Synthesis and Comparative Analysis of Carbon Dots: A Study on Continuous Flow, Microwave, and Furnace Methods

Madeleine Waskaas

Department of Chemistry
University of Bergen

A thesis submitted for the degree of

Master of Science

June 2024

Synthesis and Comparative Analysis of Carbon Dots: A Study on Continuous Flow, Microwave, and Furnace Methods

Madeleine Waskaas

Department of Chemistry
University of Bergen

Supervisor

Associate Professor Tore Skodvin
Department of Chemistry, University of Bergen

A thesis submitted for the degree of

Master of Science

June 2024

Acknowledgements

I would like to express my sincere gratitude to the following individuals for their support and contribution to the completion of this master thesis:

Assoc. Prof. Tore Skodvin, my supervisor, for his guidance, help and encouragement throughout the process.

I would like to thank **Sen. Eng. Egil Nodland** for teaching me how to use the FT-IR instrument and for providing valuable insight and guidance on the FT-IR analyses. **Hd. Eng. Frida Johanne Rakneberg Lundevall** for instructing me on the freeze-dryer, and **Postdoc Adam Leo Truskewycz** for assisting with the fluorescence analyses and teaching me how to use the fluorescence spectrometer.

The Electron Microscopic Laboratory at the University of Bergen for the TEM imaging, and especially **Eng. Irene Heggstad** for handling the microscopic imaging.

I would also like to thank **Prof. Bengt Erik Haug, Assoc. Prof. Mali Husby Rosnes,** and **Assoc. Prof. Wei Wang** for providing the equipment needed for my experiments, ensuring that the project stayed on schedule.

I am thankful to my colleagues and peers for their insightful discussions, feedback, and encouragement, which have enriched my thesis and contributed to its improvement. Special thanks to **MSc. Haakon Holien** and **MSc. Sara Storsveen Trana** for their support and comfort in the lab and throughout the entire journey, especially during the final months.

I extend my gratitude to my friends and family for their encouragement, support, and understanding during the ups and downs of this academic process. Their support has been a source of joy and inspiration. I would like to thank my uncle, **Prof. Hans Kristian Eriksen**, for his guidance and constructive feedback, which significantly improved the quality of my thesis.

I would also like to express my deepest gratitude to my boyfriend **Marius Flæsland Hoel**, whose unwavering support, encouragement, and understanding throughout this journey have been invaluable. His patience, love, and belief in me have provided the strength and motivation to overcome challenges and pursue my academic goals. I am truly fortunate to have him by my side, and his presence has enriched every aspect of my life.

Abstract

Since the discovery in 2004, Carbon Dots (CDs) have gained significant attention due to their unique properties, making them suitable for a wide range of applications. This study investigates the synthesis and properties of CDs using three different methods: continuous flow (CF), a microwave synthesizer, and a furnace. Additionally, it assesses the potential advantages of the CF technique compared to conventional batch methods.

The CD synthesis involves simple precursors and environmentally friendly solvents, aiming to optimize reaction parameters like temperature, flow rate, and reactant concentration to enhance quality and yield. Detailed characterization of the CDs includes Fluorescence spectroscopy, UV-vis spectroscopy, FT-IR spectroscopy, TEM imaging, Raman spectroscopy, and Dynamic Light Scattering (DLS). Ideally, CF setups offer precise control over reaction conditions, scalability, and efficient mixing.

The results suggest minor differences among CDs synthesized using the different methods, accompanied by common challenges such as incomplete carbonization, particle aggregation, and purification difficulties. There is a need for standardization of purification and work-up techniques, requiring further optimization, including the use of dialysis as chosen in this study. Although CF synthesis shows promise for automation and scalability, it faces obstacles concerning gas evolution and pressure control.

Certain trends were evident. For instance, nitrogen content enhanced the fluorescence of particle solutions. Prolonged residence times in cascade experiments correlated with decreased FL intensity, indicating more defined carbon cores. UV-vis spectra exhibited distinct absorption peaks at 332 nm, while FT-IR analyses depicted broad peaks indicative of complex molecular environments. Both Raman and DLS measurements faced challenges due to interference from sample fluorescence. TEM imaging confirmed the heterogeneous nature of CD samples, with larger particle sizes than previously reported.

Sammendrag

Karbonprikker (eng.: Carbon Dots) ble først oppdaget i 2004, og siden da har de tiltrukket seg betydelig oppmerksomhet på grunn av deres unike egenskaper, som gjør dem egnet for et bredt spekter av bruksområder. I denne studien vil syntesen og egenskapene til karbonprikkene bli undersøkt ved bruk av tre ulike metoder: kontinuerlig flyt (eng.: Continuous Flow), mikrobølgereaktor og ovn. I tillegg vil det bli vurdert om det er noen betydelige fordeler ved å bruke kontinuerlig flyt fremfor andre, mer tradisjonelle bulkmetoder.

I syntesen av karbonprikkene benyttes enkle reaktanter og miljøvennlige løsemidler. Reaksjonsparametere som temperatur, flythastighet (eng.: flow rate) og reaktantkonsentrasjon optimaliseres for å forbedre produktkvaliteten og utbyttet. Detaljert karakterisering av karbonprikkene omfatter fluorescensspektroskopi, UV-vis-spektroskopi, FT-IR-spektroskopi, TEM-avbildning, Raman-spektroskopi og dynamisk lysspredning (DLS). Ideelt sett vil kontinuerlig flyt gi presis kontroll over reaksjonsbetingelser, mulighet for oppskalering og effektiv blanding av reaktanter.

Resultatene antyder at det er små forskjeller og liten variasjon blant karbonprikkproduktet syntetisert fra de ulike metodene. I tillegg forekom utfordringer som ufullstendig karbonisering, aggresjon av partiklene og opprensing. Foreløpig er det et sterkt behov for en standardisering av opprensing og opparbeidingsteknikker av karbonprikker, og ytterligere optimalisering er nødvendig. Dette inkluderer dialyseteknikken som ble benyttet i denne studien. Synteser i kontinuerlig flyt har lovende muligheter for automatisering og oppskalering, men hindringer som gassproduksjon i reaktoren og trykkproblemer skaper utfordringer.

Det var enkelte trender som utpekte seg, som for eksempel at økt nitrogeninnhold ga mer intens fluorosens på partikkeløsningene. Økt oppholdstid i reaktoren under kjedereaksjonseksperimentene hadde negativ korrelasjon med fluorosens intensitet, noe som indikerer mer definerte karbonkjerner. UV-vis spektre viste distinkte absorpsjonstopper ved 332 nm, mens FT-IR-analysene viste brede topper som indikerer komplekse molekylære miljøer i prøvene. Under både Raman- og DLS-målingene var det utfordringer knyttet til interferens fra prøvefluorosens. TEM-avbildningene bekreftet at det kjemiske miljøet var svært heterogent, og partikkelstørrelsen var større enn hva som er tidligere dokumentert.

Abbreviations

ATR	Attenuated Total Reflectance
BPR	Back Pressure Regulator
CA	Citric Acid
CDs	Carbon Dots
CF	Continuous Flow
CQDs	Carbon Quantum Dots
CNDs	Carbon Nanodots
CPDs	Carbonized Polymer Dots
DLS	Dynamic Light Scattering
FL	Fluorescence
FT-IR	Fourier-Transform Infrared
GQDs	Graphene Quantum Dots
HOMO	Highest Occupied Molecular Orbital
LUMO	Lowest Unoccupied Molecular Orbital
MW	Microwave
MWCO	Molecular Weight Cut-Off
NDs	Nanodots
NPs	Nanoparticles
PDI	Polydispersity Index
PL	Photoluminescence
QCE	Quantum Confinement Effects
RTD	Residence Time Distribution
SQDs	Semiconductor Quantum Dots
TEM	Transmission Electron Microscopy
UV-Vis	Ultraviolet-Visible

Table of Contents

Acknowledgements ..... **I**
Abstract ..... **II**
Sammendrag ..... **III**
Abbreviations ..... **IV**
Table of Contents ..... **V**
1 Introduction **1**
1.1 The Origin of Carbon Dots 1
1.2 The Classification of Carbon Dots 1
1.3 The Fluorescence Mechanism of Carbon Dots 3
1.4 Synthesis Methods of Carbon Dots 5
1.4.1 Top-Down Synthesis Methods 6
1.4.2 Bottom-Up Synthesis Methods 7
1.5 Various Surface Effects: Passivation and Element Doping 11
1.6 Applications of Carbon Dots 12
1.6.1 Optical Applications 12
1.6.2 Energy Applications 12
1.6.3 Biomedical Applications 13
1.7 Continuous Flow Chemistry and Carbon Dots 13
1.7.1 Advantages of Microreactors 13
1.7.2 Comparison with Batch Processes 14
1.7.3 Carbon Dots Synthesis in Continuous Flow 15
1.7.4 Gas-Liquid Segmented Flow in Nanoparticle Synthesis 17
1.7.5 Green Chemistry and Continuous Flow 18
1.8 Objectives 20
2 Materials and Methods **21**
2.1 Chemicals and Apparatus 21
2.2 Synthesis of CDs in a Microwave 21
2.2.1 Microwave Synthesis: General Procedure 21
2.3 Synthesis of CDs Using a Furnace 22
2.3.1 Furnace Technique: General Procedure 22
2.4 Synthesis of CDs using a Continuous Flow Setup 22
2.4.1 Continuous Flow Setup: Vapourtec RS-400 System 23
2.4.2 Continuous Flow Synthesis: General Procedure 24
2.4.3 Preliminary Experiments 25
2.4.4 Cascade Experiments 27

2.5 Purification of Carbon Dots: Dialysis 27
2.5.1 Dialysis Procedure 28
2.6 Characterization Techniques 29
2.6.1 Fluorescence Spectroscopy 29
2.6.2 Ultraviolet-Visible Spectroscopy 29
2.6.3 Raman Spectroscopy 31
2.6.4 Fourier-Transform Infrared Spectroscopy 33
2.6.5 Transmission Electron Microscopy 34
2.6.6 Dynamic Light Scattering 35
3 Results 37
3.1 Synthesis of CDs in a Microwave 37
3.1.1 FL Spectroscopy 38
3.1.2 UV-Vis Spectroscopy 40
3.1.3 FT-IR Spectroscopy 40
3.2 Synthesis of CDs Using a Furnace 41
3.2.1 FL Spectroscopy 42
3.2.2 UV-Vis Spectroscopy 44
3.2.3 FT-IR Spectroscopy 45
3.3 Continuous Flow 46
3.3.1 Preliminary Experiments 46
3.3.2 Synthesis of CDs Using a Continuous Flow Setup 49
3.3.3 FL Spectroscopy 52
3.3.4 UV-Vis Spectroscopy 54
3.3.5 FT-IR Spectroscopy 55
3.3.6 TEM Imaging 56
3.4 Characterizing through Raman Spectroscopy 57
3.5 Characterizing through DLS 58
3.5.1 Evaluation the Accuracy of DLS Measurements 60
4 Discussion 61
4.1 Exploring Batch Methods: Transitioning from Microwave to Furnace Synthesis 61
4.2 Exploring Continuous Flow for CD synthesis 62
4.3 FL Spectroscopy: Characterization and Analysis of CD Samples 65
4.3.1 Excitation-Dependent Emission Characteristics of CDs Synthesized by Different Methods 65
4.3.2 Emission Spectra and Fluorescence Intensity of CD Samples 66
4.4 UV-Vis Spectroscopy: Characterization and Analysis of CD Samples 67
4.4.1 Detailed UV-Vis Spectra Analysis of CD Samples from Different Synthesis Methods 67

4.4.2 Guidelines for Interpreting UV-Vis Spectra of CD Samples 68
4.5 Interpretation of FT-IR Spectra: Broad Peaks and Molecular Environment 69
4.5.1 Comparative Analysis of CD IR Spectra from Each Synthesis Method 69
4.5.2 Comparative Analysis of CD IR Spectrum and Second Derivative 71
4.6 Challenges and Limitations of Raman Spectroscopy 72
4.7 Particle Size Analysis through DLS 73
4.8 TEM Analysis and Characterization of CDs 74
4.9 Overall Insights: Challenges and Observations in CD Synthesis and Characterization 75
5 Conclusion 77
5.1 Conclusive Analysis of CD Synthesis Methods: Microwave, Furnace, and Continuous Flow Techniques 77
6 Further Work 78
6.1 Investigation of Advanced Reactor Designs and Control Strategies 78
6.2 Enhancement of Surface Passivation of CDs 78
6.3 Evaluation of Alternative Purification Techniques of CDs 78
7 References 79
8 Appendices 86
A 12 Principles of Green Chemistry 86
B Biotage Initator: Report 87
C FL Instrument Settings 87
D FL Emission Spectra for All CD Samples 88
E Vapourtec System: Pressure Fluctuations 93
F DLS Expert Advice 93
G DLS: Correlation Graphs 94
H DLS: Size Measurement Graphs 95
I FT-IR Spectra 96
J TEM Images 105

1 Introduction

1.1 The Origin of Carbon Dots

Carbon Dots (CDs) are nanoparticles typically less than 10 nm in diameter (1-4). These particles generally consist of clusters of carbon atoms along with additional elements such as oxygen, hydrogen, and nitrogen (2, 5). Carbon nanoparticles were first discovered in 2004 when Xu and coworkers synthesized single-walled carbon nanotubes via preparative electrophoresis (6). Later in 2006, Sun and coworkers reported a new finding which they named carbon dots (7). The particles were synthesized via laser ablation of a carbon source in the presence of water vapor with argon as the carrier gas. Since these discoveries, interest in CDs has increased significantly across various scientific fields (8). While carbon is typically known to be a black material with low solubility in water and weak fluorescence (3), CDs exhibit the opposite characteristics, including high water solubility and strong fluorescence. Additionally, they can be synthesized using inexpensive methods, are easily surface-modified, and often display low toxicity (1).

1.2 The Classification of Carbon Dots

The classification of CDs has been a subject of debate since their discovery. Cayuela and coworkers noted a lack of clarity in the terminology associated with these particles, with various names being used interchangeably, including semiconductor quantum dots (SQDs), carbon dots (CDs), carbon quantum dots (CQDs), graphene quantum dots (GQDs), carbon nanodots (CNDs or NDs), etc. (8-10). To establish a clearer understanding of nanoparticles (NPs), they are generally defined as particles with dimensions ranging from 1 to 100 nm (11).

The term "quantum" in this context refers to the manifestation of quantum confinement effects (QCE) within the particles, a criterion for defining as "CQDs" (9, 10). In nanoscience, "dots" typically denote nanometer-sized particles (9), prized for their unique functional and structural properties emerging at the nano scale. Generally, all CDs possess a carbon core with various functional surface groups.

A proposed framework of Cayuela et al. (9) comprises two main divisions: semiconductor-based dots and carbon-based dots. Semiconductor quantum dots (SQDs) exhibit unique optical properties such as tunable photoluminescence and are characterized by their core-shell structure with a crystalline carbon core and functionalized surface. Within the category of carbon-based dots, three subgroups are defined based on specific characteristics.

The term "carbon nanodots" (CNDs) is used for quasi-spherical nanodots that lack quantum confinement (9, 12). Conversely, carbon-based nanodots that exhibit QCE or have a crystalline structure are termed "carbon quantum dots" (CQDs). The term "quantum dots" (QDs) refers to NPs exhibiting QCE and size-dependent photoluminescence emission (9, 10), distinguishing them from other types of CNDs.

Additionally, NDs presenting a π-conjugated single sheet are referred to as "graphene quantum dots" (GQDs), with particle sizes potentially reaching up to 20 nm (9, 12, 13). GQDs typically originate from graphene-based precursors and are made up of a single or few graphene layers with functional groups at the edges (13). In contrast, CQDs generally derive from carbon nanomaterials with a crystalline structure, although they can also be synthesized via pyrolysis of organic materials at high temperatures (9).

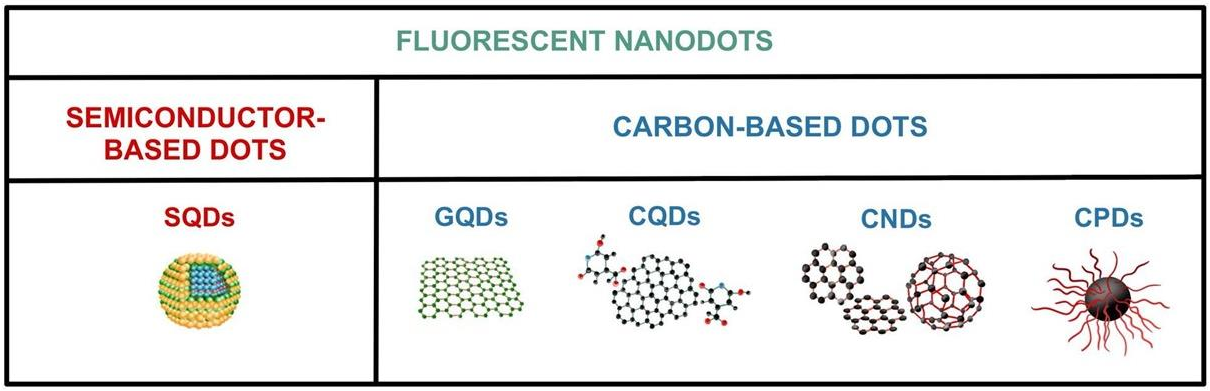

Figure 1: Classifications of fluorescent nanodots: semiconductor quantum dots (SQDs), graphene quantum dots (GQDs), carbon quantum dots (CQDs), carbon nanodots (CNDs), and carbonized polymer dots (CPDs). Recreated based on figures from Cayuela et al. and Zhao et al. (9, 12) with modifications.

In a contemporary classification proposed by Zhao et al. (12), the understanding of CDs has evolved alongside advancements regarding the synthesis and characterization techniques. Generally, CDs are carbon-based nanomaterials that exhibit fluorescence properties, combining sp^2 and sp^3 carbon atoms with various functional groups and polymers. Common classifications include GQDs, CQDs, and "carbonized polymer dots" (CPDs).

GQDs typically consist of fewer than five layers of graphite lattices, featuring an anisotropic carbon core and surface-bound functional groups (12). The anisotropic nature implies that the core structure varies along different axes, with lateral dimensions typically larger than height dimensions (13).

CQDs, on the other hand, are three-dimensional multilayer graphite structures with surface functional groups. Unlike GQDs, the lateral and height dimensions of these particles are comparable, contributing to their spherical appearance (12).

The third division encompasses CPDs, formed as polymer structures with a carbon core, featuring a hydrophobic interior and hydrophilic exterior. Both polymerization and carbonization processes are important for their formation (12), which is detailed in chapter 1.4.2 "Bottom-up Synthesis Methods".

To simplify the discussion in this paper, the general term "carbon dots" (CDs) will hereafter be used.

1.3 The Fluorescence Mechanism of Carbon Dots

In general, luminescence can be defined as light emission from a molecule, encompassing various types (14). Photoluminescence (PL) is the process where a photon is absorbed, causing excitation of an electron (15). More specifically, fluorescence (FL) is a phenomenon where light excites an electron to higher state, followed by energy loss through vibrations and the emission of a photon as the electron returns to a lower state. Molecules that absorb light at one wavelength and emit light at another are termed fluorophores, typically emitting longer wavelengths than absorbed.

Radiative decay, the process where an excited electron loses energy, manifests as fluorescence or phosphorescence, with fluorescence characterized by rapid decay and phosphorescence by longer-lasting emission (16), as illustrated Figure 2.

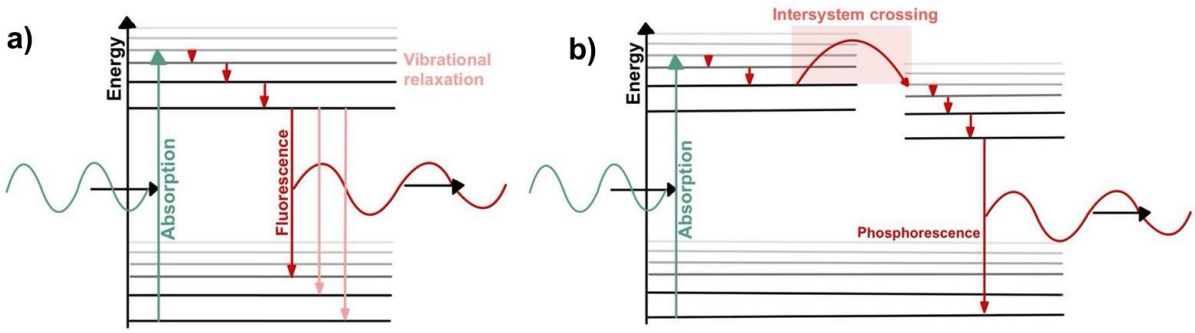

Figure 2: a) The sequence steps of fluorescence. b) The sequence steps of phosphorescence. The important step is the intersystem crossing from an excited singlet state on the left to an excited triplet state on the right. Based on figures from Atkins et al. (16) with modifications.

The physics involved in these processes are described by elementary quantum mechanics; see e.g., Atkins and de Paula (16) for a recent review. When an excited electron absorbs energy from an incident photon, it enters an excited state. As a result, it interacts with surrounding molecules, colliding, and losing energy as it steps down to lower vibrational levels. The remaining excess energy is then emitted as a photon. Phosphorescence is a type of PL like FL, but with a key difference in the electronic transitions involved. When a molecule absorbs light, it is lifted from the ground state to an excited singlet state. In phosphorescence, the molecule can undergo

intersystem crossing to an excited triplet state, where the two electrons have parallel spins, placing them in a spin-forbidden state. This spin configuration makes the transition back to the ground state slow, resulting in delayed emission. As a result, the material continues to glow even after the excitation source is removed, with emission lasting from milliseconds to hours as the electron gradually loses energy through various vibrational levels.

When it comes to the FL mechanism of CDs, this is an active area of research. Several ongoing studies aim to provide a more detailed understanding of the processes involved (17). A number of research groups have proposed possible FL mechanisms of the CDs. Three of the suggested explanations are the quantum confinement effect (QCE), surface defect states, and the presence of fluorophores (2, 18, 19), respectively.

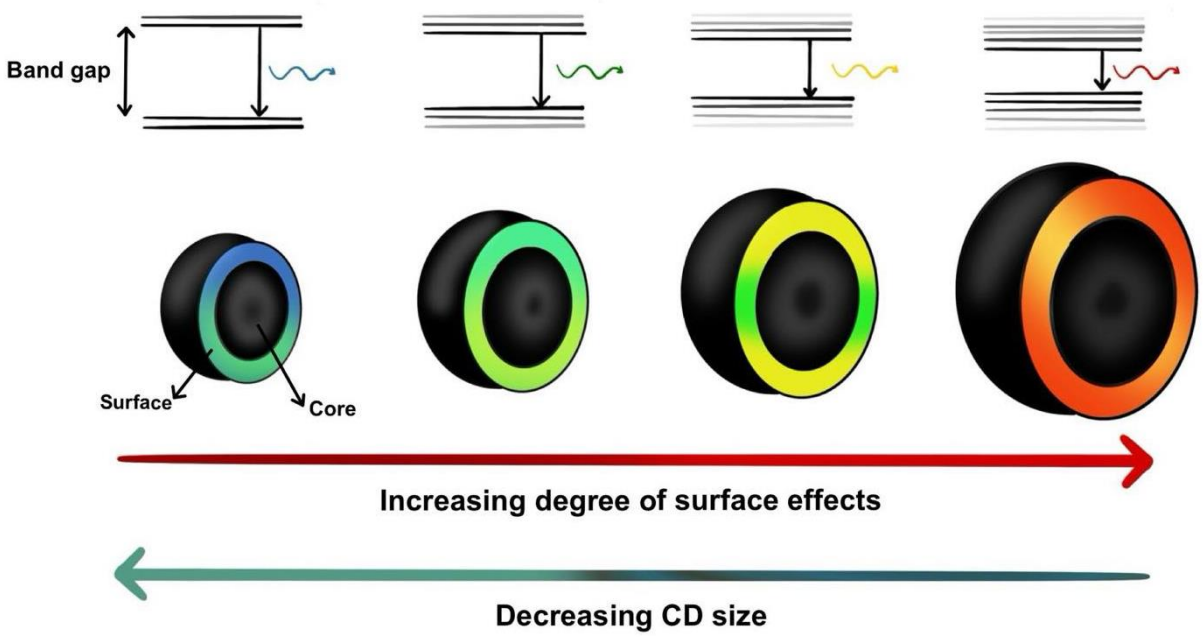

Figure 3: Changes in surface effects or higher oxidation intensity shift the emitted light towards the red end of the spectrum, meaning longer wavelengths with less energy. This red shift occurs because surface effects create new energy levels within the band gap, resulting in lower energy photon emissions. Similar observations occur with emission being size-dependent: as the size decreases, the band gap increases, causing the emission to shift towards shorter wavelengths. This figure is recreated with modifications based on figures by Ullal et al. (20).

The FL mechanism in QCE is influenced by variations in particle size. As the size of CDs decreases, their energy bandgap increases, resulting in higher energy transitions and shorter emission wavelengths (2, 17, 19). Surface defect states, caused by surface irregularities and oxidation, play a crucial role in the FL of CDs (2, 19). More defects or more oxidations tend to shift the emitted light towards the red end of the spectrum, meaning towards longer wavelengths with less energy. This red shift occurs because surface defects create new energy levels within the band gap, leading to lower energy photon emissions corresponding to longer wavelengths (2, 19, 21). Including

fluorophores via surface functional groups like C=O and C=N can introduce diverse energy levels in CDs, thereby impacting the FL (22). This can enable the development of multicolor CDs, which was done by Zhang et al. (23) where they synthesized nitrogen-doped CDs emitting various colors which were dependent on surface functional groups rather than oxidation degree. The presence of such fluorophores can also be either attached to the CD surface or float in the sample solution. As a result, their presence inevitably increases the FL intensity and can lead to misleading results (20).

1.4 Synthesis Methods of Carbon Dots

Since the discovery of CDs, numerous synthesis methods have emerged, each influencing the properties of the particles. Synthesis routes and precursor selection play crucial roles in determining CD characteristics (1-3, 24). Common methods for CD synthesis can generally be classified into two main approaches: "top-down" and "bottom-up" methods. It is important to acknowledge that while these approaches are widespread, other techniques exist, and often, a combination of methods is employed to achieve the desired CDs. On the right side of Figure 4, various common synthesis routes relevant to this discussion are listed.

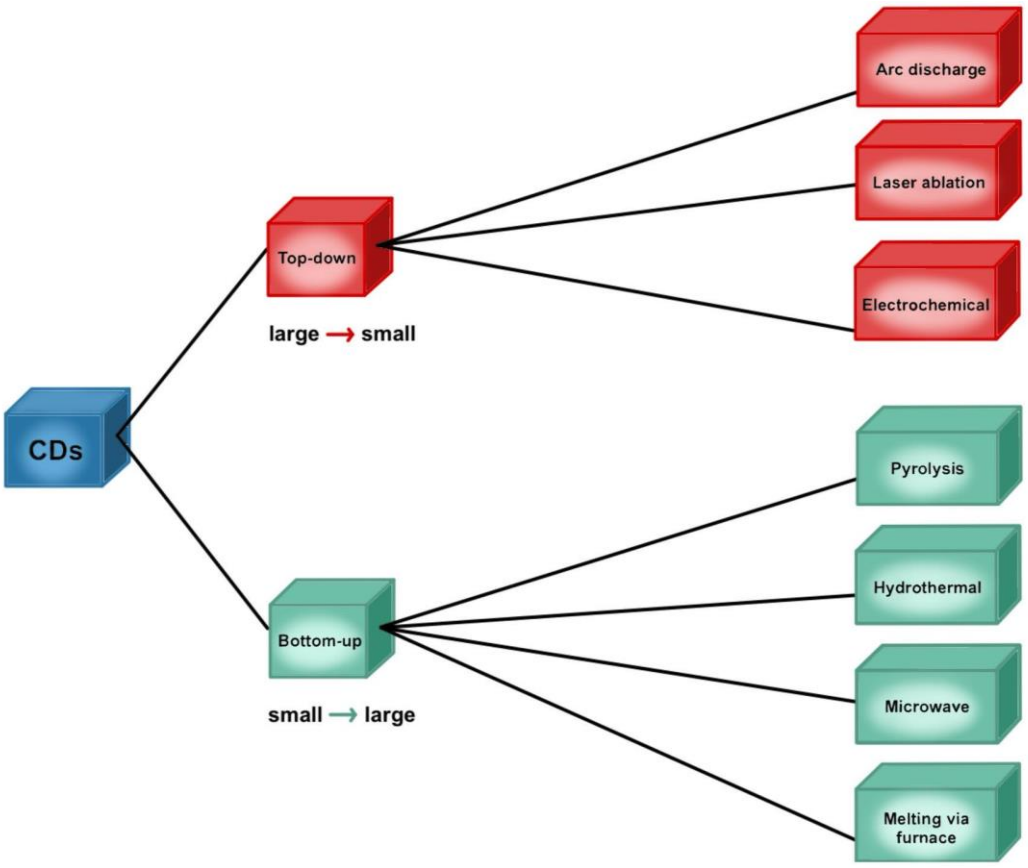

Figure 4: Graphical abstract of a selection of CD preparation methods categorized into top-down and bottom-up approaches. Top-down methods include arc discharge, laser ablation, and electrochemical processes. Bottom-up methods consist of pyrolysis, hydrothermal synthesis, microwave reactor techniques, and furnace melting.

1.4.1 Top-Down Synthesis Methods

Top-down syntheses involve breaking down larger carbon sources into CDs through chemical and physical means (1, 2, 24). Common carbon sources include carbon nanotubes, graphite, or carbon fibers. Methods such as arc discharge, laser ablation, and electrochemical synthesis are typical in this category. While these methods offer simplicity and versatility, they often require extended reaction times and harsh conditions (1).

For instance, the arc discharge method begins with the preparation of single-wall carbon nanotubes, followed by the appearance of CDs post-separation and purification (24, 25). However, CDs produced via this method tend to exhibit high oxygen content, low FL, and complex compositions (24).

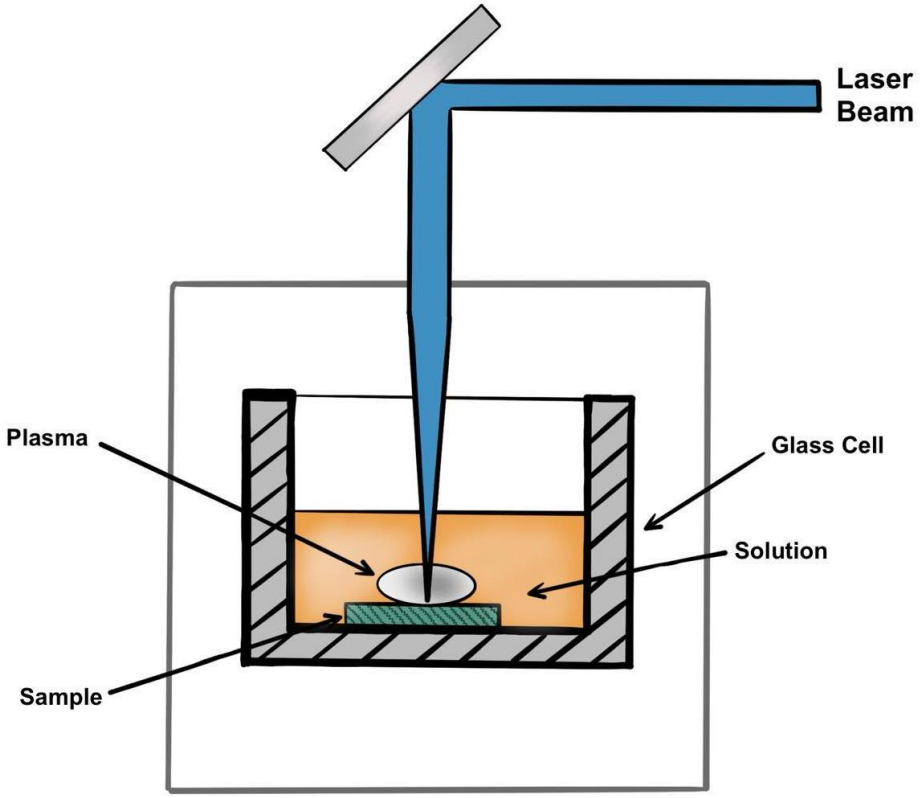

Figure 5: Process of laser ablation. Laser ablation removes material from a solid or liquid surface by directing a laser beam at the target. The material heats up, converts to plasma, and then condenses into nanoparticles. Adapted from figures on the "Laser Ablation" Wikipedia page (26), with modifications.

In the laser ablation method, carbon sources are targeted with a high-intensity laser. The laser beam is directed at a carbon-containing material, such as graphite or carbon nanotubes, in a high-temperature and high-pressure environment (2, 8, 24, 25). This causes the material to vaporize and form plasma, which then condenses into NPs. The carbon source can be immersed in either a liquid or vapor medium, and by adjusting the physical conditions of the laser or the target materials,

CDs with varying properties can be produced (2, 25). This method is valued for its simplicity and ability to create various nanostructures, although it often results in wide size distributions and challenges in reproducibility (8). The process is illustrated in Figure 5.

The electrochemical method involves repeated charging and discharging of carbon sources, commonly utilizing graphene or graphite electrodes (24). While this method utilizes readily available materials and yields high-purity products, the source pretreatment and purification processes can be intricate and time-consuming (2, 24).

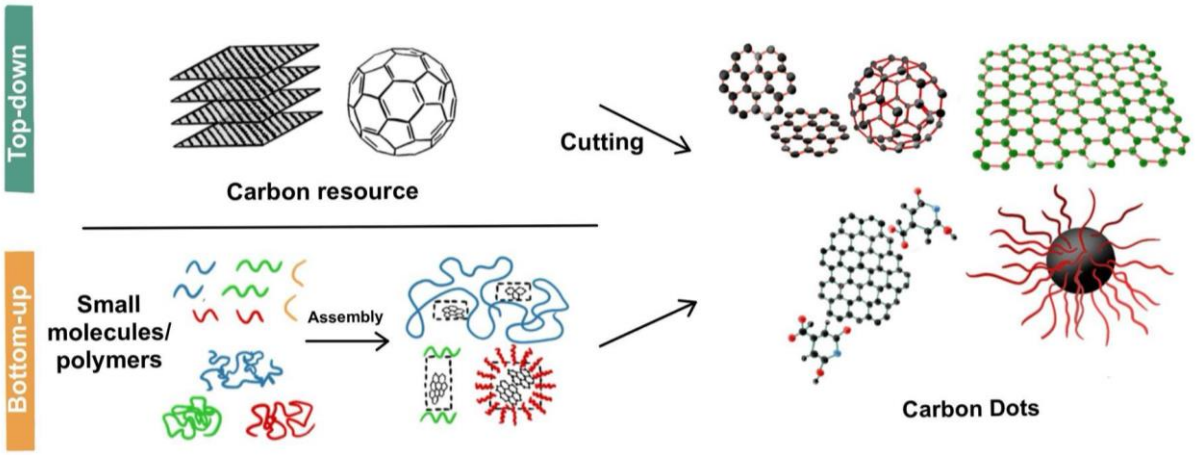

Figure 6: Illustration depicting the two synthetic routes: top-down and bottom-up. In top-down, larger carbon resources are broken down into CDs, and in bottom-up, small molecules and polymers are assembled to form CDs. Recreated based on figures from Zhu et al. (13) with modifications.

1.4.2 Bottom-Up Synthesis Methods

In contrast to top-down methods, which involve breaking down larger materials into smaller units, bottom-up synthesis builds particles from smaller molecules. This approach allows for precise control over the composition and properties of the resulting CDs. Bottom-up approaches utilize small organic molecules or oligomers as precursors for CD synthesis (24). Precursors such as citric acid, glucose, and urea are commonly employed, with methods including chemical oxidation, thermolysis, hydrothermal, and microwave synthesis (2, 19, 24, 25). Microreactors and continuous flow setups have also been employed to synthesize CDs (27-30).

The bottom-up process typically involves four stages: decomposition of precursors, polymerization, carbonization, and surface passivation (19), as illustrated in Figure 7. (Further elaboration on surface passivation will be provided later chapter 1.5 “Various Surface Effects”, p.11). Liu et al. proposed a mechanism for CD formation involving condensation reactions forming intermediate compounds, which then polymerize to form polymer-like CDs (19). Subsequently, these polymers undergo carbonization at elevated temperatures to form a carbon core. Finally, remaining precursor molecules act as surface passivating agents, enhancing the FL and stability of

the CDs. The thermal degradation and carbonization processes are complex and challenging to control precisely.

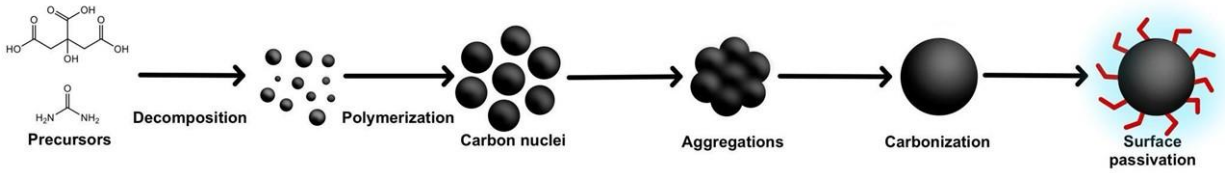

Figure 7: A schematic illustration depicting the possible mechanism for the formation of CDs: starting with decomposition and condensation reactions of the precursors, followed by polymerization into carbon nuclei, aggregation, and carbonization. The final step, surface passivation, shows the doping of other components on the surface to enhance fluorescence. This figure is recreated with modifications from Liu et al. (19).

In a study by He et al. (31) the influence of temperature was systematically examined on CD formation using a microwave approach. It was found that increasing the temperature from 160°C to 200°C caused the precursor molecules to form more defined carbon cores, but it reduced the FL intensity due to the consumption of fluorescent groups. Extending the heating time further decreased PL as more FL groups were carbonized to carbon cores. This study underscored the importance of carefully controlling both temperature and reaction time to achieve the desired CD properties.

Pyrolysis involves the thermal decomposition of organic materials at high temperatures in an inert atmosphere (1). This method results in physical and chemical changes in the material, forming CDs (1, 24). Various organic precursors can be used, and by controlling the degree of decomposition, the properties of the CDs can be managed. This method is simple and often yields CDs with strong FL.

Hydrothermal synthesis employs both high temperature and high pressure to produce CDs (3, 24). This method is one of the most widely used due to its ability to produce larger quantities of CDs with strong FL (2). Typically, small organic precursors are dissolved in water and the reaction mixture is heated in a Teflon-lined stainless-steel autoclave, as illustrated in Figure 8. The high temperature and pressure facilitate the formation of carbon cores, which serve as nucleation points for further growth into CDs.

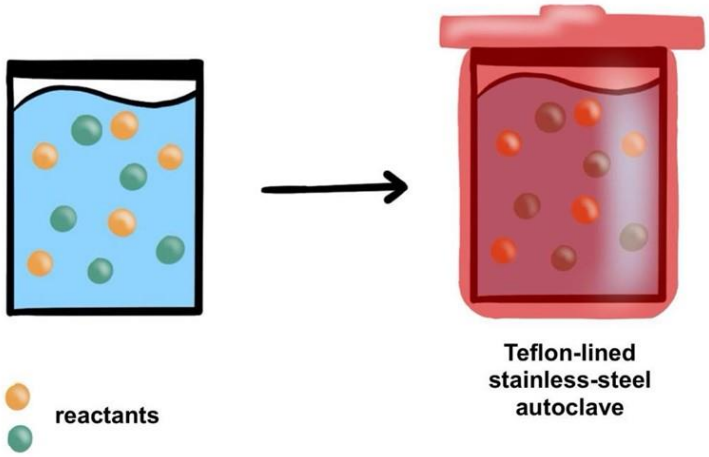

Figure 8: Illustration of a hydrothermal setup. The reactants are dissolved in water and heated to high temperatures and kept at high pressure in a Teflon-lined stainless-steel autoclave. These conditions facilitate the formation of nanoparticles.

Introduced in 1986, microwave (MW) chemistry has emerged as a leading synthesis technique, extending its application to nanomaterial and organic synthesis, including CDs (32-34). This method not only reduces reaction times but also enhances yields and product purities by minimizing side-products (1, 2, 24, 35). The rapid heating characteristic of MW synthesis accelerates nucleation, yielding monodispersed nanostructures (36). Additionally, polar solvents, such as water, interact favorably under MW conditions, facilitating efficient absorption and heat conversion (37).

In contrast to conventional heating methods relying on conduction and convection, MW heating operates through two primary mechanisms: dipolar and ion polarizations (38). When exposed to microwave irradiation, polar molecules in the reaction mixture align with the alternating electric field, as demonstrated in Figure 9. MW synthesis leverages these mechanisms, aligning polar molecules with the dipolar field and inducing heating through charge carrier mobilization.

Moreover, MW reactors, like continuous flow setups, can maintain high temperatures and pressures, significantly accelerating reactions. The efficiency of MW synthesis lies in its utilization of the dielectric properties of materials and the interactions with MW radiation, providing a swift and controlled approach to synthesis.

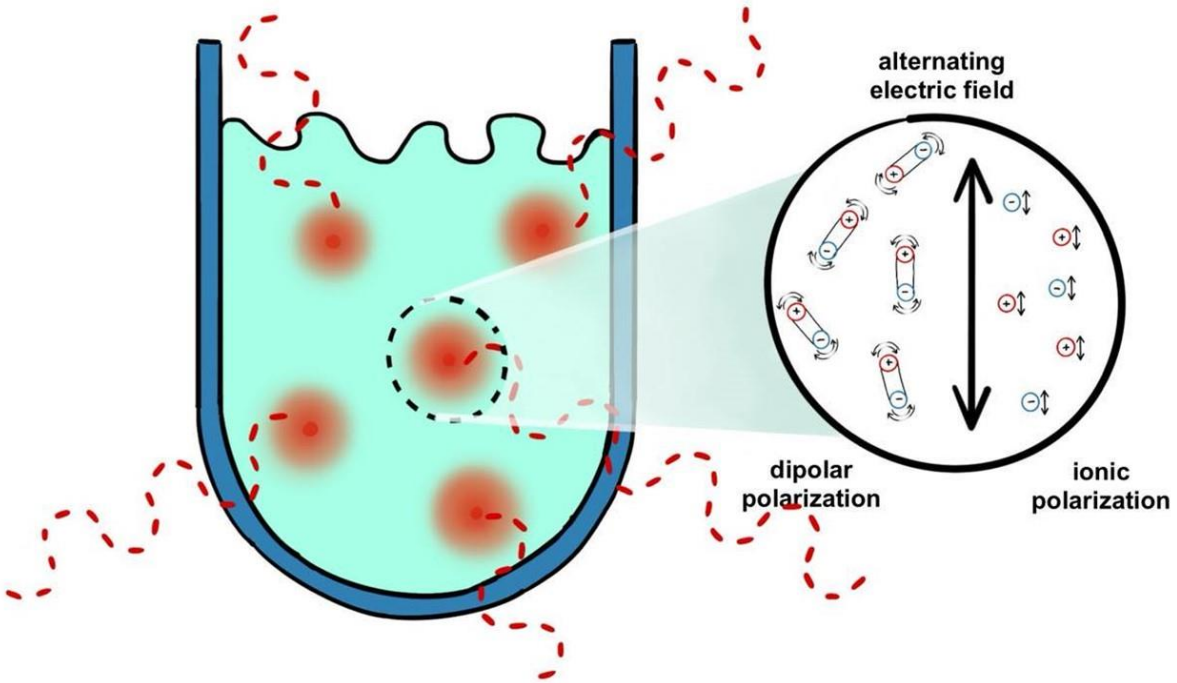

Figure 9: Illustration of a microwave reactor. In microwave-assisted chemical reactions, reactants are placed in a microwave-transparent vessel and exposed to microwave radiation. The microwaves rapidly heat the reactants, increasing the reaction rate and often leading to higher yields and selectivity. This process involves two primary mechanisms: dipolar and ionic polarization. When exposed to microwave irradiation, polar molecules within the reaction mixture align with the alternating electric field, causing dipolar polarization. Additionally, charge carriers mobilize, contributing to ionic polarization. These mechanisms enhance the efficiency and effectiveness of the reaction. This figure is based on figures from Mohamad Aziz et al. (38) and Rabiller-Baudry et al. (39).

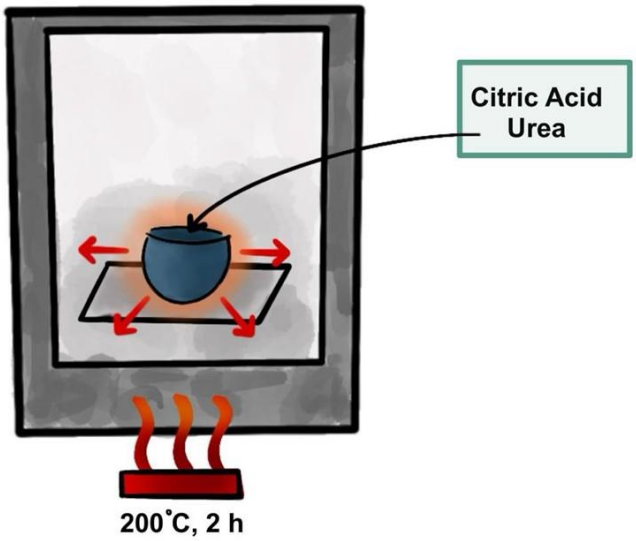

Figure 10: CD Synthesis in a furnace. In this paper, the precursors (CA and urea) are combined and heated in a crucible at 200°C for 2 hours. This method, a type of bottom-up synthesis technique, offers a straightforward, cost-effective, and eco-friendly route to synthesize CDs through simple heating.

Recently, Chen and colleagues (40) successfully synthesized nitrogen-doped CDs through a one-step sintering technique. Ammonium citrate and citric acid were used as precursors. The precursors

were separately heated in a crucible in an oven 180 ˚C for 4 hours. Sintering is a process that involves compacting and forming a solid mass of material by applying heat or pressure without melting it to the point of liquefaction (41). The method is described as straightforward, cost-effective, and environmentally friendly (40).

1.5 Various Surface Effects: Passivation and Element Doping

CDs primarily consist of carbon, hydrogen, and oxygen, and the composition depends on the carbon source and preparation method (30, 42). Usually, CDs composed of these elements emit weak blue FL (18, 42). However, to broaden the utility of CDs and render them more appealing for diverse applications, enhancing the FL properties becomes imperative. Surface modifications are frequently employed to achieve this enhancement (8). By modifying the surface chemistry or structure of CDs through techniques like passivation or doping, the optical characteristics, including FL, can be influenced. These alterations have the potential to induce shifts in emission wavelength, enhance intensity, and improve the stability of FL emission.

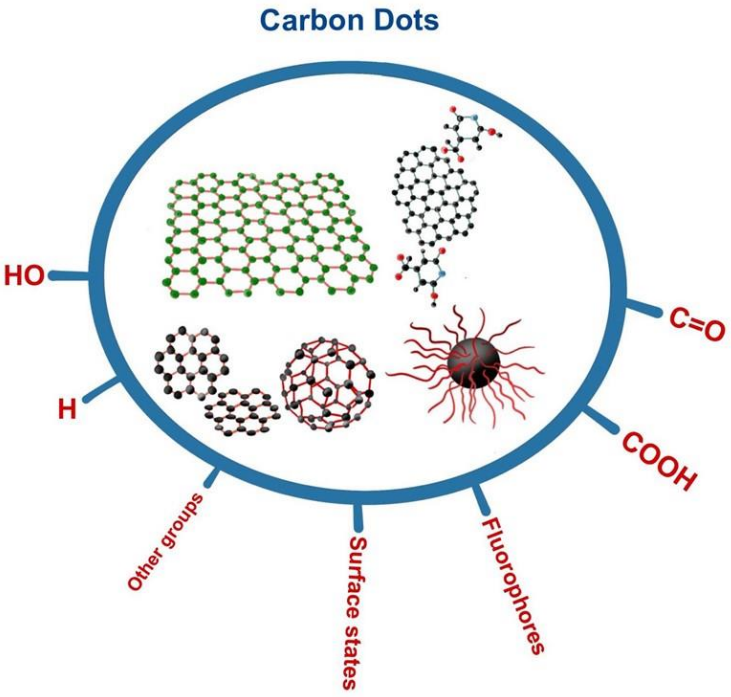

Figure 11: Instances of different surface states situated on the surface of CDs, as per Zhu et al. (13) with alterations. Depicts diverse types of FL CDs: GQDs, CQDs, CNDs, and CPDs.

Numerous techniques and synthetic routes lead to CDs, resulting in a wide range of chemical structures. Despite this diversity, the FL and absorption characteristics of CDs remain consistent (13). Liu et al. (19) proposed an explanation of the bottom-up approach, emphasizing the final step of surface passivation. This step functions to enhance the PL properties and alter FL emissions (13, 24). It involves using remaining precursor molecules as surface passivating agents, which attach

to the CD surface. Different functional groups have different energy levels, creating various possible energy levels for the CDs to undergo FL. Thus, by synthesizing CDs with different surface groups, it is possible to manipulate the FL emission.

Another effective technique is doping CDs with other elements such as nitrogen (N) and sulfur (S) (18, 24, 42). Introducing new elements into the CD structure, both in the carbon core and on the surface, can create new energy levels or alter the original band gaps, thereby changing the PL emissions and potentially enhancing the FL properties.

N-doping is particularly effective due to the close similarity between nitrogen and carbon. This method is the most widely used to enhance the PL properties of CDs (18, 43). Nitrogen atoms increase electron density in the CDs, altering the electronic environment and significantly improving the FL properties. N-doped CDs have shown excellent performance in biomedical applications such as bioimaging and biosensing (18, 24).

1.6 Applications of Carbon Dots

CDs are versatile materials with applications in optical, energy, and biomedical fields due to the low toxicity, strong PL, good photostability, and water solubility.

1.6.1 Optical Applications

CDs are ideal for optical applications due to the FL properties, high sensitivity, low cost, and easy preparation methods (44). They are used as fluorescent probes for detecting various environmental analytes. The properties, such as size, surface area, and surface functional groups, make them sensitive to environmental changes like temperature, pH, solvent, and ionic strength, enabling the enhancement or quenching of FL.

CDs have been used to detect cations such as Fe^{3+} (29), Cr^{6+} (45), Cd^{2+} (46), and Hg^{2+} (47). Additionally, they serve as pH sensors, with synthesized N-doped CDs showing responsiveness to acidic environments, demonstrating potential in environmental monitoring and pollution detection (40).

1.6.2 Energy Applications

CDs have shown to be effective photocatalysts for degrading pollutants, reducing CO_2, and facilitating various chemical reactions by harnessing solar energy (25, 44). The broad light absorption range, low cost, good photostability, and efficient charge separation and transfer make them ideal for these applications. They are also used as electrocatalysts, with the abilities enhanced by heteroatom doping (48).

1.6.3 Biomedical Applications

CDs are promising in biomedicine due to their low toxicity, biocompatibility, rapid excretion, small size, high photostability, and unique optical properties. The biomedical applications include bioimaging, drug and gene delivery, and nanomedicine (1, 24, 25, 44). The low toxicity and biocompatibility of the CDs, make them suitable for targeting and imaging cancer cells (49) and detecting bacteria (50).

1.7 Continuous Flow Chemistry and Carbon Dots

Since the 1990s, chemical research has increasingly explored the use of microreactors for syntheses (51). Continuous flow (CF) chemistry often involves the use of narrow capillary tubes to take advantage of the controlled properties inherent in this setup (52). Microreactors, characterized by cross-sections less than 1 mm in diameter, present unique opportunities not accessible with traditional batch reactors (51, 53-56). It is worth noting that while CF is typically associated with microscale setups, it also finds application in larger-scale operations.

This paper compares continuous flow and batch reactions, with a focus on NP synthesis and CD synthesis. The emphasis is on NP synthesis due to its relevance and the distinct advantages CF setups offers for this application.

1.7.1 Advantages of Microreactors

Microreactors provide several advantages that enhance the efficiency and effectiveness of chemical reactions, advantages which batch reactors often lack. Firstly, the high surface-area-to-volume ratio improves mixing and results in enhanced thermal and mass transfer properties. This is coupled with short diffusion distances, leading to improved reaction kinetics and higher reproducibility (52-57).

Moreover, microreactors offer efficient heat transfer, which is particularly beneficial for exothermic reactions. This property ensures nearly isothermal conditions, preventing temperature spikes that could lead to undesired side reactions (54, 56, 58, 59). Enhanced control over pressure and temperature in microreactors facilitates reactions at higher concentrations and with less solvent usage, reducing process costs and environmental impact.

Additionally, microreactors ensure optimal mixing and stoichiometry, providing consistent reaction conditions that improve yields and selectivity (52, 58). This precise control helps prevent undesirable side reactions and ensures that the reaction conditions remain stable throughout the process.

Novel process windows aim to improve existing processes by utilizing elevated pressures and temperatures, increased concentrations, or process integration (54, 56, 58). Microstructured systems enhance heat transfer and temperature control, enabling reactions to occur safely above the normal boiling point of the solvent. The former is achieved partly through the use of a back pressure regulator (BPR), which maintains a steady pressure throughout the reaction, particularly at elevated temperatures.

1.7.2 Comparison with Batch Processes

Batch processes involve producing materials in discrete quantities, where all reactions occur within a single vessel at once, making them suitable for smaller-scale productions with versatile reaction conditions, including high temperatures, pressures, and reactant concentrations (52, 54, 57, 60). Reactants are loaded into a vessel, allowing the reaction to proceed before emptying and cleaning the reactor. While well-suited for many applications, batch processes have limitations, especially for fast and exothermic reactions due to low surface-to-volume ratios and mixing challenges (54). Scaling up batch processes can further magnify these issues, requiring additional heat exchangers and mixing devices (54, 59). On the other hand, CF systems operate with a steady stream of reactants and products, offering precise control over reaction parameters and enabling seamless scalability for large-scale processes (54, 57). CF systems offer increased efficiency, enhanced safety, and reduced waste generation by maintaining continuous operation and providing tighter control over reaction conditions.

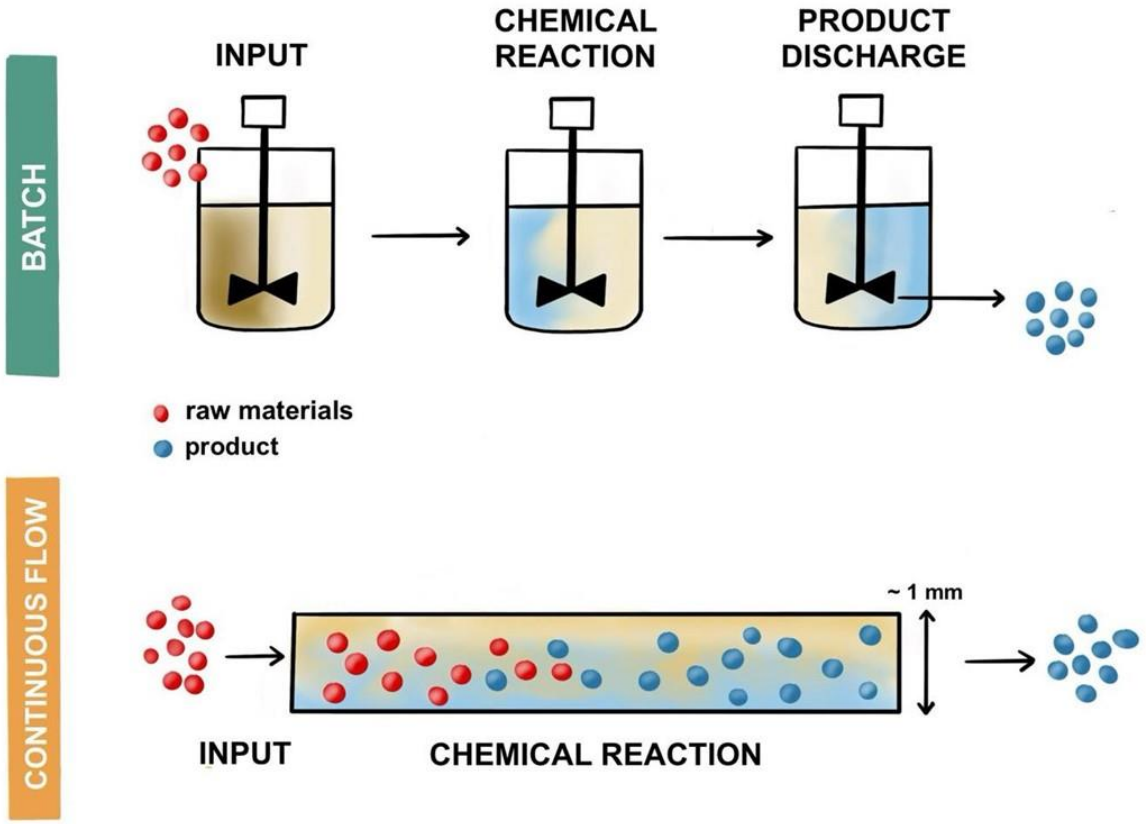

Figure 12: Batch and continuous flow processes. In a batch process, reactants are added to a container where the chemical reaction occurs, and the product is subsequently discharged. In contrast, a continuous flow process involves a steady stream where raw materials are converted to products as they pass through the reactor. A typical flow capillary has a diameter of about 1 mm. The figure is recreated based on figures from Nambiar et al. (61) with alterations.

In batch processes, the product forms as NPs through a precipitation process involving nucleation, growth, and agglomeration, all happening in the same volume (62). Microreactors, operating at the micrometer length scale, offer better control over each of these process steps independently. Longer residence times typically lead to a broader size distribution as particles are exposed to reaction conditions for an extended period, promoting growth and agglomeration. Conversely, shorter residence times narrow the size distribution by limiting the time available for particle growth or aggregation, resulting in more uniform NPs.

1.7.3 Carbon Dots Synthesis in Continuous Flow

Microreactors are particularly attractive for NP synthesis because they offer improved control over particle size, composition, and size distribution (30, 51, 62, 63). Continuous flow systems effectively address the challenges associated with batch synthesis, such as irreproducibility and inconsistent particle quality. With integrated heaters and fluid control, reactions can be conducted under more aggressive conditions, potentially resulting in higher yields (62, 63). It is important to highlight that

while many acknowledge the great potential of CF syntheses, there is overall a noticeable lack of publications specifically addressing this technique.

Various methods have been developed to synthesize CDs using different precursors, as detailed in Chapter 1.4, "Synthesis Methods of Carbon Dots". However, CF methods have shown promise for CD synthesis, offering scalability and control over size and properties (27-30). CF techniques allow for precise control of critical reaction parameters such as temperature, mass transfer, flow rates, and pressure, which are challenging to achieve in traditional batch methods.

In 2023, Campalani and colleagues published a comprehensive review on the importance of CF methods for CD synthesis (30). They emphasized that the ability to control these parameters enables the synthesis of CDs with consistent optical, chemical, and electronic properties. Despite this potential, achieving consistent results remains challenging. The review highlighted the difficulty in drawing general conclusions about the effects of CF parameters on CD structure and properties due to the diverse conditions reported in the literature. These conditions include variations in temperature, reactor type, residence time, and carbon precursor concentration and type. However, certain trends are evident, such as the goal of synthesizing CDs with the smallest possible size, narrow size distribution and strong FL.

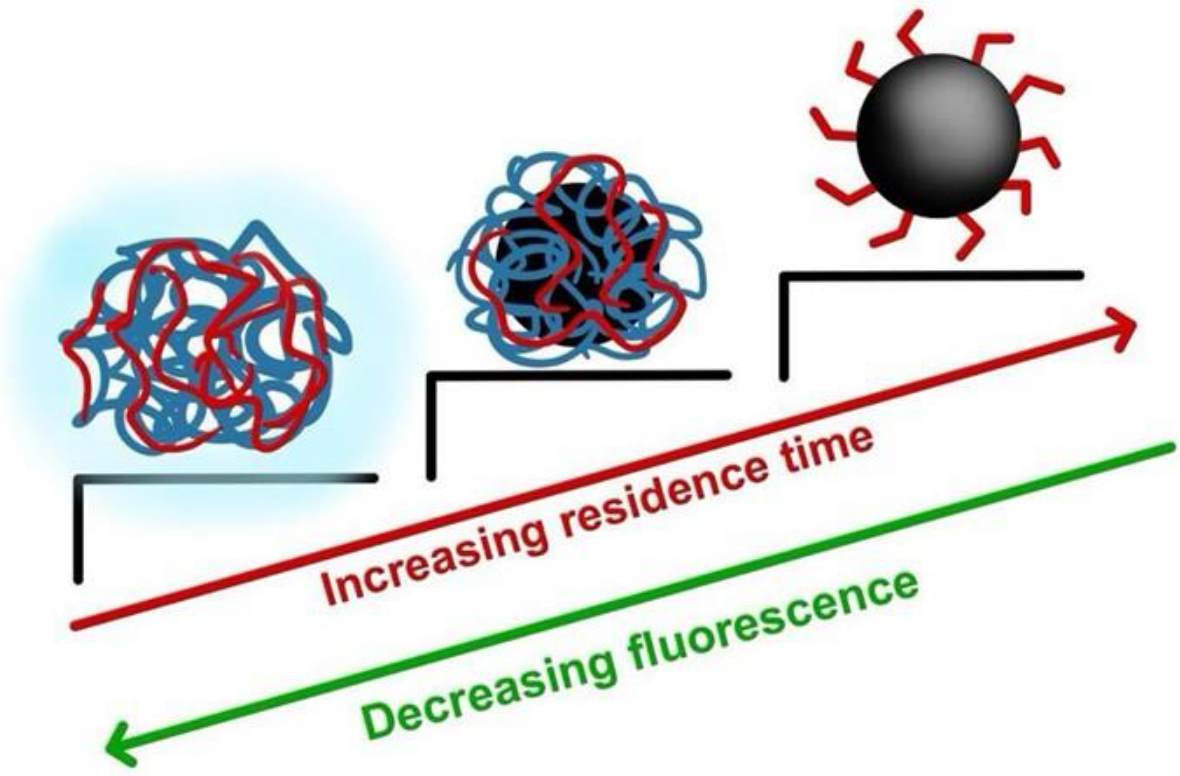

Figure 13: Illustration of the formation process of CDs where increased residence time leads to decreased FL properties due to extended participation in the carbonization process. Adapted with modifications from Liu et al. (19).

Lu et al. (51) were pioneers in screening reaction conditions for CDs, focusing on PL properties. They optimized various precursors, solvents, additives, and reaction conditions, including temperature and time. In most cases, it was noted that variations in reaction temperature, time, and precursor concentration did not have a significant impact on the PL properties of CDs. However, experiments with longer residence times and higher temperatures resulted in CDs with lower hydrogen and oxygen content and higher carbon content. This phenomenon can be attributed to prolonged participation in the carbonization process, leading to larger particles (28, 30, 51), as illustrated in Figure 13.

1.7.4 Gas-Liquid Segmented Flow in Nanoparticle Synthesis

This review of gas-liquid segmented flow is based on the review of NP synthesis in microreactors by Zhao et al. (62). If a reaction generates significant amount of gas, gas bubbles may transform a single liquid flow to a gas-liquid segmented flow. This segmented flow can greatly influence mixing, residence time distribution (RTD), and ultimately the NP size distribution.

In gas-liquid segmented flow, gas bubbles create segmented slugs within the liquid, enhancing mixing within each liquid segment and reducing axial dispersion – the spreading of reactants along the length of a flow channel or reactor. By segmenting the liquid into discrete units separated by gas bubbles, it can give more uniform reaction conditions. Ideally, gas-liquid segmented flow generally provides a narrower RTD compared to a single liquid flow, helping ensure that reactants spend more uniform amounts of time in the reactor, leading to more consistent NP sizes.

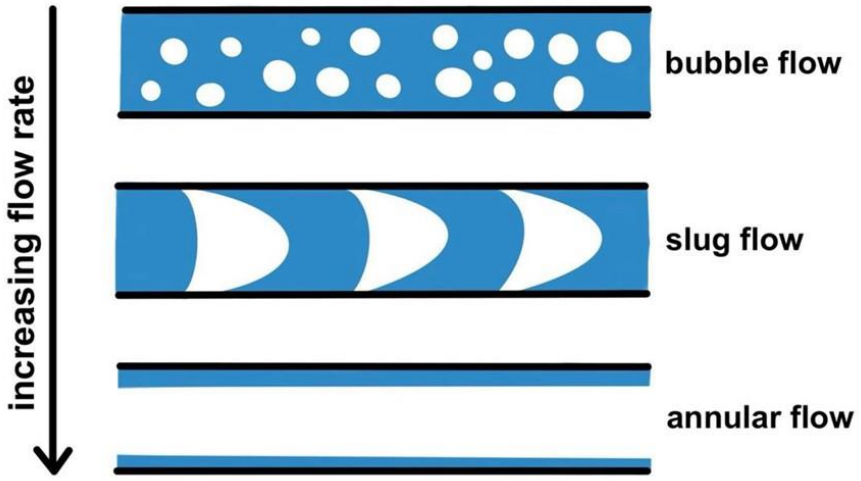

Figure 14: Demonstrates how various flow rates result in different flow regimes, with increasing flow rates leading to the breakup of individual bubbles and a more uniform distribution. This depiction is adapted from figures in the work of Plutschack et al. (57).

To manage and optimize the gas bubbles created in the reaction, increasing the flow rate can break up larger gas bubbles into smaller ones, promoting better mixing and uniformity (62). Implementing external control mechanisms, such as pressure adjustments, can also regulate bubble formation and segmentation. By carefully managing these factors, gas-liquid segmented flow can be leveraged to improve mixing, reduce axial dispersion, and achieve a more consistent nanoparticle size distribution, resulting in higher quality NPs.

1.7.5 Green Chemistry and Continuous Flow

In recent years, the urgency for more sustainable and environmentally friendly chemical processes has become increasingly clear. Traditional chemical manufacturing often involves hazardous substances, generates significant waste, and consumes large amounts of energy (59, 64). This contributes to environmental pollution, health hazards, and depletion of non-renewable resources. As a result, there is a growing demand for green chemistry practices that minimize these negative impacts.

The term “Green Chemistry" was introduced by P. T. Anastas in 1991 through the US Environmental Protection Agency (65) to promote sustainable development in chemistry and chemical technology. This initiative aimed to reshape the approach to chemical syntheses, processes, and applications in order to reduce health and environmental threats. The guidelines are outlined in the “12 principles of Green Chemistry,” which are detailed in Appendix A.

Continuous flow chemistry offers a promising solution to many of the challenges. CF processes provide enhanced mixing and heat management, improved scalability, and greater energy efficiency. These processes reduce waste generation and solvent use, aligning with the principles of green chemistry (59, 64). By integrating the principles of green chemistry with CF technologies, chemists can develop more efficient, economical, and environmentally friendly chemical processes. This combination not only enhances the sustainability of chemical manufacturing but also aligns with the broader goals of reducing the environmental impact of chemical production.

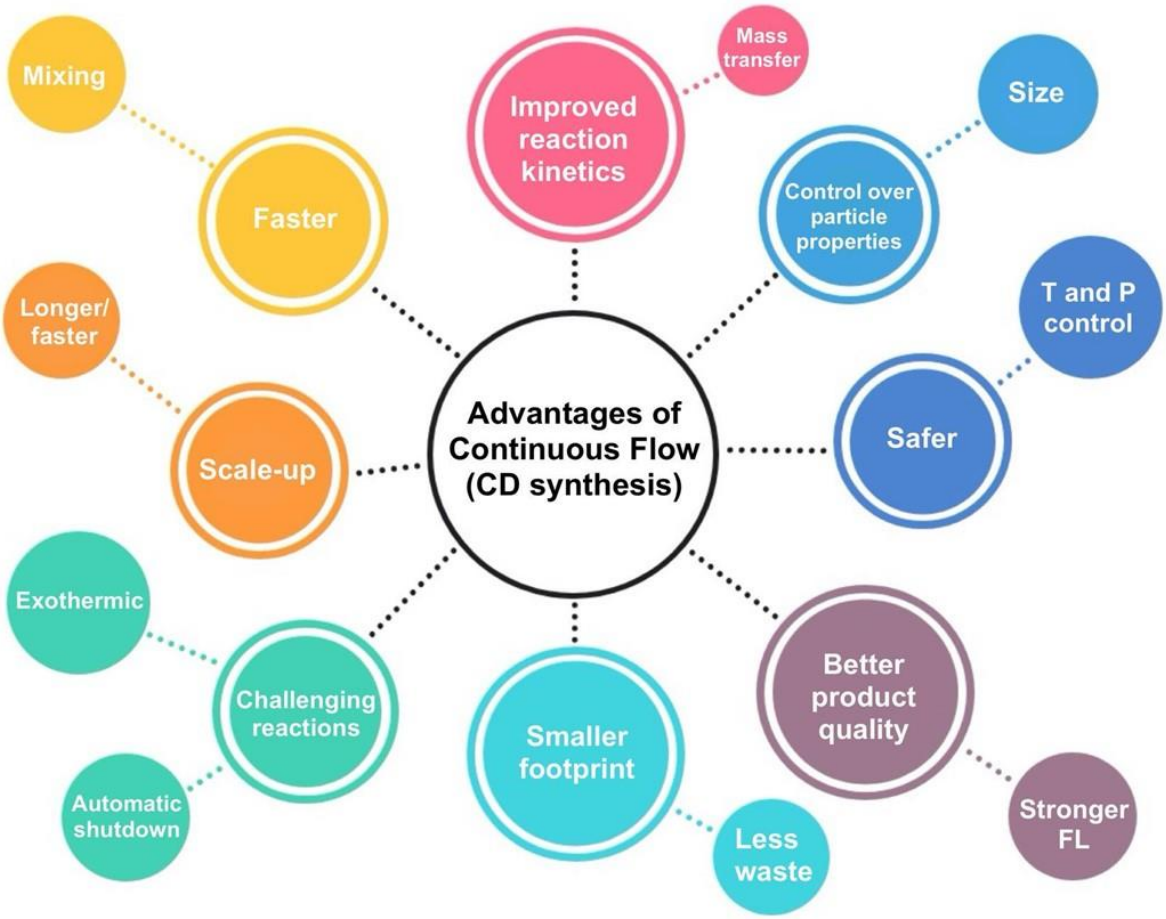

Figure 15: A graphical abstract illustrating a selection of the benefits of synthesizing, particularly CDs, using a CF setup. "T" denotes temperature, "P" indicates pressure, and "FL" represents fluorescence. CF systems offer precise control over reaction conditions, including temperature and pressure, leading to enhanced reproducibility and scalability. Additionally, the CF approach promotes efficient mixing and uniform reaction conditions, resulting in improved product quality and yield. Furthermore, the FL properties of CDs synthesized in CF setups can be finely tuned, offering versatility for various applications in sensing and imaging.

1.8 Objectives

The aim of this thesis is to investigate the production of fluorescent carbon dots using a continuous flow setup and to evaluate the potential advantages of this method over traditional batch techniques.

The main objectives are:

- **Examine the properties of CDs:** Investigate the properties of CDs synthesized from simple precursors, employing environmentally friendly solvents, and using a continuous flow setup. Optimize the reaction parameters (e.g., temperature, flow rate, concentrations) to enhance the quality and yield of the CDs.
- **Comparative study:** Conduct a comparative study of CDs synthesized using traditional batch techniques, specifically utilizing a microwave reactor and a furnace.
- **Comprehensive characterization:** Perform comprehensive characterization of the products using techniques such as Fluorescence (FL) spectroscopy, Ultraviolet-Visible (UV-vis) spectroscopy, Fourier-Transform Infrared spectroscopy (FT-IR), Transmission Electron Microscopy (TEM), Raman spectroscopy, and Dynamic Light Scattering (DLS) to determine the CDs optical and structural properties.

2 Materials and Methods

In this section, the experimental procedures are outlined. The procedures are divided into distinct synthesis methods, incorporating the use of a microwave, a furnace, and a continuous flow setup. Also included are the initial experiments performed using the continuous flow setup. Detailed descriptions of each experimental setup, including materials used, apparatus setups and characterizing methods, are provided. Additionally, any deviations from standard procedures or adaptations made are explicitly addressed.

2.1 Chemicals and Apparatus

Citric acid (CA, $C_6H_8O_7$, Sigma Aldrich, 99%), urea ($CO(NH_2)_2$, Sigma Aldrich, ACS reagent, 99.0-100.5%), ethanol (EtOH, VWR, absolute ethanol, 99.8%), 2-propanol (C_3H_8O, Sigma Aldrich, 99.8%), and sodium chloride (NaCl, 99.5%, Sigma Aldrich) were used as received. Polystyrene microspheres in water (Nanobead NIST traceable size standard, 61.8±0.8 nm, Polysciences Inc.) were used as standards for DLS. All solids were precisely weighed using an analytical balance (Mettler Toledo AX205 DeltaRange or Sartorius BP 2105). Milli-Q water (Millipak Q-pod 18.2 MΩ cm) served as the solvent for all experiments. The fluorescence of the crude product solution was observed at 234 and 366 nm using a CAMAG® UV Cabinet.

2.2 Synthesis of CDs in a Microwave

The microwave experiments served as an alternative batch method to complement the continuous flow setup for result comparison. For all microwave experiments, a Biotage Initator+ microwave synthesizer equipped with 20 mL Biotage microwave reaction vials were used.

2.2.1 Microwave Synthesis: General Procedure

Various amounts of citric acid and urea were dissolved in water (10 mL) and transferred to Biotage microwave reaction vials (20 mL), along with a stirring magnet. The vials were then placed in the microwave synthesizer. The experiments were set to last for 5 minutes at 200 °C. The stirring rate was 600 rpm. After completion, the reaction mixture was purified using the dialysis method outlined in section 2.5.

Table 1: The experimental parameters and conditions for the microwave experiments, detailing the time, concentration, molar ratio and resulting color of the product. The temperature was set to 200 °C.

Name	t [min]	[CA] [M]	[Urea] [M]	Molar Ratio CA : urea
MW-1	5	0.1	-	-
MW-2	5	0.1	0.04	1 : 0.4
MW-3	5	0.1	0.08	1 : 0.8
MW-4	5	0.1	0.10	1 : 1.0
MW-5	30	3.2	-	-
MW-6	30	3.2	-	-

2.3 Synthesis of CDs Using a Furnace

The furnace experiments offered an additional batch method to compare with and complement the continuous flow method. These experiments were conducted using a Nabertherm L3/11 furnace equipped with the basic controller B400/B410.

2.3.1 Furnace Technique: General Procedure

Citric acid (3 M) and urea (0-3 M) were dissolved in water (1.6 mL) and transferred to a porcelain crucible. The crucible was placed in the furnace and heated gradually from room temperature, increasing at a rate of 5 °C/min until reaching 200 °C, where it was maintained for 2 hours. The resulting product was then collected, dissolved in water (10-12 mL), and transferred to centrifuge tubes (15 mL). After centrifugation at 8000 rpm for 30 minutes, the reaction mixture was purified using the dialysis method described in section 2.5.

Table 2: The experimental parameters and conditions for the experiments conducted with a furnace, detailing the time, reactant concentrations, and molar ratio. The temperature was set to 200 °C.

Name	t [min]	[CA] [M]	[Urea] [M]	Molar Ratio CA : urea
F-1	120	2.9	-	-
F-2	120	3.0	0.46	1 : 0.2
F-3	120	3.5	-	-
F-4	120	3.0	0.69	1 : 0.2
F-5	120	4.6	-	-
F-6	120	2.9	0.80	1 : 0.3
F-7	120	3.0	1.62	1 : 0.5
F-8	120	3.0	2.87	1 : 0.9

2.4 Synthesis of CDs using a Continuous Flow Setup

In all continuous flow experiments, the Vapourtec RS-400-series was employed. The experiments were managed through the Vapourtec "R-series software" (version v1.3.0.28), and the reactor utilized was a high-temperature tube reactor (10 mL coil). For the preliminary experiments, a

micromixer (50-1273, Lab-MS Glass micromixer chip) facilitated the mixing process and involved the incorporation of an autosampler (Gilson X271) for both sample injection and product collection.

Figure 16: The RS-400 series comes equipped with two R-series pump modules, R-series software, and a selection of reactors, including the high-temperature coil reactor. Additionally, it features the Gilson X271 autosampler, providing options for both injection and collection. The images are obtained from the Vapourtec website (66).

2.4.1 Continuous Flow Setup: Vapourtec RS-400 System

The RS-400 is a commercially available continuous flow setup manufactured by Vapourtec. Complete with fully automated control, an autosampler/collector, four pumps, and multiple reactors, it streamlines reaction processes. The R-series software enables for conducting reactions seamlessly and autonomously, facilitating unattended operation. The software also facilitates data logging, storage, and visualization, including concentration curves and real-time pressure monitoring, enhancing efficiency and control in experimental workflows.

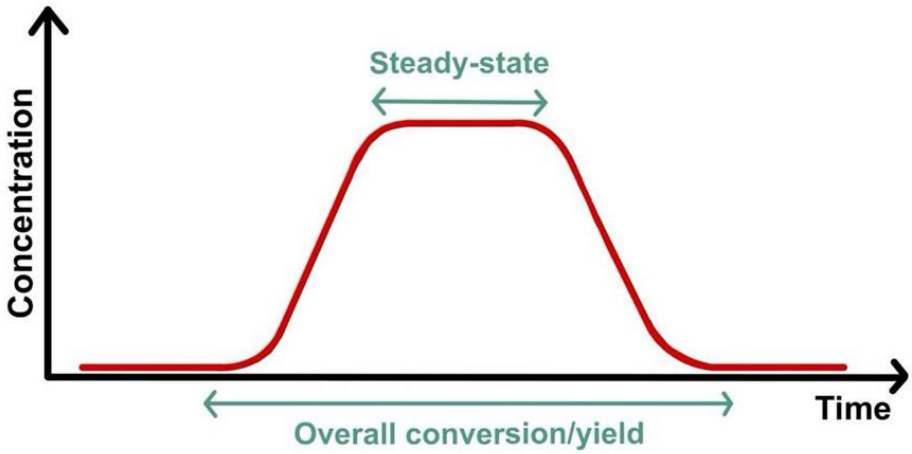

Figure 17: Illustration of steady-state conditions.

An essential difference between batch and CF chemistry lies how concentrations change. According to the Hitchhiker's Guide to Flow Chemistry by Plutschack et al. (57), in a batch reactor, the concentration of reactants uniformly decreases over time. In contrast, in continuous flow reactions, the concentration of the starting material decreases along length of the reactor, reaching a minimum at the end. Ideally, this dependency on length results to constant reactant and product concentrations at specific positions known as the steady state, as illustrated in Figure 17.

2.4.2 Continuous Flow Synthesis: General Procedure

Solution A containing citric acid and urea in water was prepared. The Vapourtec system was purged before initiating the reaction at 200 °C. The solution was pumped at different flow rates. The resulting product mixture was then collected and purified using the dialysis method outlined in section 2.5.

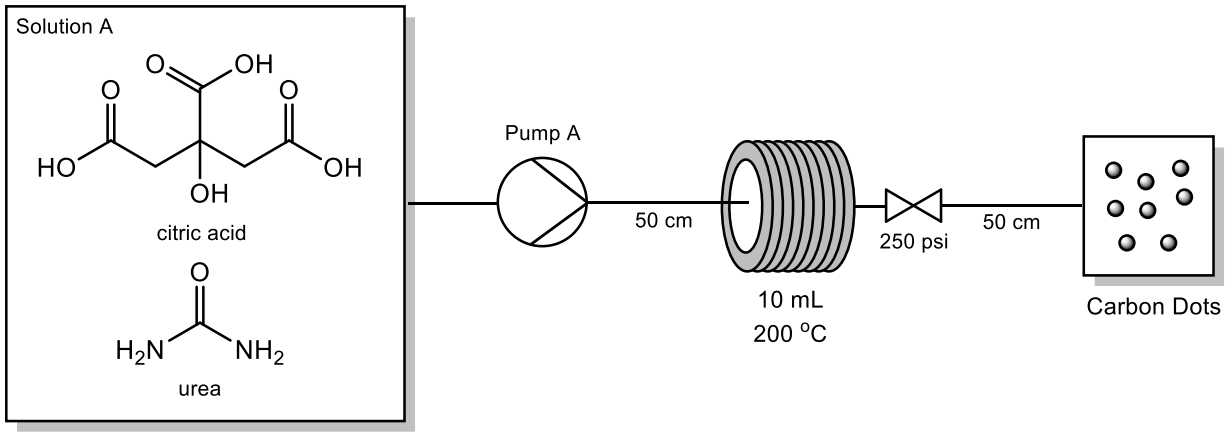

Figure 18: Sketch of the continuous flow setup: Solution A is pumped through the high-temperature coil reactor (200 °C). A back pressure regulator (250 psi) ensures that the water is kept in the liquid state even at temperatures above the normal boiling point.

Table 3: The experimental parameters and conditions for the continuous flow setup experiments. τ denotes the residence time with the high-temperature reactor set at 200 °C.

Name	τ [min]	F_R [mL/min]	[CA] [M]	[Urea] [M]	Molar Ratio CA : urea
CF-1	60	0.17	3.25	-	-
CF-2	120	0.08	3.25	-	-
CF-3	60	0.17	3.25	0.35	1 : 0.1
CF-4	60	0.17	3.25	1.04	1 : 0.3
CF-5	60	0.17	2.01	135	1 : 0.7
CF-6	60	0.17	2.01	1.99	1 : 1.0
CF-7	60	0.17	2.01	1.99	1 : 1.0
CF-8a	5	2.00	1.00	1.03	1 : 1.0
CF-8b	5	2.00	-[a]	-	-
CF-9a	15	0.67	1.00	1.03	1 : 1.0
CF-9b	15	0.67	-	-	-
CF-10a	30	0.33	1.00	1.03	1 : 1.0
CF-10b	30	0.33	-	-	-
CF-11a	60	0.17	1.00	1.03	1 : 1.0
CF-11b	60	0.17	-	-	-

a) CF-8b, -9b, -10b, and -11b denote experiments where the concentrations of CA and urea were not precisely determined. This is attributed to the utilization of the product from CF-8a, -9a, 10a, and -11a, respectively, as the reactant for the subsequent experiment (see further details in chapter 2.4.4 Cascade Experiments".

2.4.3 Preliminary Experiments

These experiments were conducted to evaluate the feasibility and outcomes of producing CDs using the CF setup, with particular focus on revealing any unforeseen effects of system utilization or reactant behavior. Additionally, the autosampler functionality of the Vapourtec was integrated to the system to automate the synthesis process and enhance operational proficiency. Considering the limited utilization of the system by others, it provided an intriguing opportunity to become acquainted with its operation.

Procedure

Solutions A (citric acid in water) and B (urea in water) were prepared. The Vapourtec system was purged before initiating the reaction at 200 °C. Solutions A and B were pumped in a 1:1 ratio and at different total flow rates. The resulting product mixture was then collected and purified using the dialysis method as outlined in section 2.5.

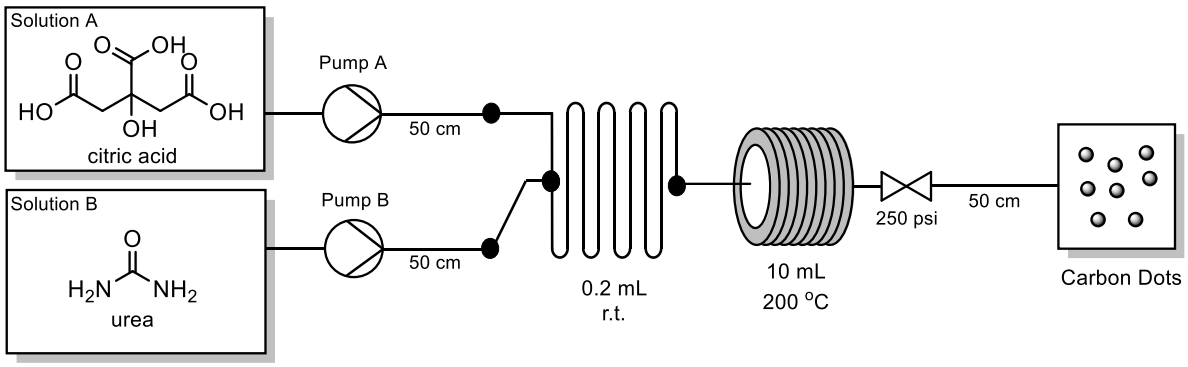

Figure 19: The continuous flow setup operates as follows: Each reactant solution was pumped through the micromixer (50-1273, Lab-MS). The mixture was conveyed to the high-temperature coil reactor (200 °C). Collection was automated through an autosampler.

Table 4: The experimental parameters and conditions for the preliminary experiments. The provided flow rate (F_R) represents the combined flow rate of both pumps utilized in the setup. τ denotes the residence time in the coil reactor. The temperature is 200 °C.

Name	τ [min]	F_R [mL/min]	[CA] [M]	[Urea] [M]	Molar Ratio CA : urea
P-1	10	1.0	0.20	0.02	1 : 0.1
P-2	10	1.0	0.06	0.02	1 : 0.3
P-3	10	1.0	0.03	0.02	1 : 0.7
P-4	10	1.0	0.02	0.02	1 : 1.0
P-5	10	1.0	0.06	0.08	1 : 1.5
P-6	10	1.0	0.11	0.14	1 : 1.2
P-7	10	1.0	0.21	0.22	1 : 1.0
P-8	10	1.0	0.31	0.36	1 : 1.2
P-9	10	1.0	0.41	0.42	1 : 1.0
P-10	33	0.3	0.41	0.42	1 : 1.0
P-11	33	0.3	0.11	0.14	1 : 1.2
P-12	17	0.6	0.04	0.06	1 : 1.5
P-13	17	0.6	0.10	0.10	1 : 1.0
P-14	17	0.6	0.20	0.20	1 : 1.0
P-15	17	0.6	0.30	0.32	1 : 1.0
P-16	17	0.6	0.40	0.42	1 : 1.0

2.4.4 Cascade Experiments

Continuous flow cascade (67) experiments were conducted to explore the potential for reducing gas production, with the goal of enabling the formation of more well-defined carbon cores. These experiments were necessary due to the challenges posed by gas evolution during the reactions, which affected flow rate, residence time, and product collection.

The premise involved passing the product solution through the reactor for an additional cycle under similar reaction conditions to the initial run. The experimental setup mirrored the description provided in section 2.4.2, with the notable difference being that the product from the first run served as the reactant solution for the subsequent run.

The experiments from the first run correspond to "CF-Xa" in Table 3, while the samples from the second run correspond to "CF-Xb".

2.5 Purification of Carbon Dots: Dialysis

The preparation of CDs often results in a mixture containing various emissive and non-emissive molecular-like side products, which can significantly affect the optical properties and performance of the CDs (2, 33). Proper purification is crucial to ensure that the properties of the CDs are accurately characterized and optimized for the intended applications.

Dialysis is the most common method for purifying CDs (2, 33). Ullal et al. (20) published a review highlighting the importance of proper purification and separation of CDs, emphasizing that no standard technique exists for this purpose. Impurities and side products from unreacted precursors and other fluorophores can lead to misinterpretation of PL properties. Therefore, purification is essential to separate the CDs from byproducts and prevent errors caused by interference from these fluorophores.

While dialysis effectively removes unreacted reactants and molecular-like side products, it does not separate CDs of different sizes or surface functional groups (33). Additionally, there is currently no standard protocol for the duration of dialysis or the molecular weight cut-off (MWCO) of the dialysis membrane.

A study by Chen et al. (33) concluded that the dialysis process should last a minimum of 120 hours to completely remove all side products, and that an MWCO of less than 1 kDa is insufficient to effectively remove these side products. Despite these findings, the CD samples in this paper were dialyzed for shorter durations: 72 hours for most samples and 48 hours for some, using a 2000 Da MWCO membrane. Specifically, samples CF-3/3*, CF-6/6*, and CD-7 were dialyzed for 48 hours.

2.5.1 Dialysis Procedure

Every sample underwent dialysis for a minimum of 48 hours. Most of the samples were dialyzed for 72 hours. The product was transferred into a 2000 Da MWCO dialysis tube (benzolated, Sigma Aldrich) and submerged in approximately 800-1000 mL of water, which was replaced every 24 hours. After dialysis, the product was freeze-dried and stored for subsequent analysis.

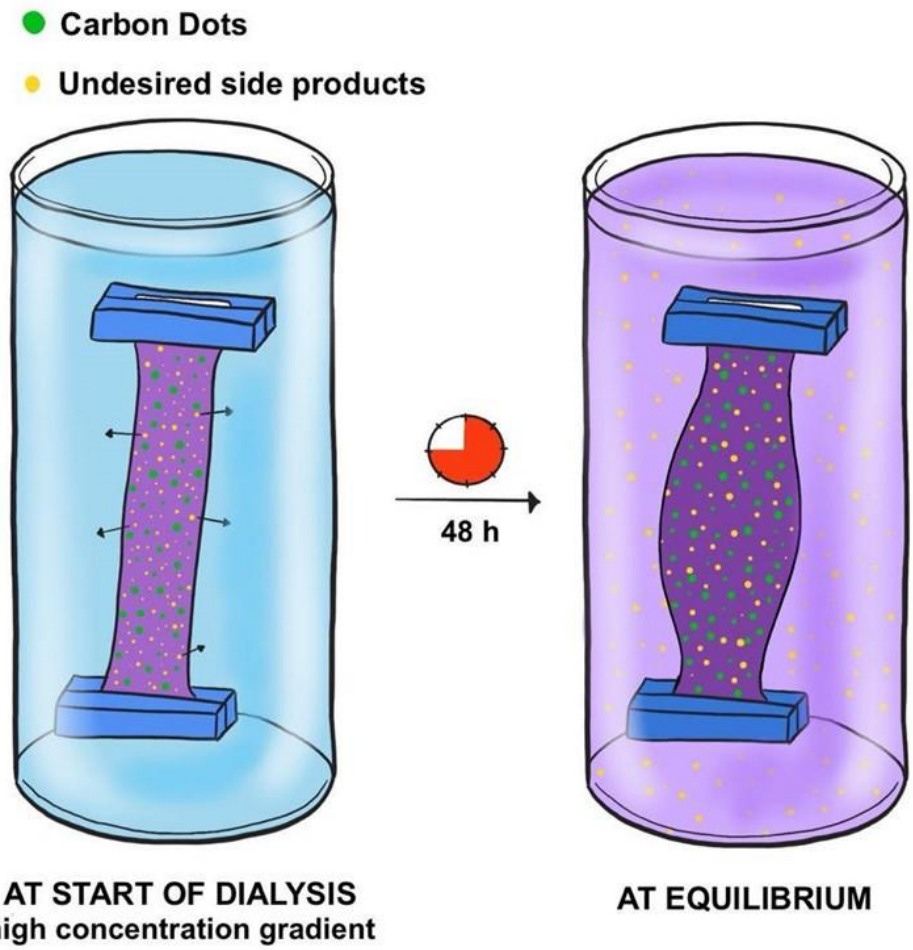

Figure 20: Dialysis Setup: The dialysis purification setup involved transferring the sample in a dialysis tubing to a container filled with water. The dialysis tubing is as a semi-permeable membrane, allowing small molecules (undesired side products) to pass through while retaining larger ones (CDs). The procedure hinges on diffusion and osmosis, whereby impurities migrate from the sample through the membrane into the water, while water permeates into the tubing.

This approach balanced the need for thorough purification with practical considerations such as time constraints and the specific requirements of the experiments. The 2000 MWCO membrane was chosen to remove most molecular-like byproducts within a reasonable time frame. Although not adhering strictly to the 120-hour recommendation, this method aimed to achieve high purity within experimental constraints. Future studies could further optimize dialysis conditions to align more closely with recommendations, potentially improving the consistency and reliability of the results.

2.6 Characterization Techniques

This section provides a detailed description of the methods employed to characterize the CDs. The methods include fluorescence spectroscopy, UV-visible spectroscopy (UV-vis), Raman spectroscopy, Fourier-transform infrared spectroscopy (FT-IR), dynamic light scattering (DLS), and transmission electron microscopy (TEM). By combining these techniques, the aim is to provide insights into the structural composition, size distributions and fluorescence properties of the CDs.

This review is based on the works of Atkins and de Paula (16), Leng et al. (68), and Pavia et al. (69). Additionally, when applicable, information from the manuals provided by the instrument manufacturer is used.

As with purification, there is no standard set of techniques for characterizing CDs. The methods presented here are a subset of those available and are chosen for their accessibility and ease of use.

2.6.1 Fluorescence Spectroscopy

Fluorescence spectroscopy examines the fluorescent properties of a sample by using a laser to excite the electrons, causing them to emit light. Based on the manuals provided by Tecan, this is how the principles behind its operation function (70). The emitted light is collected by a detector after passing through a filter. The outcome is a steady-state FL spectrum, which measures the intensity of emitted photons as a function of wavelength when the molecules are excited by a consistent light source. This involves scanning the emission wavelength while maintaining a constant excitation wavelength. This technique can distinguish between single-particle CDs and mixtures, with a wider bandwidth indicating mixed populations (2).

Each purified CD sample was dissolved water. 100 μL of the solutions were transferred to a black 96-well plate (Thermo Scientific™). Fluorescence measurements were performed using a Tecan (SPARK) 96-well plate reader. Maximum excitation and emission fluorescence profiles of the CDs were generated with 2 nm incremental excitation steps ranging from 280 to 460 nm. For further instrument settings, refer to appendix C.

2.6.2 Ultraviolet-Visible Spectroscopy

In the ultraviolet-visible (UV-vis) spectrum, wavelengths ranging from 190 nm to 800 nm are typically examined. Although most organic molecules exhibit transparency within this range, certain molecules absorb energy, offering valuable insights into the structures (69).

When photons traverse a transparent substance, they may be absorbed, resulting in an absorption spectrum (69). This absorption leads to the transition of a molecule or atom from its ground state

to a higher, excited state, a process that is quantized. This quantization signifies that the energy difference between the ground and excited states corresponds precisely to the energy of the absorbed electromagnetic radiation.

Typically, during excitation, electrons move from the Highest Occupied Molecular Orbital (HOMO) to the Lowest Unoccupied Molecular Orbital (LUMO) (69). The HOMO commonly encompasses the lowest energy occupied molecular orbitals, such as σ and π orbitals, with nonbonding (n) orbitals holding unshared pairs. Conversely, the LUMO comprises antibonding orbitals, including σ* and π* orbitals, as illustrated in Figure 21.

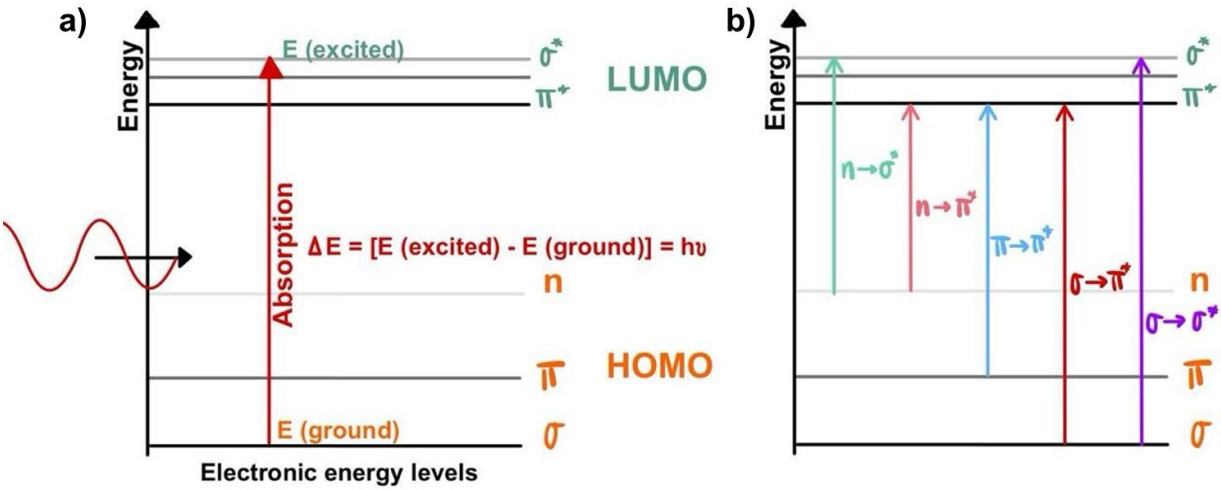

Figure 21: Illustrating the electronic excitation process. a) The process of electronic excitation involves the absorption of a photon, leading to the transition of an electron from the Highest Occupied Molecular Orbital (HOMO) to the Lowest Unoccupied Molecular Orbital (LUMO). b) Illustrating the typical energy absorption transitions. Based on figures from Pavia et al. (69) with modifications.

Each compounds undergoes specific transitions. In the case of CDs, two important transitions are observed: n→π* transitions, corresponding to carbonyl compounds, and π→π* transitions, which pertain to aromatic sp^2 bonds (69, 71, 72). For a given molecule, numerous possible transitions occur, resulting in a broad band structure with absorption predominantly centered around the most prevalent transitions (69).

$$A = \log\left(\frac{I_0}{I}\right) = \varepsilon c l \qquad \text{Equation 2.1}$$

The fundamental principle underlying UV-vis spectroscopy is elucidated by Beer-Lambert's law (equation 2.1), where A denotes absorbance, equal to $\log\left(\frac{I_0}{I}\right)$. The molar absorptivity, ε, is an inherent molecular property of the substance undergoing an electronic transition. Here, I_0 and I represent the intensity of incident light and light exiting the sample cell, respectively, while l signifies the length of the sample cell and c denotes the concentration of the substance.

A spectrophotometer comprises a light source, monochromator, and a detector. The light source emits electromagnetic radiation within the UV-vis region, while the monochromator spreads the light into its constituent wavelengths (69). The light passes through the sample cell, with the detector measuring the light reaching it. In this setup, a double-beam instrument was employed, concurrently measuring a reference sample (solvent). While glass or plastic cuvettes are suitable for visible range measurements, quartz is recommended for UV measurements to prevent material absorption (69).

Each purified CD sample was dissolved in water and the solution was transferred to a plastic cuvette (cuvette Kartell S.P.A. 10x10x45 mm std). Analyses were conducted using a Shimadzu UV-1800 spectrophotometer, measuring wavelengths from 250 nm to 800 nm.

2.6.3 Raman Spectroscopy

Raman spectroscopy enables the examination of rotational and vibrational transitions within substances, arising from collisions between molecules and photons, altering the vibrational and rotational states (16). For a Raman transition to occur, there must be a change in molecular polarizability as the molecule vibrates.

In a Raman spectrometer setup, a light source emitting a specific wavelength is directed through a lens and subsequently through a small aperture in a mirror possessing a curved reflective surface (16). Upon reaching the front of the sample, the light beam undergoes scattering, while the mirror simultaneously deflects and concentrates the rays towards a monochromator. The dimensions of the aperture of the monochromator are determined by the analysis parameters. Finally, a detector measures the intensity of the light passing through.

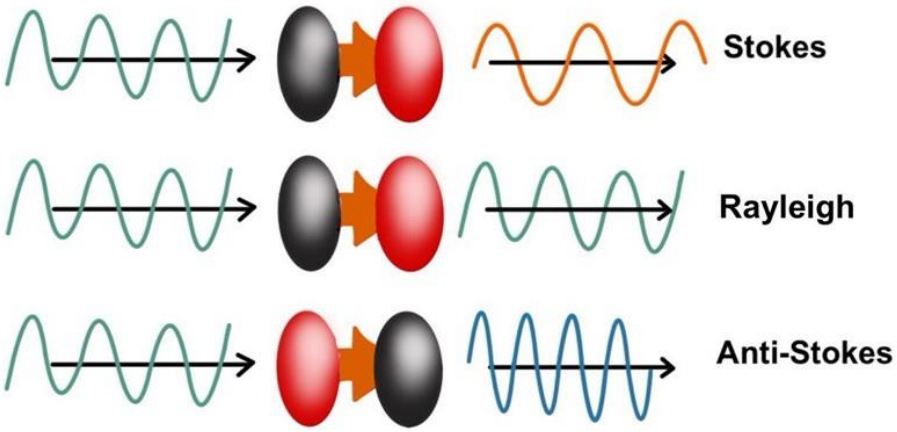

Figure 22: Raman scattering. The illustration depicts three distinct scatter mechanisms through which incident light interacts with molecules, leading to the generation of three types of radiation: Stokes, Rayleigh, and Anti-Stokes radiation. Recreated based on figures from Atkins et al. (16).

Figure 22 illustrates the scattering mechanism of Raman spectroscopy, depicting photon-molecule interactions through scattering. Stokes radiation is the most common scattering mechanism, involving a loss of energy as photons collide with molecules, resulting in a lower energy state. Rayleigh radiation occurs when scattered photons keep the original energy. Anti-Stokes radiation involves photons gaining energy from molecular collision, leading to an increase in energy and frequency.

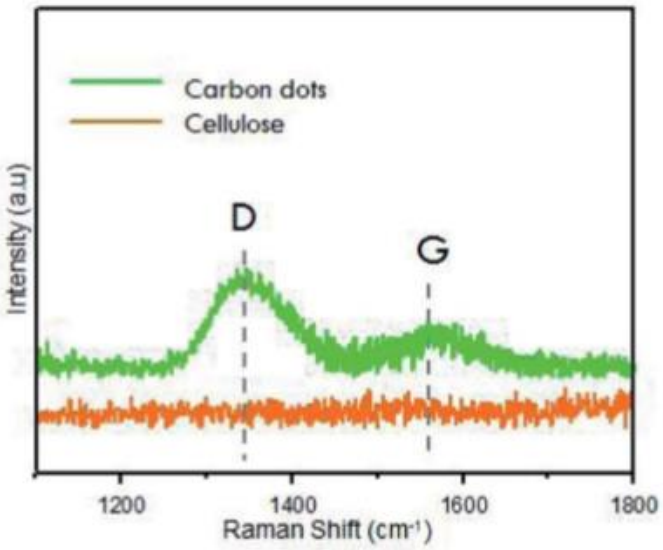

Figure 23: Illustrative Raman Spectrum. Raman spectrum showcases the D-band and the G-band, sourced from the review of Rooj and Mandal on CD characterization (73).

In a typical Raman spectrum of CDs, two main bands are of interest: the D-band, typically around 1350 cm^{-1} and the G-band, usually around 1585 cm^{-1} (25, 72-74). Generally, sp^2 carbon bonds, being easily polarizable π-bonds, are Raman-active. The D-band is attributed to disordered sp^3 hybridized carbon atoms at the surface, while the G-band represents the in-plane stretching of C=C, which is a signature of sp^2 hybridized carbon atoms (25, 73).

For the analyses, a RamanRXN Analyzer from Kaiser Optical Systems Inc. was employed, utilizing an excitation wavelength of 785 nm. Each scan was repeated five times, and an average spectrum was obtained within an acquisition time of 100 ms. Both a non-contact sampler probe, an immersion probe, for solutions and a ball probe for solid samples were used.

2.6.4 Fourier-Transform Infrared Spectroscopy

Most covalently bonded compounds absorb electromagnetic radiation within the infrared range, which spans wavelengths longer than those in the visible spectrum but shorter than microwaves (69). Of particular interest within this spectrum is the vibrational domain, ranging from 2.5 µm to 25 µm, commonly denoted as wavenumber ($\bar{v}$) and expressed in reciprocal centimeters (equation 2.2).

$$\bar{v}(cm^{-1}) = \frac{1}{\lambda(cm)}$$ Equation 2.2

Infrared absorption, akin to other absorption phenomena, is quantized, with radiation energy corresponding to the stretching and bending vibrational frequencies of covalent bonds (69). For absorption to occur, the bond must possess an electrical dipole moment that oscillates at the same frequency as the incoming radiation.

The primary vibrational modes in molecules, which are infrared active, are stretching and bending, with the origins of IR stretches and bends explained in Figure 24.

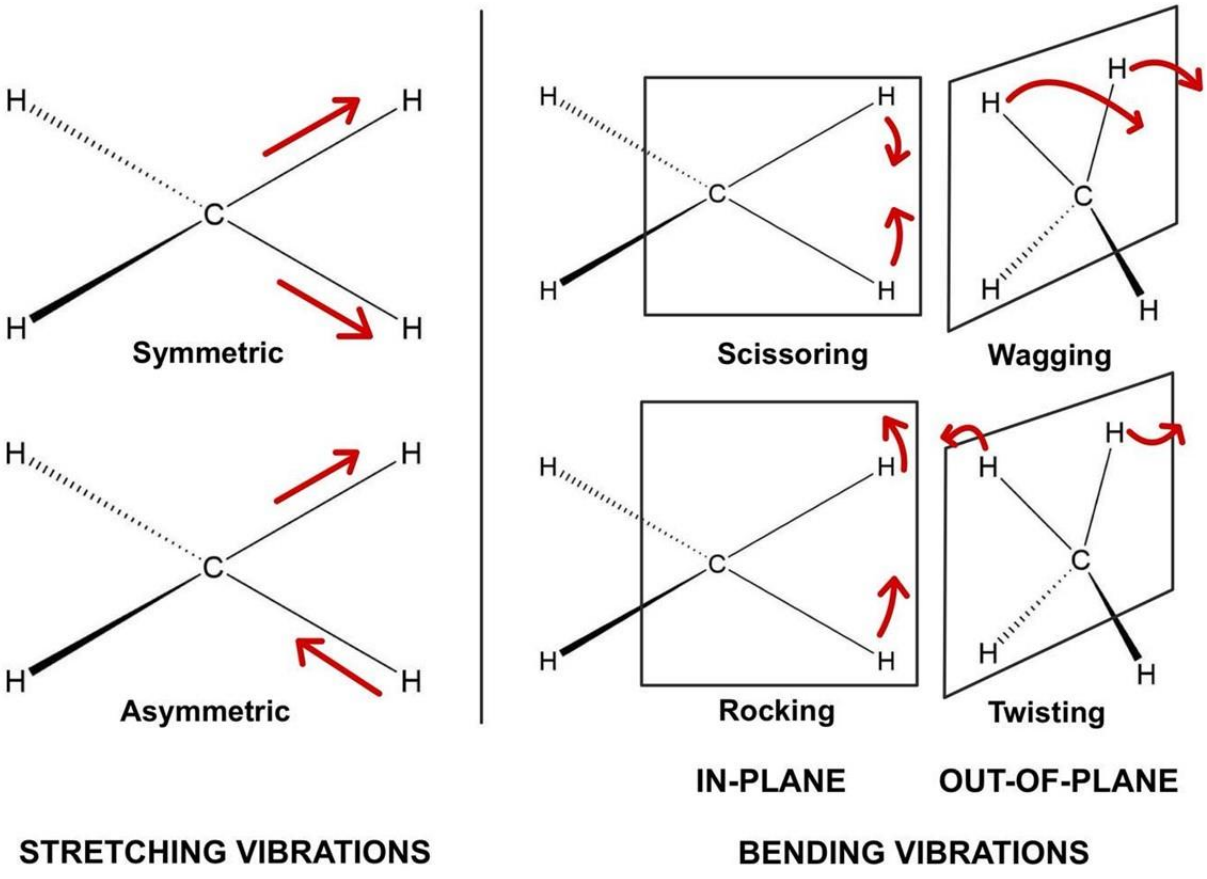

Figure 24: Most common IR stretching and bending vibrations. Recreated from Pavia et. al. (69).

Measurements were conducted using a Fourier-Transform Infrared (FT-IR) spectrometer, which generates an interferogram – a wave-like pattern containing all IR spectrum frequencies (69). Fourier-Transform mathematically separates the individual absorption frequencies from the interferogram, enabling rapid analyses and improving signal-to-noise ratio (S/N) by summing interferograms from the same sample.

The method employed for CD sample spectrum determination is attenuated total reflectance (ATR), which eliminates sample preparation and facilitates rapid analyses (69). Using a diamond ATR, samples are placed directly on the diamond. The incoming IR beam bounces back and forth, penetrating the sample slightly and causing absorption of its vibrational frequencies, thus resulting in beam attenuation (69, 75). This process is illustrated in Figure 25.

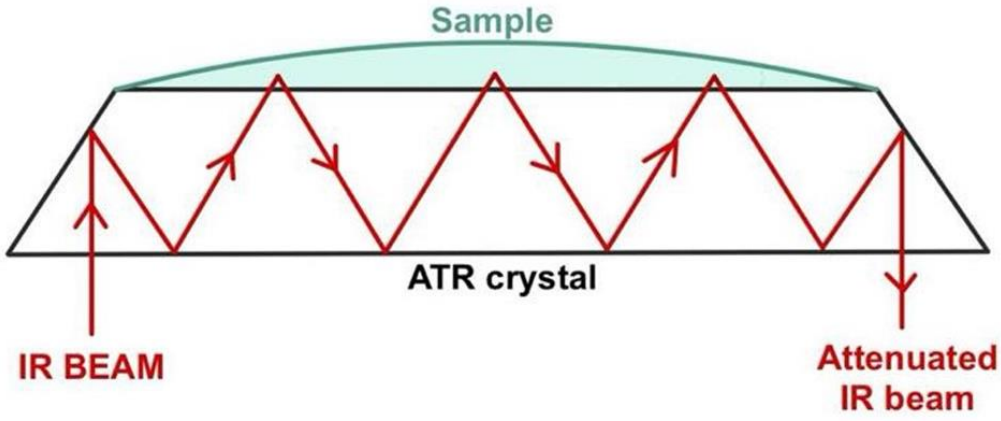

Figure 25: Illustration of the ATR technique where the sample is placed directly on the crystal. The IR beam penetrates the sample slightly, allowing for the absorption of vibrational frequencies, leading to beam attenuation. Recreated based on figures from Pavia et al. (69) with modifications.

The experiments were analyzed with the Thermo Scientific Nicolet iS50R FT-IR instrument equipped with the single reflection ATR technique and a diamond crystal. Each spectrum was an average of 32 scans to achieve a good S/N, at an optical resolution of 4.0 cm^{-1}.

2.6.5 Transmission Electron Microscopy

Images with higher magnification and resolution compared to conventional light microscopes can be obtained using a transmission electron microscope (TEM) (68). This facilitates the exploration and examination of the morphology and size of CDs. The TEM system emits a high-energy electron beam, accelerated by a voltage of 160 kilovolts (kV). The choice of acceleration voltage directly impacts the resolution, with electron wavelengths shorter than visible light, enabling the microscope to reveal finer details.

To reduce potential interactions between the electron beam and extraneous elements beyond the sample, a high vacuum environment is established within the TEM column (76). As the electrons pass through the specimen, they interact with the atoms, undergoing various scattering processes. The interactions cause alterations in the intensity and trajectory of the electron beam, which are captured by detectors to construct an image (77).

TEM sample preparation and imaging were conducted by Irene Heggstad at the Electron Microscopic Laboratory of the University of Bergen. The specimens were prepared by placing a drop of CDs suspended in isopropanol onto a copper 100/200 mesh grid, coated with carbon on a Formivar layer. Following deposition, the samples were allowed to air-dry under ambient conditions. Subsequent imaging and analysis were executed employing a Jeol JEM-2100 transmission electron microscope, operating at an accelerating voltage of 160 kV.

2.6.6 Dynamic Light Scattering

Dynamic light scattering (DLS), as described in the manuals provided by Malvern Instruments, is used to measure the Brownian motion of particles and correlate it with the size (78). This method involves illuminating the sample with a laser, measuring the scattered light in all directions, and determining the particle size corresponding to the diffusion rate of the measured particle. Brownian motion, defined as the random movement of particles due to molecular bombardment, is central to this process.

The relationship between particle size and Brownian motion is expressed in the Stokes-Einstein equation (equation 2.3), incorporating parameters such as Boltzmann constant (k_B), temperature (T), viscosity (η), particle radius (r), and diffusion constant (D).

$$D = \frac{k_B T}{6\pi\eta r} \qquad \text{Equation 2.3}$$

Particles with slower movement and consistent positions over time will appear larger, while those with faster movement and rapidly changing positions will appear smaller (78). A digital correlator within the instrument evaluates the correlation between signals over time (see Figure 26), with decreasing correlation attributed to Brownian motion, resulting in the calculation of particle size. Perfect correlation scores as 1 and no correlation as 0.

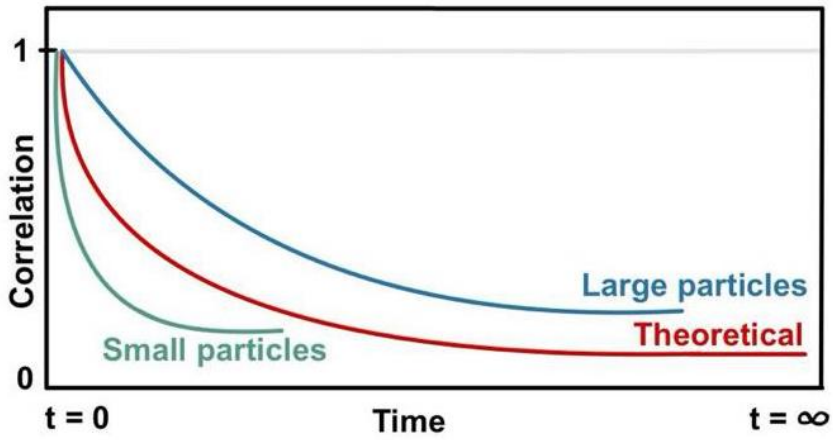

Figure 26: Correlation functions for small and large particles. The graph illustrates the correlation function for small and large particles. Based on the manuals by Malvern Instruments (78) with modifications.

The program generates a Z-average size and a polydispersity index (PDI), suitable for monodisperse, spherical particles with a single peak (78). Additionally, it provides individual peaks by size and percentage. The PDI is recommended to be below 0.1 for reliable results. However, if the PDI is over 0.5 it is unwise to use the Z-average mean.

Each CD sample was diluted to achieve a light-colored solution, with varying dilution factors. The measurements were conducted on a Malvern Zetasizer Nano series instrument. The instrument settings were configured to the "general purpose" analysis mode, with the number of runs set to automatic, allowing the instrument to determine the optimal number of runs based on the particle solution. The refractive index was set to 1.330 for the solvent (water) and 1.500 for the CD solution.

Assessing Instrument Precision: Incorporating Polystyrene Microspheres for Size Validation

To ascertain the precision of the instrument, experiments were conducted incorporating polystyrene microspheres suspended in water into the measurement solution. The expected size of these particles was 61.8±0.8 nm.

The polystyrene solution, containing polystyrene particles (3 drops) and NaCl (10 mM), was dissolved in water (100 mL). Subsequently, 3 drops of this solution were added to the prepared product solution and measured alongside other analyses.

This step aimed to verify the accuracy of the instrument by comparing the measured size with the theoretical size provided by the producers. Any deviation would prompt adjustments to the viscosity of the solvent to correct for the error.

3 Results

In this chapter, the results derived from the experiments will be presented. The presentation follows a chronological order, commencing with the microwave experiments, followed by the furnace experiments, and concluding with the continuous flow setup experiments. Each section starts by explaining the purpose of each experiment, followed by a detailed description of the experiments and the respective outcomes. All analyses are performed on dialyzed samples, except where noted. Throughout the presentation of the results, the effectiveness and limitations of the characterization methods will be addressed where relevant. A more detailed discussion of these aspects will follow in the subsequent discussion section (chapter 4).

3.1 Synthesis of CDs in a Microwave

The microwave synthetic pathway provided an alternate batch approach to supplement the continuous flow setup for comparative analysis. Each experiment is detailed in Table 5 below, presenting key parameters such as reaction time, molar ratio, and the resultant color of the product. Color assessment, being subjective, was conducted immediately after the product exited the synthesizer.

Table 5: Parameters and conditions employed for the MW-samples, including reaction time, molar ratio, and resulting color of the product. The temperature was set to 200 °C.

Name	t [min]	Molar Ratio CA : urea	Color
MW-1	5	-	colorless
MW-2	5	1 : 0.4	yellow with hints of purple
MW-3	5	1 : 0.8	purple with hints of brown
MW-4	5	1 : 1.0	brown shading towards purple
MW-5	30	-	purple with hints of yellow
MW-6	30	-	brown with hints of yellow

MW-1 to MW-4 represent experiments exploring various molar ratios of CA and urea. MW-5 and MW-6 are attempts to increase the concentration of CA. A screenshot of a typical instrument report post-reaction can be found in Appendix B. Figure 27 provides photos of the samples.

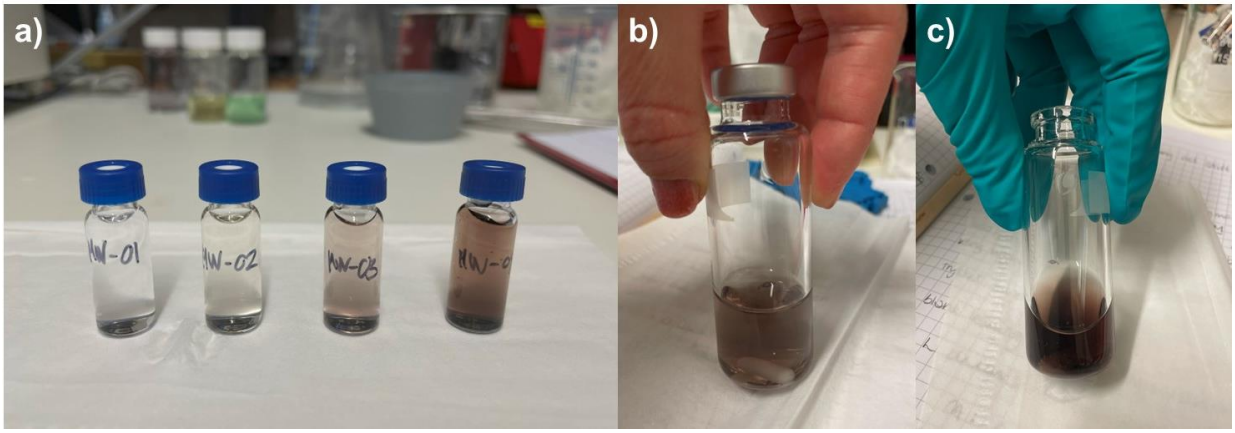

Figure 27: Product solutions obtained using microwave synthesis. a) Photo of solutions with varying ratios of CA to urea, increasing from left to right towards a 1:1 ratio. b) Photo of MW-3, displaying a purplish hue with subtle brown undertones. c) Photo of MW-4, showing a brown color transitioning towards purple tones.

3.1.1 FL Spectroscopy

The FL emission spectra are displayed in Figure 28 below. With a maximum excitation wavelength of 280 nm, Figure 28a showcases the emission spectra under varying excitation wavelengths. Similar observations were made for the other samples prepared using the MW method.

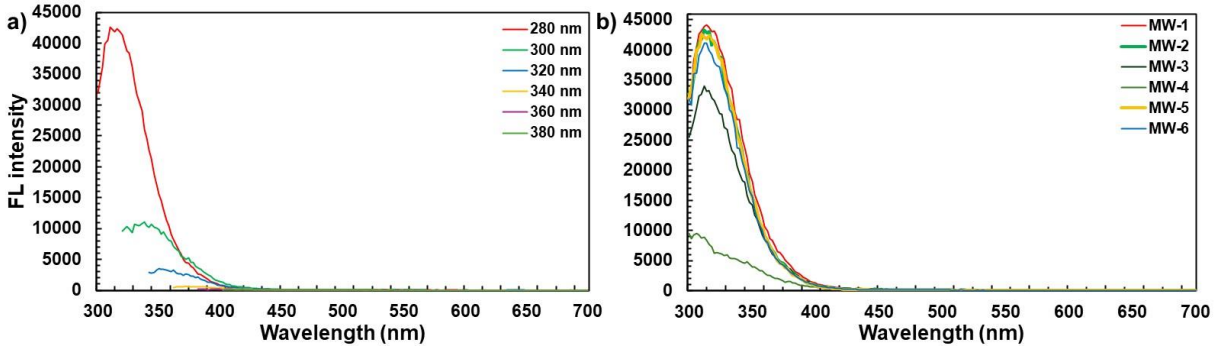

Figure 28: FL emission spectra for the microwave experiments. a) Emission spectra for experiment MW-6 depicting varying excitation wavelengths. b) Emission fluorescence spectra for the MW experiments were recorded at an excitation wavelength of 280 nm, corresponding to the maximum emission wavelength observed across all MW samples.

The bar diagram (Figure 29) illustrates the excitation-dependent emission characteristics of samples synthesized using the MW synthesizer. Each bar represents a different sample and indicates the excitation wavelength at which maximum emission occurs.

Accompanying the bar graph is a blue line graph depicting the respective FL intensity of each sample. This line offers insights into the relative maximum FL intensities observed, with MW-4 standing out as the only sample exhibiting low FL intensity.

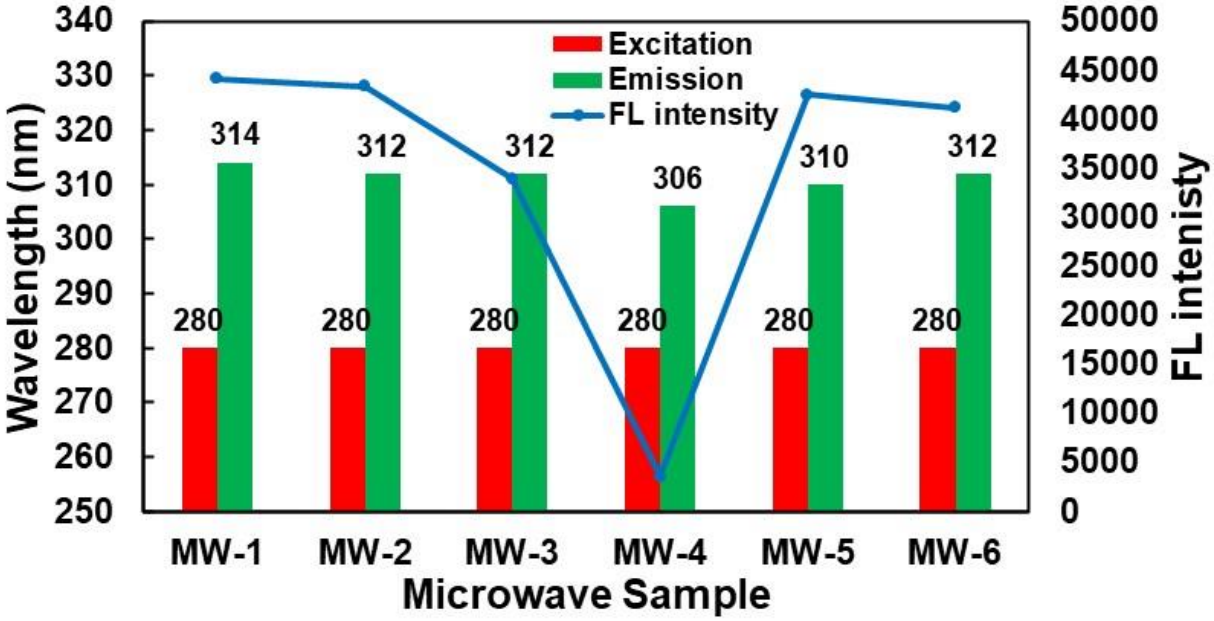

Figure 29: Excitation-dependent emission characteristics and FL intensity of samples obtained from the microwave experiments. Each bar represents a given sample. The red bars indicate the excitation wavelength corresponding to the maximum emission (depicted by green bars). Additionally, the blue line provides an overview of the maximum FL intensity observed.

3.1.2 UV-Vis Spectroscopy

The UV-vis spectra are illustrated in Figure 30. Except for MW-4, it turned out that all samples were too dilute to be measured precisely. The maximum absorption of MW-4 was observed at 332 nm.

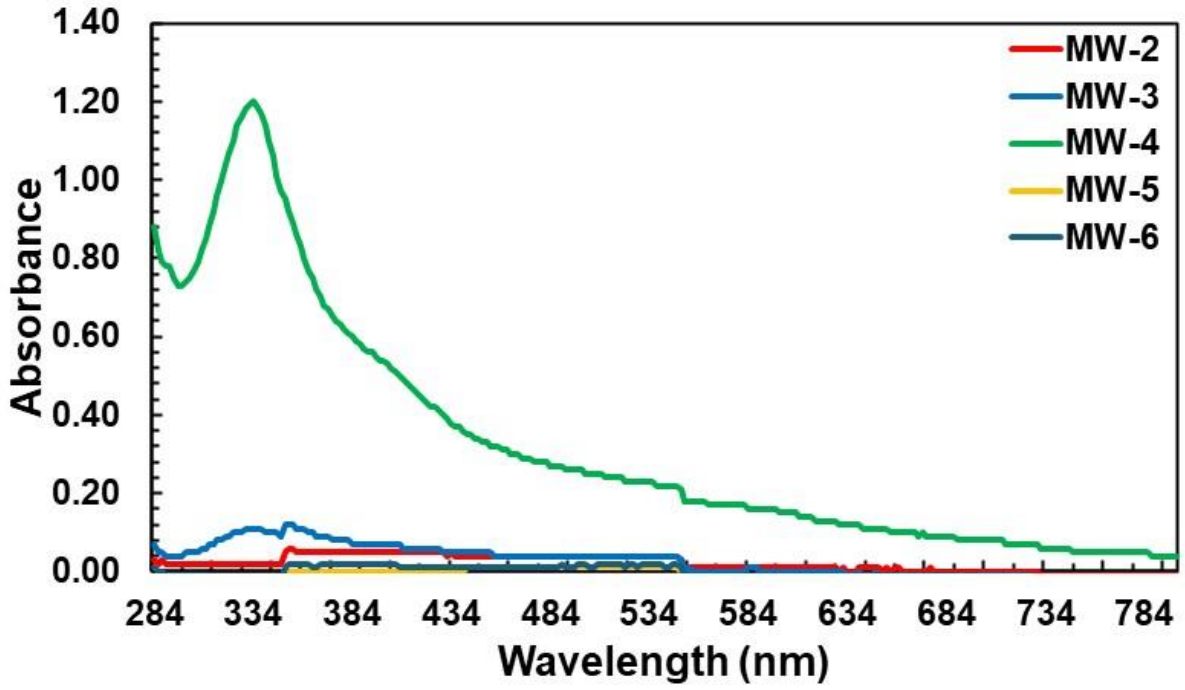

Figure 30: The UV-vis absorbance spectra of the products using the microwave method. Each spectrum was recorded over a wavelength range of 250 nm to 800 nm. Data below 284 nm was removed due to the cuvettes being made of plastic, which absorbs UV light.

3.1.3 FT-IR Spectroscopy

The FT-IR samples were too dilute to yield reliable measurements. Efforts were made to evaporate the samples to increase the concentration, but these attempts proved unsuccessful. The %reflectance ranged between 97-99%, with readings close to the baseline, suggesting that the resulting spectra may be predominantly influenced by noise. All spectra are included in Appendix I, with the spectrum of MW-4 presented in Figure 31 as an example.

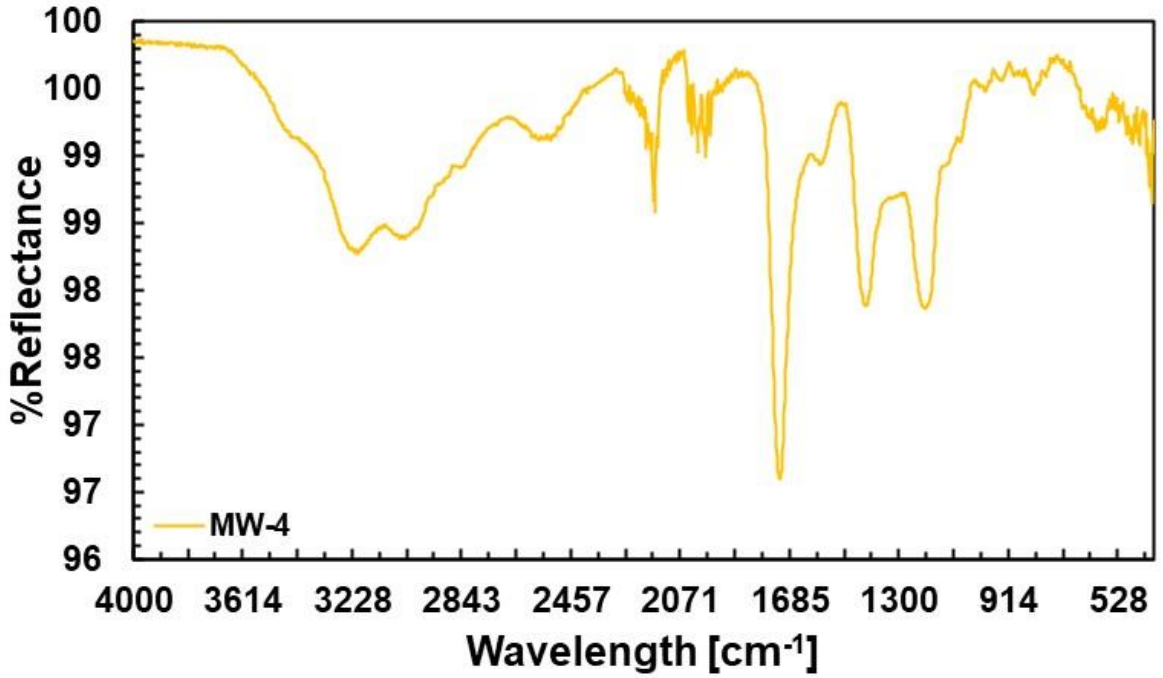

Figure 31: FT-IR spectrum of MW-4 syntheisized in a microwave, with a CA to urea ratio of 1:1.

3.2 Synthesis of CDs Using a Furnace

The experiments using a furnace were in addition to the microwave experiments serving as an alternative method for comparing results with the continuous flow setup. Table 6 details the experiments including the color and state of the product exiting the furnace. The aqueous product solution emitted blue fluorescence (Figure 32) under UV light (366 nm) while appearing as orange, brown or black solutions in daylight. The color of the product solution progressively darkened to black with a purple hue as the CA-to-urea ratio approached 1:1 (Figure 32).

Table 6: The experimental parameters and conditions for the experiments using a furnace, detailing the time, molar ratio and resulting color and state of the product. The temperature was set to 200 °C and the reaction time was 2 hours.

Name	Molar Ratio CA : urea	Color, state
F-1	-	orange, caramel-looking solid
F-2	1 : 0.2	brown, caramel-looking solid
F-3	-	orange, caramel-looking solid
F-4	1 : 0.2	brown, caramel-looking solid
F-5	-	orange caramel-looking solid
F-6	1 : 0.3	brown caramel-looking solid
F-7	1 : 0.5	porous, black, charred solid
F-8	1 : 0.9	porous, black with hints of purple, solid

All solutions were prepared in a crucible following the procedures outlined in the experimental section 2.3.1. F-1 and F-2 proved unsuccessful and were abandoned. F-4 and F-4 were replicates of the initial experiments.

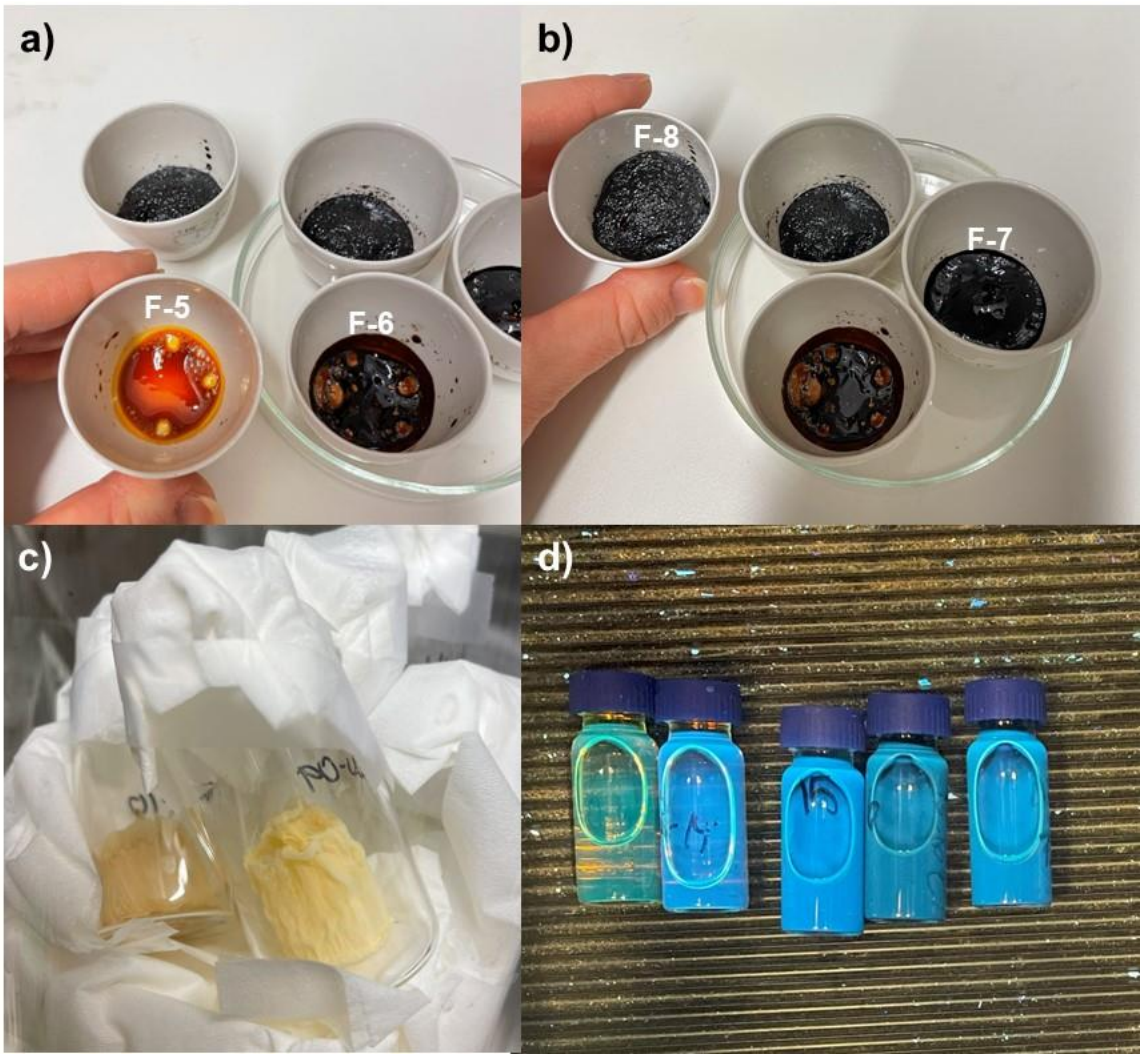

Figure 32: Products from experiments using a furnace**.** a) and b) Photos of the products post-reaction completion. F-5 contains only CA and appears as an orange, caramel-like solid. As the CA to urea ratio increased to 1:1, the color darkened to a black, charred solid. c) Photo of product after dialysis and freeze-drying. d) Photo after resuspending the product in deionized water before dialysis.

In experiments F-5 to F-8 the CA to urea ratio is increased. As the ratio approached 1:1, the resulting product exhibited a heightened level of charring, appearing darker and more porous.

3.2.1 FL Spectroscopy

Compared to the MW samples, the furnace samples did not exhibit a predominant maximum excitation wavelength. Figure 33a illustrates this with sample F-4, where the maximum excitation wavelength is 440 nm, only slightly more intense than the other excitation wavelengths. The excitation wavelength of 360 nm produced the maximum emission only for F-6 and F-7. For the remaining samples, it resulted in the second highest emission intensity. Therefore, to present a comprehensive figure including all samples, this wavelength was chosen for Figure 33b. As shown

in Figure 33a, there was minimal variation in emissions across different excitation wavelengths, a trend consistent with the other furnace-produced samples.

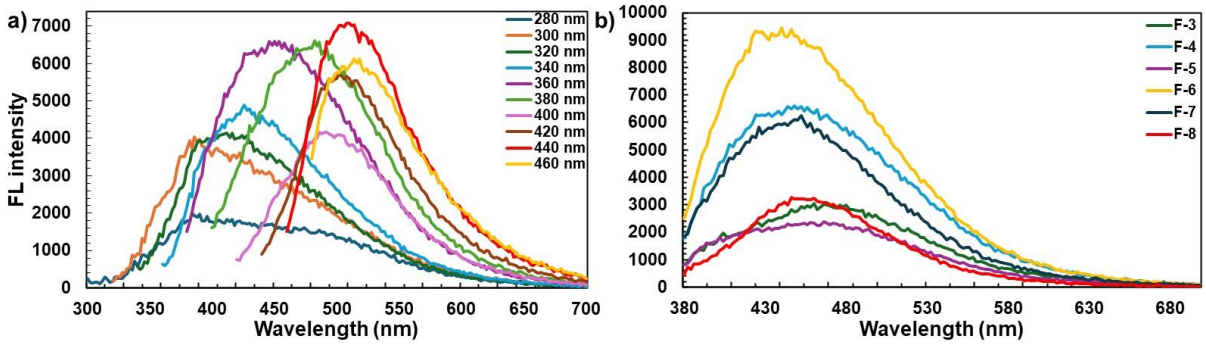

Figure 33: FL emission spectra for the experiments using a furnace. a) Emission spectra for experiment F-4 depicting varying excitation wavelengths. b) Emission FL spectra for the furnace experiments were recorded at an excitation wavelength of 360 nm.

The bar diagram showcases the excitation-dependent emission characteristics of samples synthesized utilizing a furnace. Each bar within the graph represents a different sample and indicates the excitation wavelength at which maximum emission occurs. The blue line shows the respective FL intensity of each sample, offering an insight into the relative maximum FL intensities.

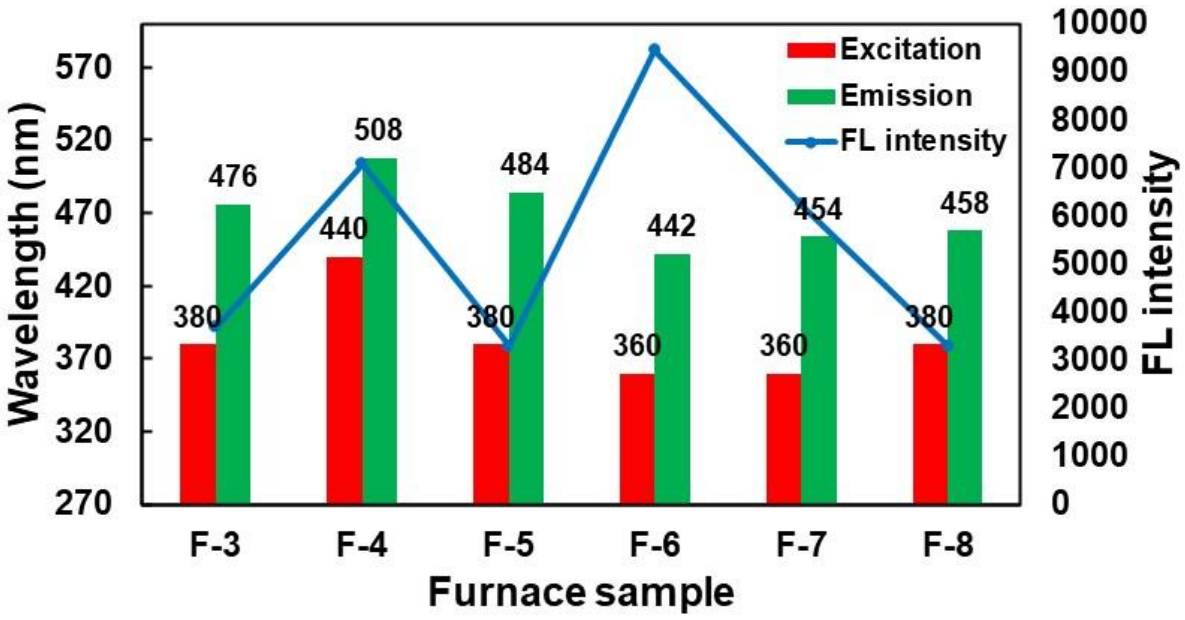

Figure 34: Excitation-dependent emission characteristics and FL intensity of samples from furnace experiments. Each bar represents a distinct sample. The red bars indicate the excitation wavelength corresponding to the maximum emission (depicted by green bars). Additionally, the blue line represents the maximum FL intensity observed for each sample.

Figure 35 illustrates the emission spectra for all samples using the respective maximum excitation wavelengths.

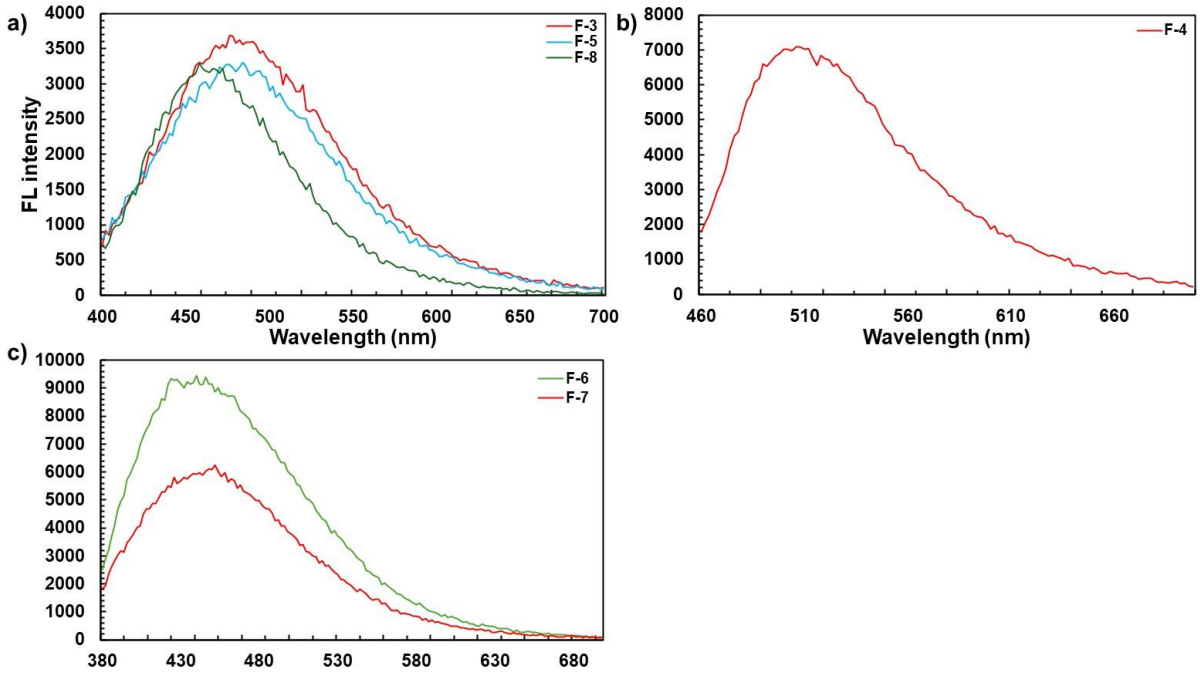

Figure 35: Fluorescence spectra from the furnace at various excitation wavelengths corresponding to the maximum emission are as follows: a) F-3, F-5, and F-8 display maximum emission when excited at 380 nm. b) F-4 shows peak emission with an excitation wavelength of 440 nm. c) F-6 and F-7 have the maximum emission with an excitation wavelength of 360 nm.

3.2.2 UV-Vis Spectroscopy

The UV-vis spectra are displayed in Figure 36.

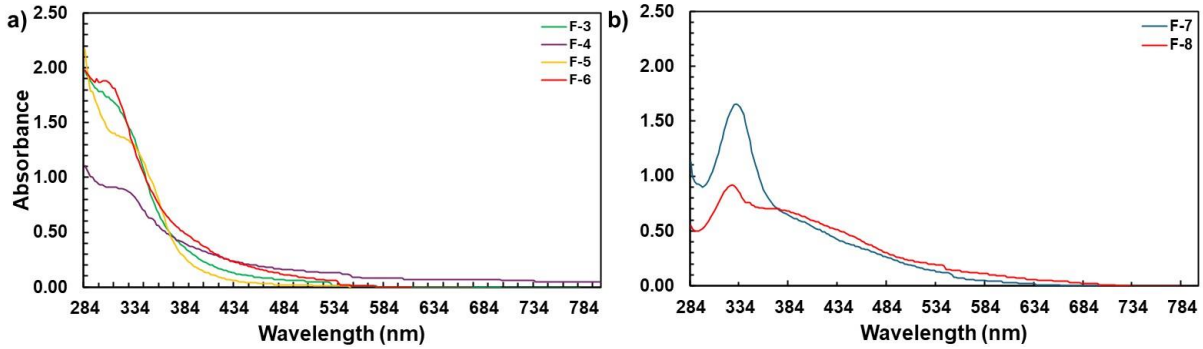

Figure 36: The UV-vis spectroscopy analysis of the product synthesized with a furnace. a) UV-vis spectra for F-3 to F-6 do not show a distinct absorption band. b) UV-vis spectra for F-7 and F-8 exhibit a distinct absorption band at 332 nm.

3.2.3 FT-IR Spectroscopy

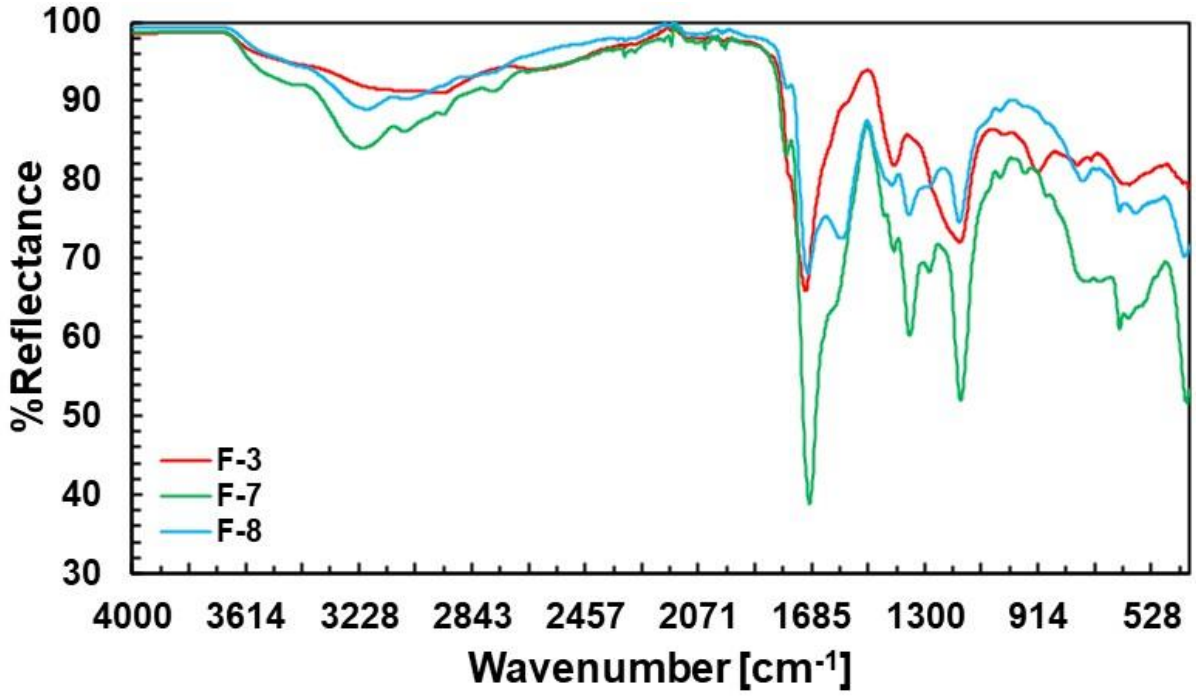

Figure 37: FT-IR spectra of product from the furnace experiments. The FT-IR spectra show a selection of products, arranged according to an increasing ratio of CA to urea. F-3 consists only of CA, F-7 has a CA to urea ratio of 1:0.5, and F-9 has a ratio of 1:0.7.

3.3 Continuous Flow

The continuous flow experiments comprised three distinct stages: preliminary experiments, the main experimental phase exploring various reactant concentrations and molar ratios, and cascade experiments initiated to address pressure challenges arising from gas generation in the reactor. These cascade experiments were aimed at resolving the pressure-related issues.

3.3.1 Preliminary Experiments

The purpose of the initial experiments was to explore the possibility and results of producing CDs through the continuous flow setup, while also integrating the autosampler functionality of the Vapourtec system. These samples were only used to test the system and were not dialyzed, freeze-dried, or analyzed. Only the color and the behavior under UV light were observed.

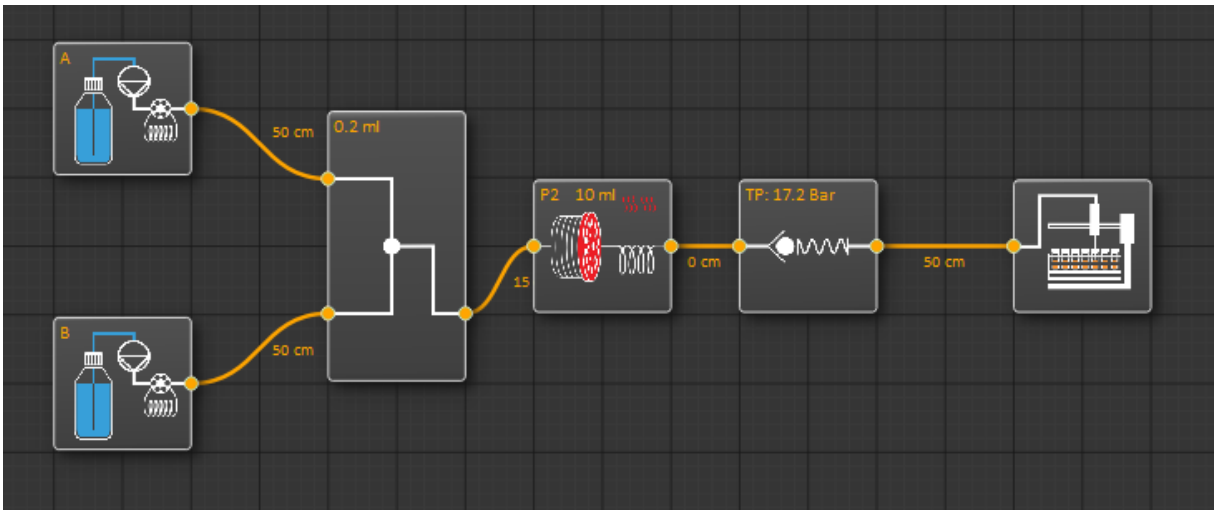

Figure 38: Flow scheme from the R-series software: depicting by two pump icons, one for each reactant, followed by a micromixer, the high-temperature coil reactor, and the BPR. The scheme also concludes the "autosampler injector and collection" icon.

The reactants (2 mL) were individually injected into the flow stream from a sample loop, passed through the reactor, and then collected. Each experiment was accompanied by a concentration model calculation, considering the flow rate and capillary lengths (refer to Figure 39). Theoretically, the collection time spanned from the initial rise in product concentration, through the steady state, until only solvent remained ("collect all" function).

However, the decomposition of reactants created gaseous compounds, leading to pressure irregularities and issues that affected the calculated collection time. To ensure total product collection, the collection time was adjusted by extending the ending time, as shown in the "collection" function on the right in Figure 39.

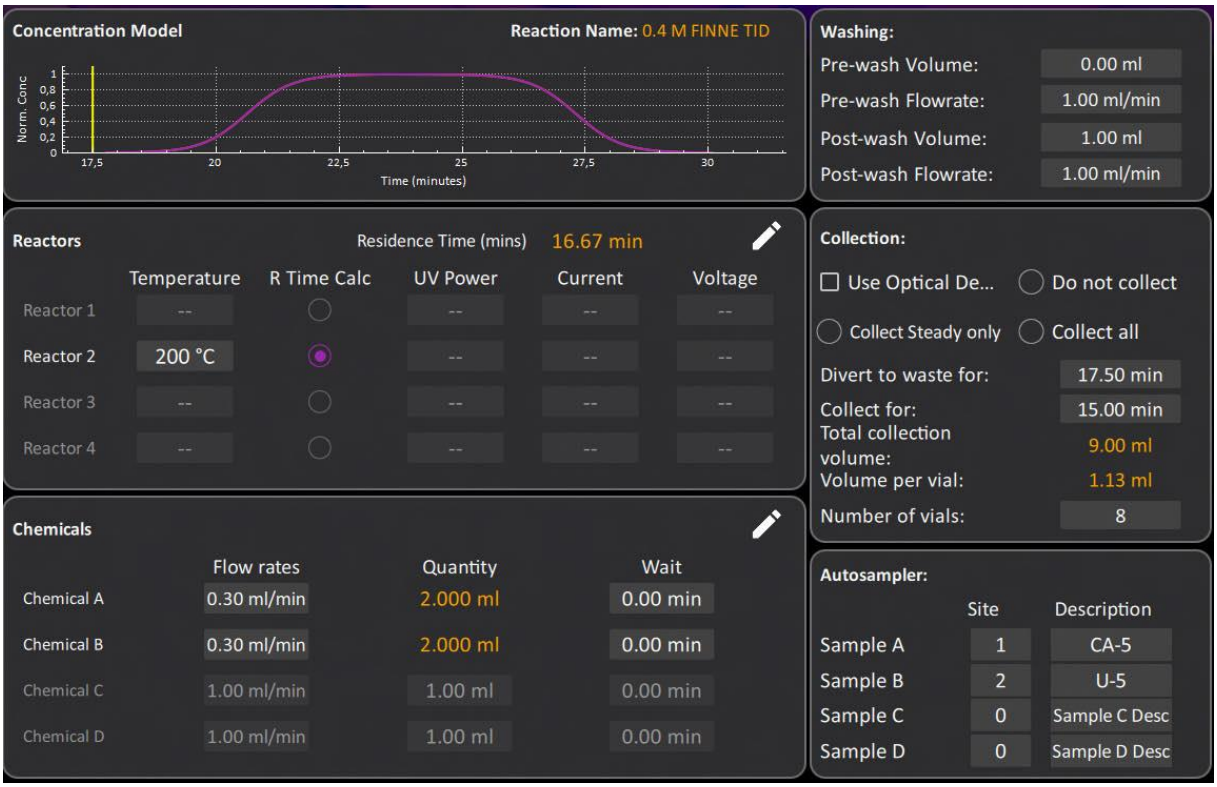

Figure 39: Configuration for the Vapourtec software included concentration model calculations (upper left corner) where the purple graph represents the steady state, indicating a theoretically constant product concentration. Additional settings include washing, collection options, reactor position and temperature, injection volumes for chemicals, and sample positioning for the autosampler.

Table 7: The experimental parameters and conditions for the preliminary experiments conducted. The provided flow rate (F_R) represents the combined flow rate of both pumps utilized in the setup. τ denotes the residence time in the high-temperature coil reactor set at 200 °C. The results are represented based on the color observed upon exiting the reactor, as well as whether the product solution exhibited fluorescence at 366 nm.

Name	τ [min]	F_R [mL/min]	Molar Ratio CA : urea	Color
P-1	10	1.0	1 : 0.1	no visible FL
P-2	10	1.0	1 : 0.3	no visible FL
P-3	10	1.0	1 : 0.7	FL
P-4	10	1.0	1 : 1.0	FL
P-5	10	1.0	1 : 1.5	colorless, FL
P-6	10	1.0	1 : 1.2	pale yellow, FL
P-7	10	1.0	1 : 1.0	pale yellow, FL
P-8	10	1.0	1 : 1.2	pale yellow, FL
P-9	10	1.0	1 : 1.0	pale yellow, FL
P-10	33	0.3	1 : 1.0	yellow, FL
P-11	33	0.3	1 : 1.2	pale yellow, FL
P-12	17	0.6	1 : 1.5	pale purple, FL
P-13	17	0.6	1 : 1.0	pale purple, FL
P-14	17	0.6	1 : 1.0	pale brown, FL
P-15	17	0.6	1 : 1.0	brown, FL
P-16	17	0.6	1 : 1.0	yellow, PL

P-5 to P-9 in Table 7 were dedicated to investigating different concentrations of CA and urea, aiming for a roughly 1:1 ratio. The concentrations of CA varied from 0.06 M to 0.41 M, while those of urea ranged from 0.08 M to 0.42 M. Notably, this series of experiments marked the initial occurrence of gas evolution within the reactor, as depicted in Figure 40c.

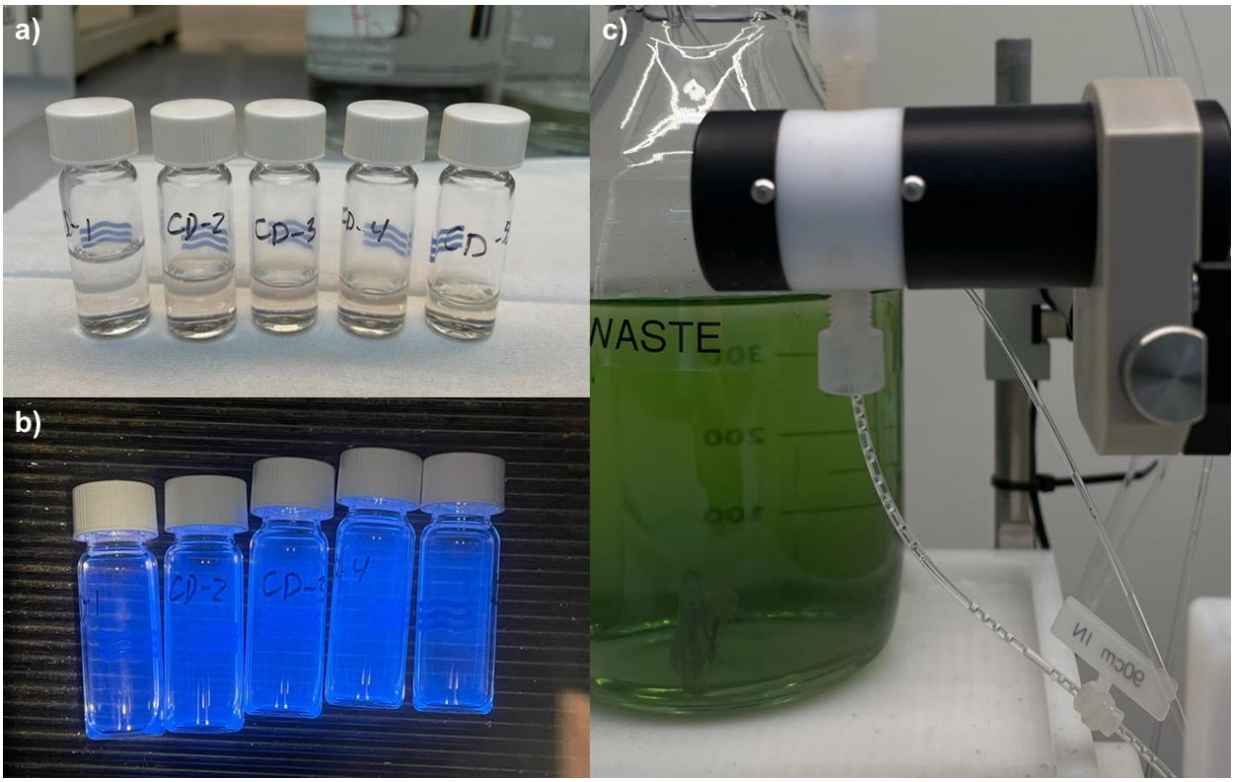

Figure 40: a) Photo of volume reduction with rising concentrations of CA and urea from left to right. b) Corresponding samples to those in a), displaying FL under a UV lamp at an excitation wavelength of 366 nm. c) Gas bubbles after the BPR indicate an irregular flow and the formation of bubbles in the reactor, resulting in a gas-liquid segmented flow pattern.

P-10 details an experiment aimed at collection a substantial volume of product. As depicted in Figure 41, the collection process was segmented into three stages. The first stage included most of the steady-state phase, the second covered the period with the highest gas production, and the third stage involved a phase with minimal gas production and fading solution color.

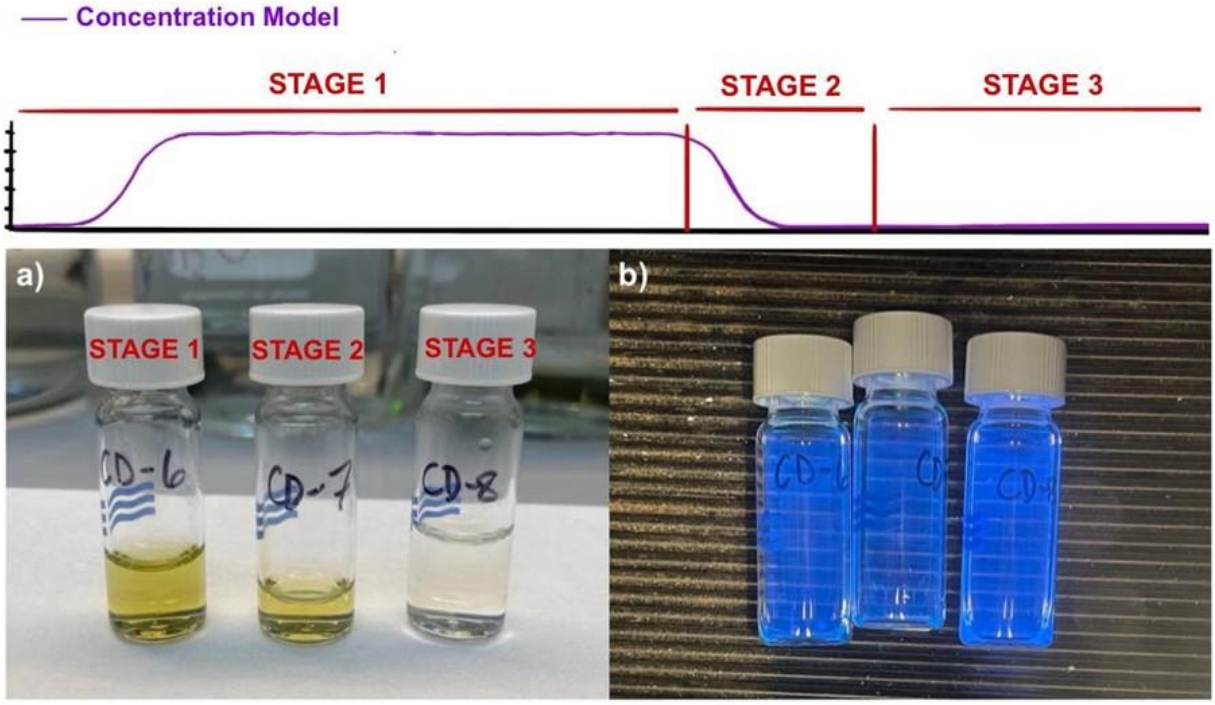

Figure 41: a) Samples collected at different stages, from left to right: the steady-state phase, the second stage with the highest gas production, and the third stage involving minimal gas production and fading solution color. An example of a concentration model is included to illustrate these stages. b) Despite the diminishing color of the third sample, the solution kept strong FL at 366 nm.

3.3.2 Synthesis of CDs Using a Continuous Flow Setup

Before starting the syntheses using the continuous flow setup, the issue of gas formation during the reaction was considered. Consequently, it was decided not to employ the autosampler in the subsequent experiments and the collection time was adjusted to ensure complete product collection. The solutions were prepared following the procedures outlined in the experimental section 2.4.2. Table 8 provides details of the experiments, including the resulting color of the product. Experiments CF-3 to CF-6 were divided into two collection phases. The output from the initial 100 minutes was collected in a large vial, while the output from the final 30 minutes was collected in a smaller vial. Samples from both collection phases underwent analysis using the same characterization technique. The samples collected at the end of the process are referred to as "CF-X*" in subsequent analyses.

Entries labeled "CF-Xa" in Table 8 indicate the cascade experiments where the reactants (CA and urea) went through one cycle in the reactor. The resulting product was collected and reused as reactants for the second cascade reaction, denoted "CF-Xb".

Table 8: The experimental parameters and conditions for the experiments using the continuous flow setup, detailing the residence time, molar ratio and resulting color of the CD product. The temperature was set to 200 °C.

Name	τ [min]	F_R [mL/min]	Molar Ratio CA : urea	Color
CF-1	60	0.17	-	black with hints purple
CF-2	120	0.08	-	black with hints of purple
CF-3	60	0.17	1 : 0.1	black
CF-4	60	0.17	1 : 0.3	black with hints of yellow
CF-5	60	0.17	1 : 0.7	black with hints of purple
CF-6	60	0.17	1 : 1.0	black with hints of purple
CF-7	60	0.17	1 : 1.0	black with hints of purple
CF-8a	5	2.00	1 : 1.0	light yellow
CF-8b	5	2.00	-	yellow with hints of red
CF-9a	15	0.67	1 : 1.0	dark yellow
CF-9b	15	0.67	-	brown with hints of orange
CF-10a	30	0.33	1 : 1.0	black with hints of yellow and green
CF-10b	30	0.33	-	brown with hints of black
CF-11a	60	0.17	1 : 1.0	black with hints of yellow and green
CF-11b	60	0.17	-	black

CF-1 and CF-2 were conducted to examine any differences between 60- and 120-min residence time in the reactor. CF-3 to CF-7 was done to examine the potential differences between various ratios of CA and urea. However, there was no visible difference to be noticed, and all samples turned out to be black with hints of yellow.

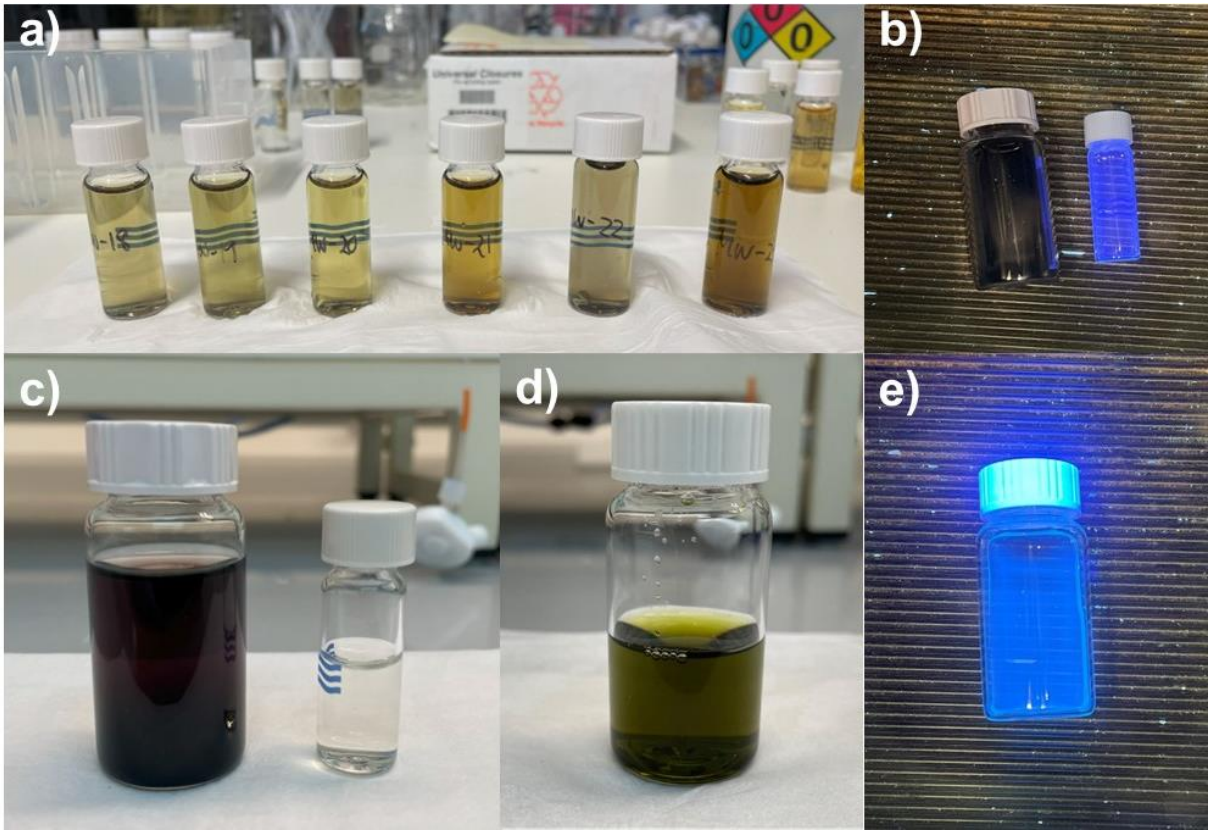

Figure 42: Photos of the product solutions achieved through the continuous flow system, along with the corresponding color. a) Photos from the experiments CF-1 to CF-6, arranged from left to right. b) Photo of CF-3 post-collection under UV light (366 nm). c) Photo of CF-3, showcasing a large vial containing the sample collection from the initial phase to 100 minutes, and a smaller container holding the collection from 100 to 130 minutes (CF-3*). d) Photo of CF-10a after the collection phase. e) Photo of CF-8a under UV light with a wavelength of 366 nm.

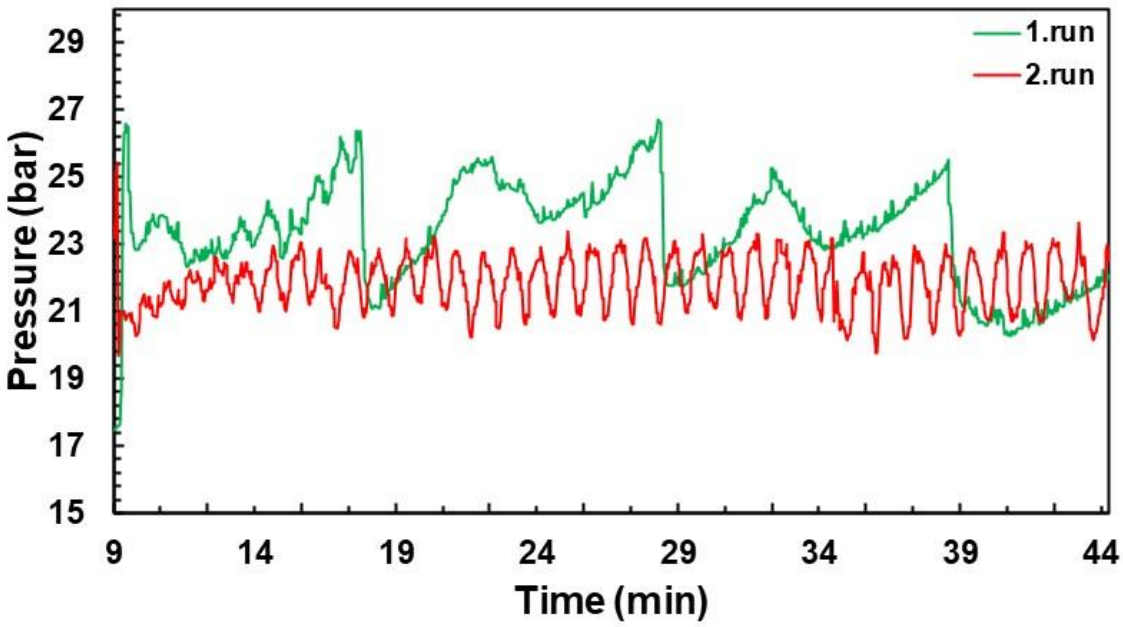

Figure 43: A segment of the pressure fluctuations generated by the R-series software during the cascade experiments**.** The pressure observed during both the first and second runs. The total pressure graph is depicted in Appendix E.

3.3.3 FL Spectroscopy

The excitation wavelength corresponding to the maximum emission for the CF-samples was either 280 nm or 360 nm. All samples are depicted at their respective maximum excitation wavelengths in Figure 44. CF-5, CF-6, and CF-7, including CF-5* and CF-6*, exhibited strong FL. Conversely, CF-1 to CF-4, along with the corresponding samples collected during the last 30 minutes, displayed weaker FL compared to the former samples. The cascade experiment samples were not freeze-dried before the FL measurements and were directly measured using the dialyzed samples.

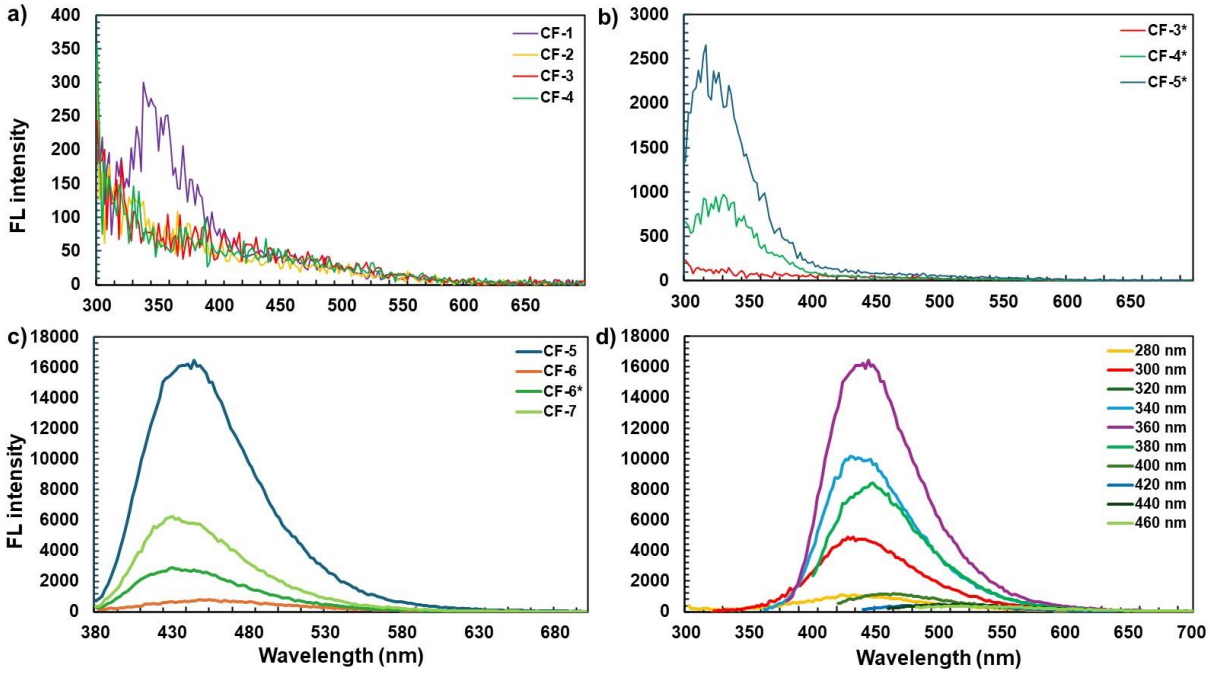

Figure 44: FL emission spectra for the product solutions synthesized with the continuous flow setup. a) FL emission spectra for the samples exhibiting low intensity at maximum emission, excited at a wavelength of 280 nm. b) FL emission spectra for samples collected during the last 30 minutes, displaying more intense emission than a), excited at a wavelength of 280 nm. c) FL emission spectra for the samples with maximum emission observed at an excitation wavelength of 360 nm. d) Emission spectra illustration for experiment CF-5 depicting varying excitation wavelengths.

Figure 45 illustrates the excitation-dependent emission characteristics of all samples synthesized using the CF setup. Each bar in the graph represents a different sample, indicating the excitation wavelength at maximum emission, while the blue line represents the corresponding FL intensity. Specifically, in Figure 45a, CF-1 to CF-7, including the CF-X* samples, are presented. Figure 45b demonstrates the cascade experiments, revealing a decrease in FL intensity as residence time increases.

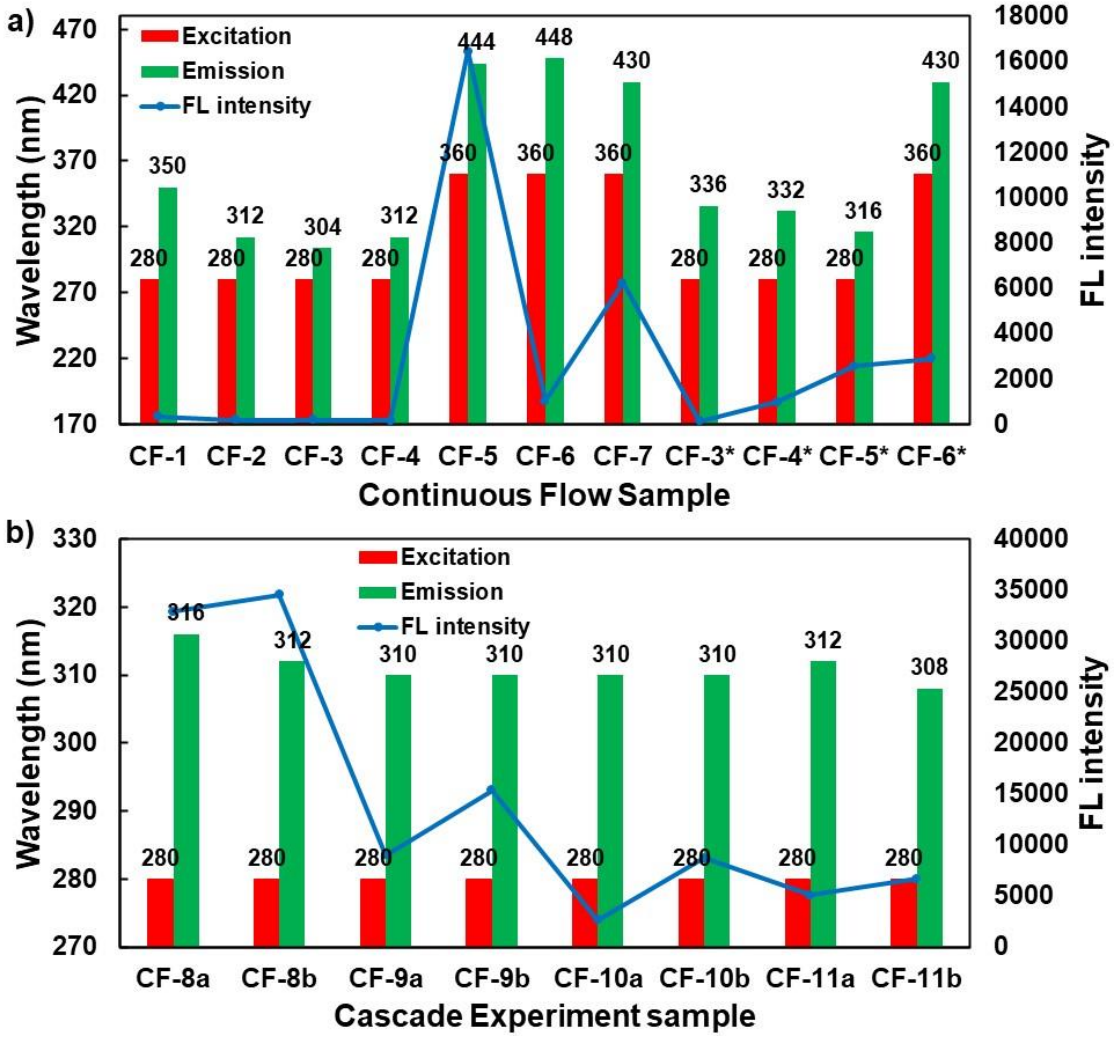

Figure 45: Excitation-dependent emission characteristics and FL intensity of product samples are depicted for: a) CF-1 to CF-7, including the corresponding CF-X* samples, and b) cascade experiments, CF-8a to CF-11b. Each bar in the graph represents a distinct sample. The red bars indicate the excitation wavelength corresponding to the maximum emission (depicted by green bars). Additionally, the blue line provides an insight of the maximum FL intensity observed for each sample.

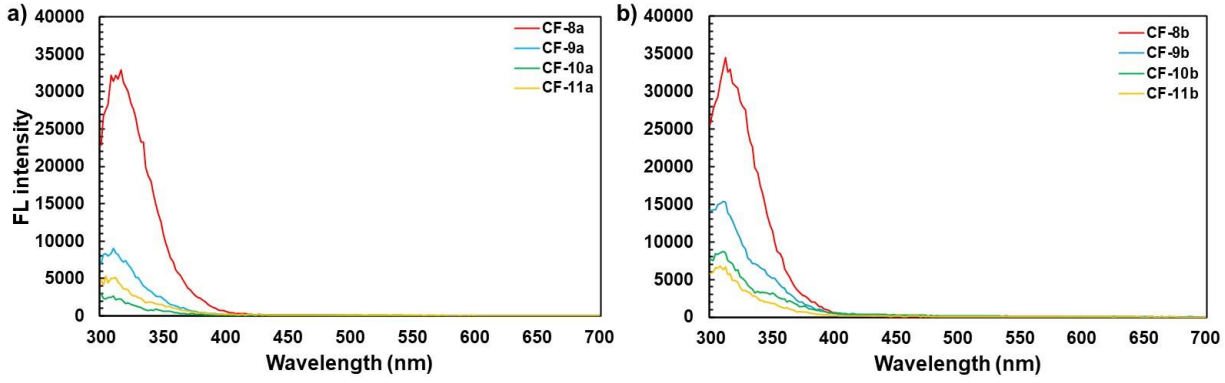

Figure 46: FL emission spectra of the cascade experiments observed at an excitation wavelength of 280 nm. a) FL emission spectra obtained for samples collected during the first run. b) FL emission spectra obtained for samples collected during the second run. The FL intensity decreases as the residence time increases.

3.3.4 UV-Vis Spectroscopy

The UV-vis spectra for the product solutions using the CF setup are depicted in Figure 47. CF-5 was the only sample exhibiting a distinct absorption band at 332 nm.

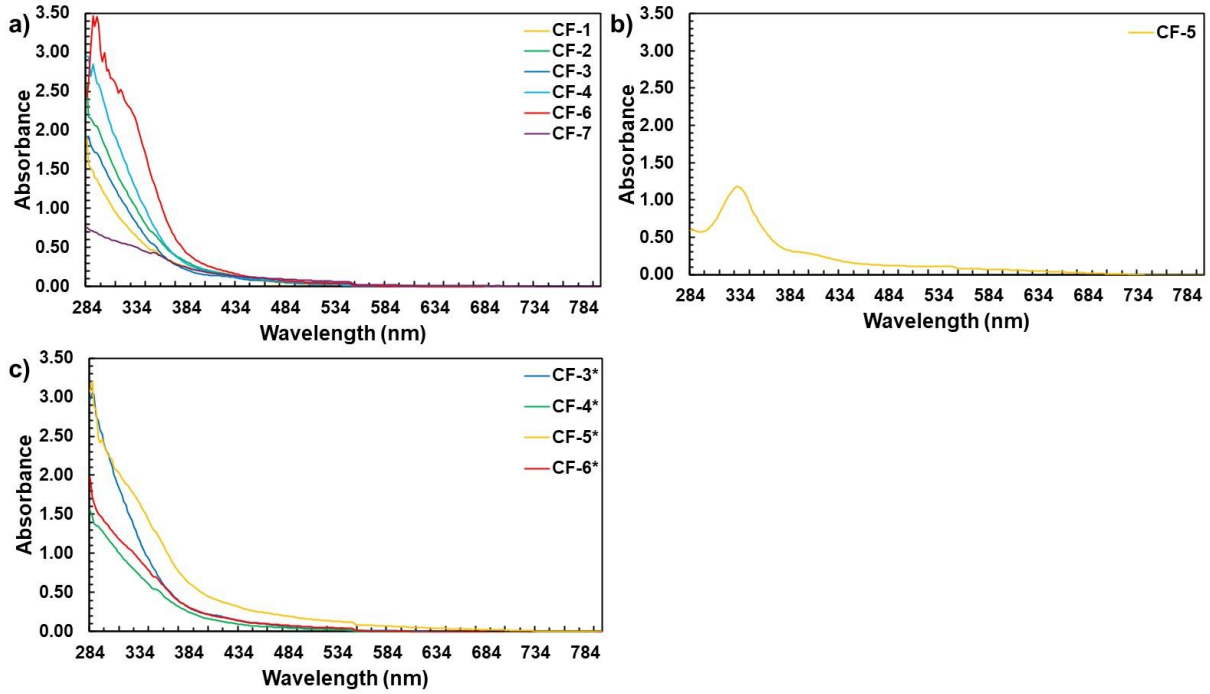

Figure 47: UV-vis spectra of the product synthesized using the continuous flow setup. a) UV-vis spectra recorded for CF-1 to CF-7, excluding CF-5. b) A separate UV-vis spectrum was acquired for CF-5 due to its distinct absorption band at 332 nm. c) UV-vis spectra obtained for samples collected during the last 30 minutes of each experiment.

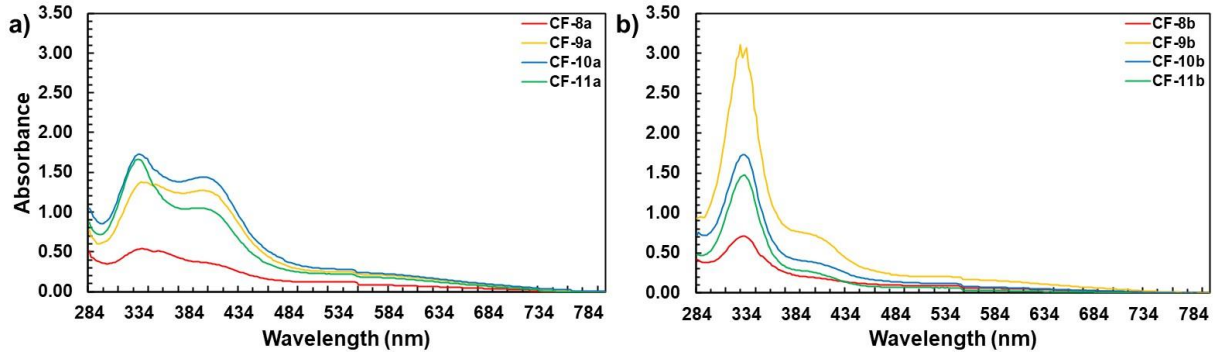

Figure 48: UV-vis spectra of the product solutions from the cascade experiments. a) UV-vis spectra obtained for samples collected during the first run. b) UV-vis spectra representing samples collected during the second run.

3.3.5 FT-IR Spectroscopy

The FT-IR samples of the samples collected after 130 minutes were too dilute to give reliable results and is therefore excluded. The spectra for the first collected samples are presented in Figure 49. All FT-IR spectra are given in Appendix I.

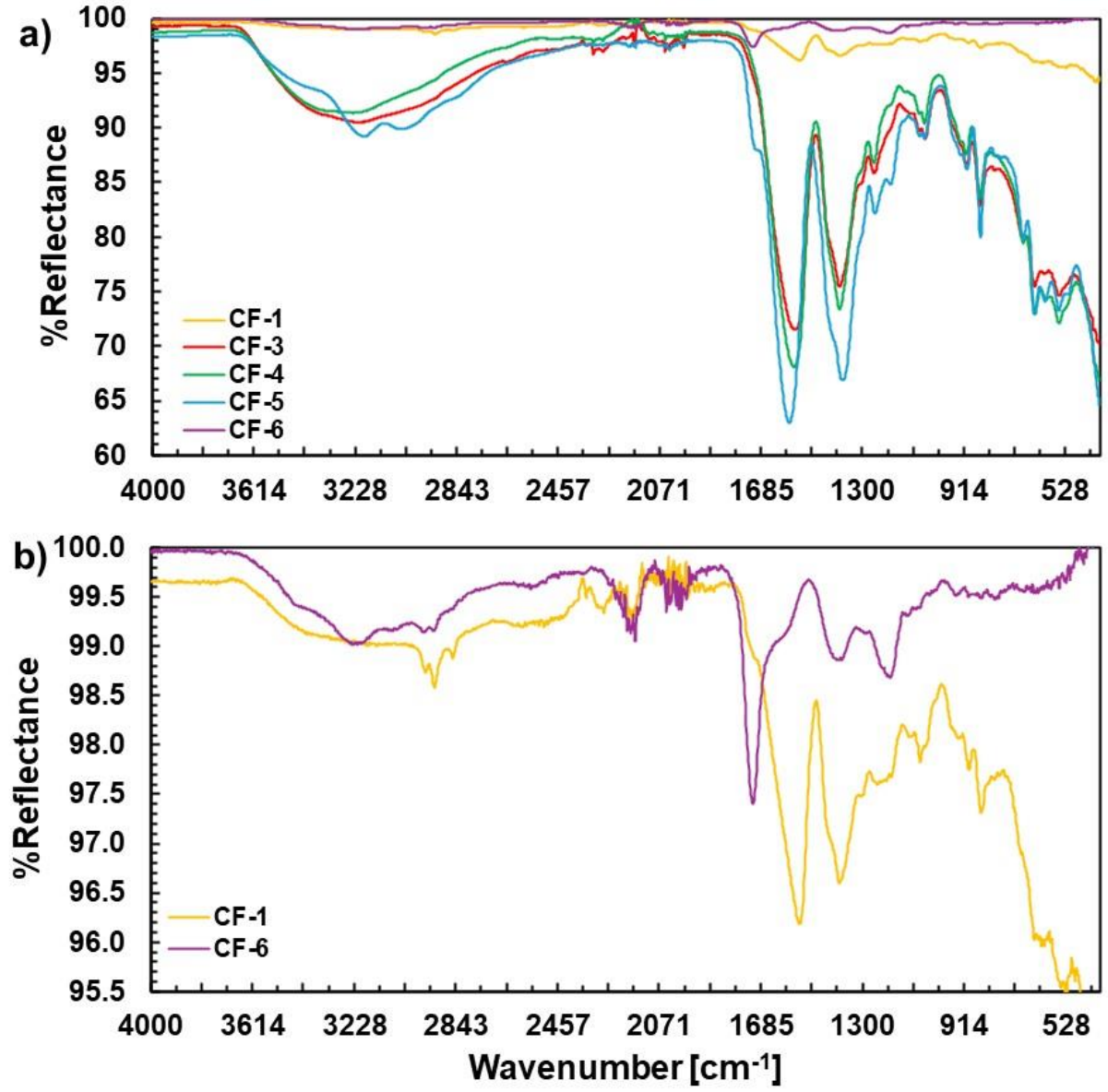

Figure 49: FT-IR spectra of product solutions using the continuous flow setup and a residence time of 60 minutes**.** a) FT-IR spectra are provided for CF-1 to CF-6, organized based on the increasing ratio of CA to urea. CF-2 is excluded due to its residence time of 120 minutes. Specifically, CF-1 consists only of CA, CF-3 has a ratio of CA to urea of 1:0.1, CF-4 has 1:0.3, CF-5 has 1:0.7, and CF-6 has 1:1. b) The FT-IR spectrum for sample CF-1 and CF-6 are zoomed in due to its low intensity, enhancing clarity and visibility of the spectrum.

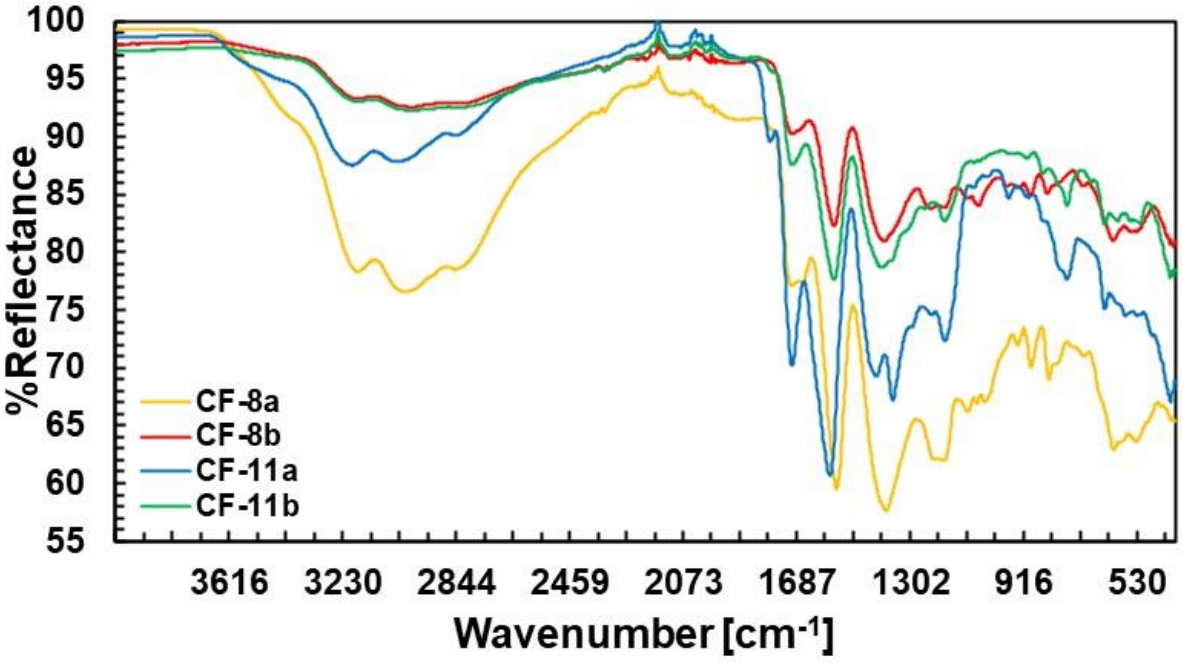

Figure 50: FT-IR spectra for a subset of the cascade experiments, including CF-8a/b and CF-11a/b, serving as endpoints to show the difference between the initial and the subsequent run within these experiments.

3.3.6 TEM Imaging

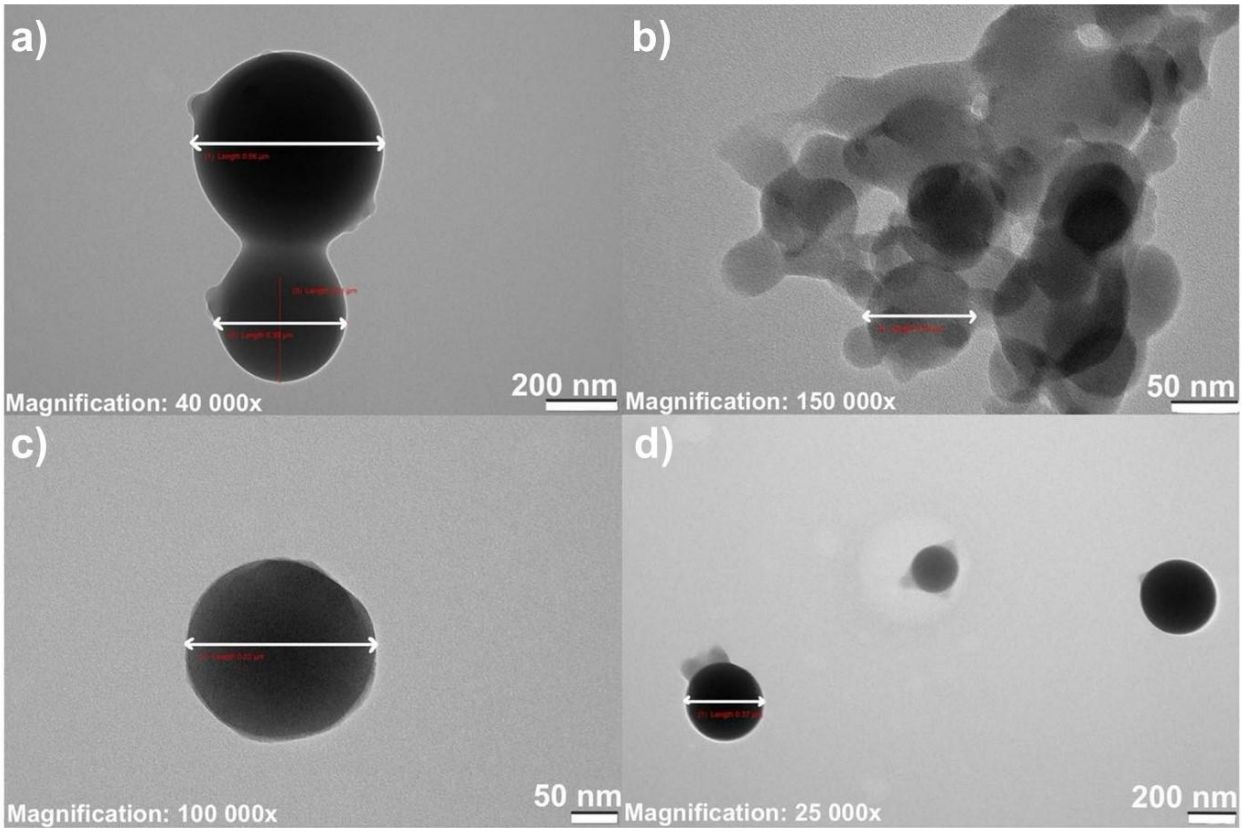

Figure 51: TEM images of different product samples at varying magnifications and an acceleration voltage of 160 eV. The measured diameters for the particles present in the samples are as follows: a) CF-8b: 560 nm and 390 nm. b) CF-10b: 80 nm. c) CF-8a: 220 nm. d) Another sample of CF-8b: 370 nm.

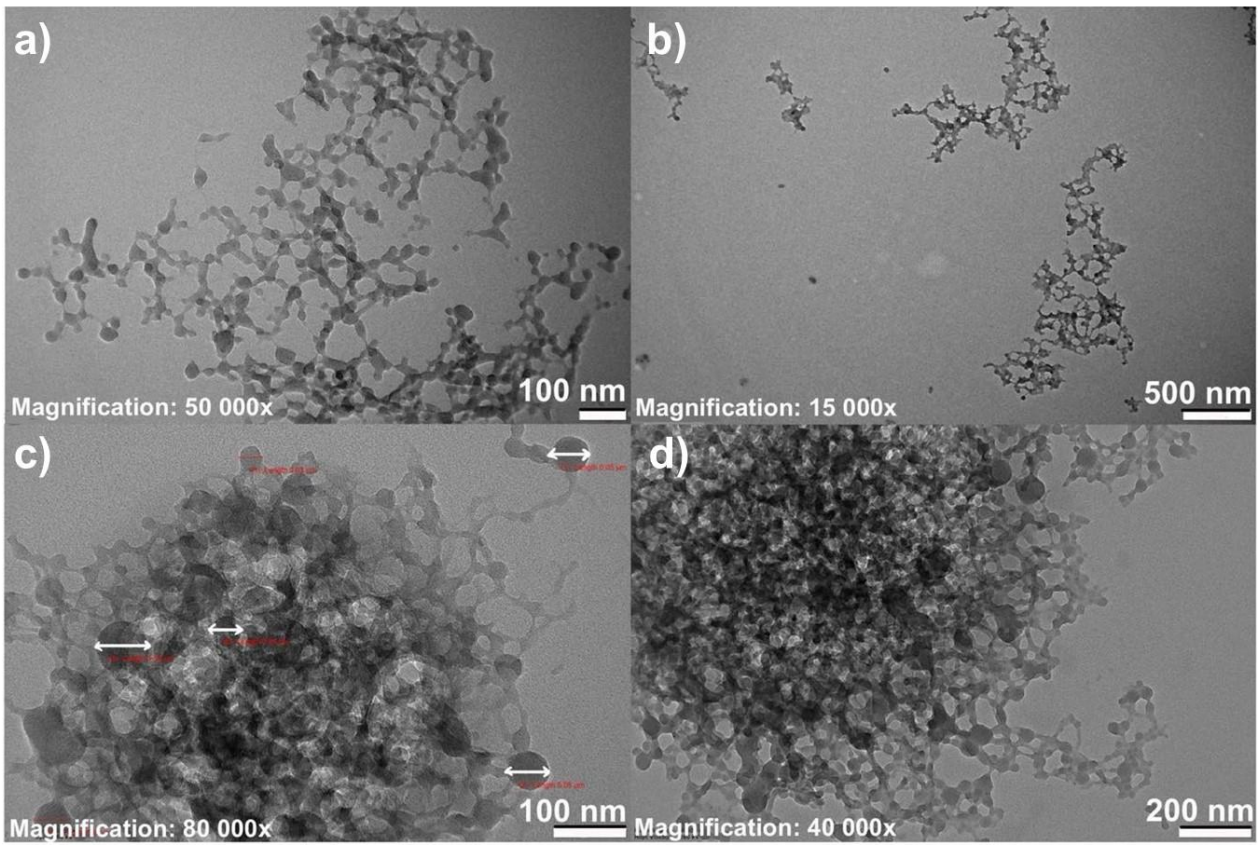

Figure 52: TEM images of different product solutions captured at varying magnifications and an acceleration voltage of 160 eV. a) Image of CF-9b. b) Image of CF-11a. c) Image of CF-11b. The measured diameters of the particles in the sample are 80nm, 50 nm, 60 nm, 50nm from left to right. d) Another view of CF-11a.

3.4 Characterizing through Raman Spectroscopy

Raman spectroscopy was employed to analyze the product, both in solution (dissolved in either 2-propanol or water) and in the solid, freeze-dried form. A non-contact sampler probe, an immersion probe, was utilized for the solutions, while a ball probe was employed for solid samples. In Figure 53, one sample from each synthesis method (microwave, furnace, and continuous flow) is given, demonstrating similar results across all methods.

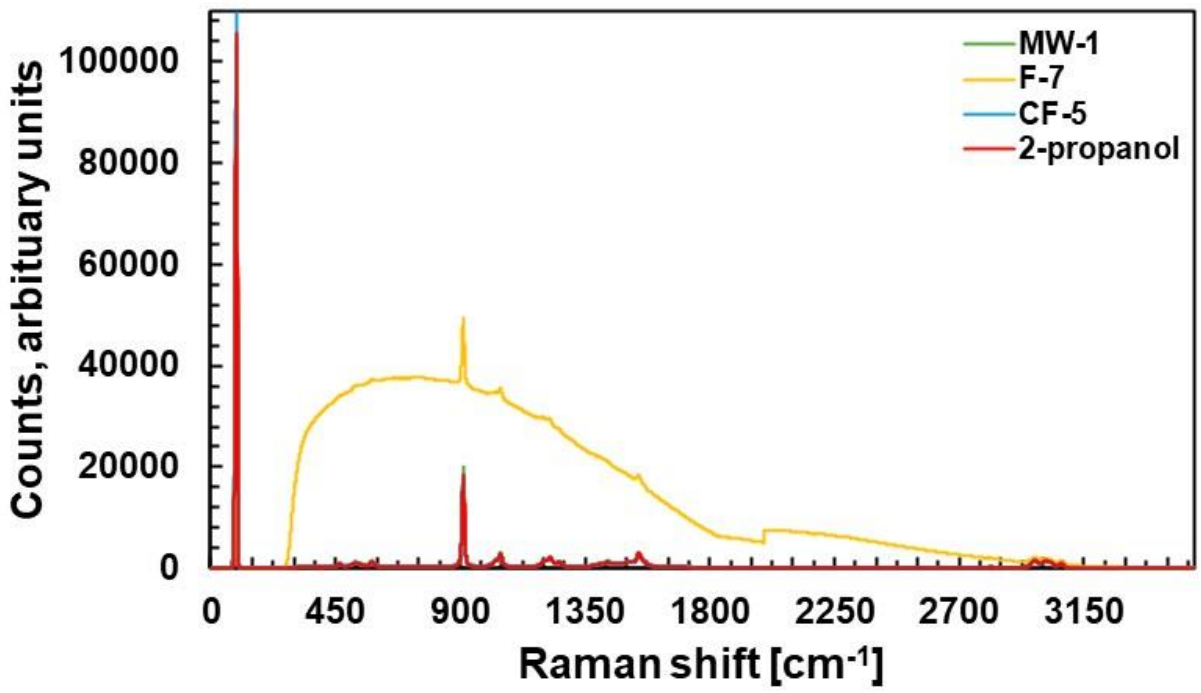

Figure 53: The Raman spectra of CDs synthesized using various methods: microwave (MW-1), furnace (F-7), and continuous flow (CF-5). The solvent was 2-propanol. Despite efforts to analyze both solution and solid samples, fluorescence interference rendered the results inconclusive.

3.5 Characterizing through DLS

Figure 54 displays size distributions of CD samples, with reported sizes representing the mean of triplicate measurements. Three samples from each synthesis method are provided to illustrate size distribution examples, alongside the cascade experiments. However, as discussed in more detail in Chapter 4.7 "Particle Size Analysis through DLS", the DLS measurements proved inconclusive due to the solutions being unsuitable for such measurements. This was attributed to factors such as samples exhibiting FL and low intensity count rate.

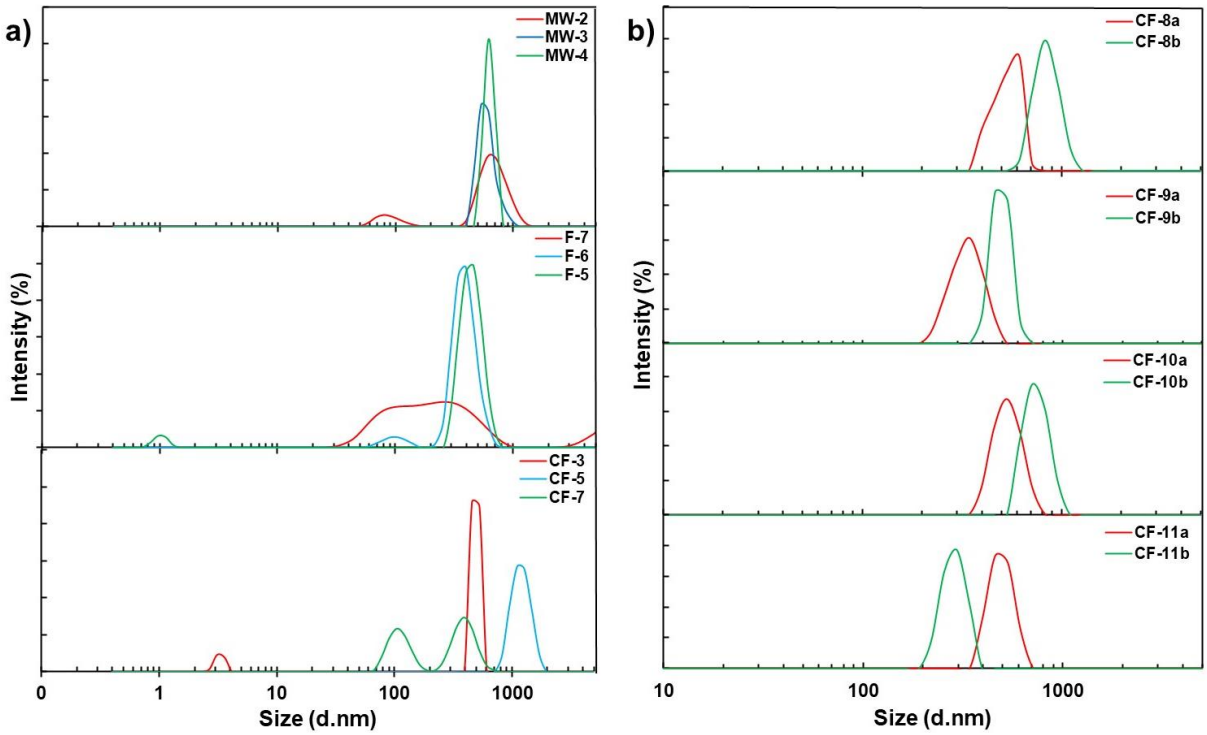

Figure 54: Size distributions for CDs synthesized using different methods: a) CDs synthesized using a microwave (upper), furnace (middle), and continuous flow setup (lower). b) CDs synthesized in the continuous flow cascade experiments. The red graph represents the first run, while the green graph represents the second run.

3.5.1 Evaluation the Accuracy of DLS Measurements

Figure 55 illustrates correlation coefficient graphs for three samples: polystyrene (considered as a "good" sample), CF-8b (classified as "medium good"), and CF-11a (depicted as having "bad correlation"). The correlation coefficient graphs are depicted in Appendix G.

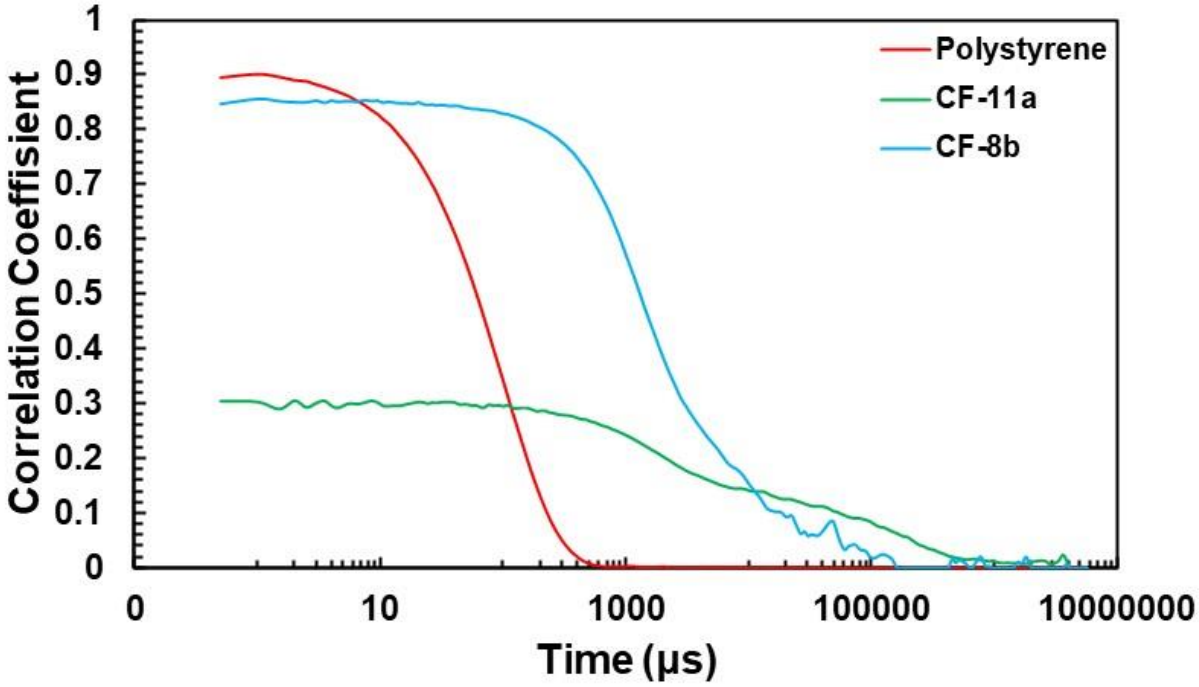

Figure 55: Correlation coefficient graphs for three samples: polystyrene ("good correlation"), CF-8b ("medium good correlation"), and CF-11a ("bad correlation").

Table 9: Presentation of calculated Z-average and PDI for polystyrene, CF-8b and CF-11a.

Sample	Z-Average (d.nm)	PDI
Polystyrene	63	0.048
CF-8b	1422	0.501
CF-11a	1844	0.897

4 Discussion

The aim of this work was to prepare CDs using a continuous flow setup and then compare this approach to traditional batch methods, specifically microwave and furnace techniques. In the experimental series, different ratios of CA and urea were tested, gradually increasing towards a 1:1 ratio, along with varying residence times.

4.1 Exploring Batch Methods: Transitioning from Microwave to Furnace Synthesis

At first microwave synthesis was selected for its widespread application in previous studies on CD synthesis (1-3). This method, known for its speed, cleanliness, and cost-effectiveness, facilitates rapid and uniform heating, leading to short reaction times and potentially higher yields and purities of CDs (1, 2, 24).

The closed system of the Biotage Initiator+ presented challenges, primarily due to the instruments pressure limits. Before initiating the reaction, the temperature was raised to 200°C, causing a significant pressure increase. Despite initial attempts at short five-minute experiments, the pressure exceeded the 20 bar limit before the reaction could begin. After two unsuccessful trials, it was decided to discontinue using the instrument.

The rapid increase in pressure was likely due to the decomposition of urea, which typically begins at around 140-180°C and produces gases such as NH_3 (79). Additionally, the decomposition of CA into gaseous compounds, including CO_2 (80), may have contributed to the pressure buildup.

It was decided to proceed with an alternative batch approach, employing furnace synthesis. The furnace trials were executed utilizing a Nabertherm L3/11 furnace. The trials were similar to the method used by Chen and colleagues (40), who synthesized N-doped CDs through a one-step sintering technique using ammonium citrate and CA as precursors. This method produced comparable results, with the CD product appearing as black, charred solids. Notably, the furnace operated as an open system, and pressure concerns was not an issue during experimentation.

While sintering is sometimes referred to as an independent synthesis method, it aligns with established bottom-up synthesis approaches for CDs, such as the hydrothermal method or pyrolysis (81-83). Notably, considering the melting point of citric acid at 153°C and urea at approximately 132°C, it appears that the technique of Chen et al. involves melting the precursors rather than strictly following traditional sintering methods. Therefore, in this context, the term "sintering" may not precisely describe the process. For ammonium citrate, with a melting point at

185°C, sintering may be more applicable. However, this is not the case for the precursors discussed in this study. Instead, the technique involves melting the precursors to synthesize CDs, falling within the broader category of bottom-up methods involving heating.

4.2 Exploring Continuous Flow for CD synthesis

Preliminary experiments were conducted to explore the possibility of producing CDs using a continuous flow system. The autosampler was utilized. This integration aimed to automate the synthesis process and gain proficiency in its usage. Given the limited utilization of the system by others, it presented an intriguing opportunity to get familiar with its operation.

The first set of experiments (P-1 to P-4 in Table 4 and 7) focused on various molar ratios of CA and urea. When the ratio approached 1:1, the FL was most pronounced under a UV lamp at 366 nm.

Subsequent experiments (P-5 to P-9 in Table 4 and 7) examined different concentrations of CA (0.06 M to 0.41 M) and urea (0.08 M to 0.42 M). These experiments marked the first instance of gas evolution in the reactor, initially suspected to be due to issues with the BPR. After replacing the BPR, pressure fluctuations persisted, causing inconsistent flow rates and an uneven flow profile.

Experiment P-10 aimed to collect a substantial volume of product solution, divided into three stages: steady-state, peak gas production, and minimal gas production with a fading solution color. Notably, even a colorless solution exhibited blue FL under UV light at 366 nm. The outcome of this was a reduction in sample volume as the concentration increased. Inaccuracies in the calculated collection time led to premature stopping, reducing sample volume.

Several experiments consistently highlighted gas production as a challenge during sample collection, prompting the investigation into its origin. After ruling out the BPR as the source of gas in the flow stream, it was suggested that the issue stemmed from within the reaction itself. This was attributed to the decomposition of CA and urea into gaseous compounds such as CO_2 and NH_3.

To effectively utilize the autosampler, it became important to ascertain the optimal collection duration beyond the determined "collect all" area to capture all product from the flow stream. P-12 to P-16 in Table 4 and 7 were dedicated for this purpose. Given the hypothesis that gas production correlated with concentration, the highest concentration (P-16, 0.40 M CA and 0.42 M urea) was selected to determine the maximum collection time. This duration was determined to be 35 minutes after the initiation of the reaction.

Due to extensive setup time and persistent gas evolution issues, the decision was made to discontinue the use of the autosampler for subsequent experiments. Instead, reactants were pre-mixed before initiating new CF experiments. Adjustments to collection times were incorporated in these experiments to ensure thorough product recovery.

The series of experiments (CF-2 to CF-6 in Table 3 and 8) involved splitting the collection process into two stages. This division arose from the observation that, even after gas evolution ceased and a steady flow was established, the solution often still exhibited blue FL under UV light at 366 nm. Therefore, the collection was divided to investigate potential differences between the CD solutions.

Experiment CF-7 involved collecting a crude sample from the final 30 minutes of the collection process. This sample was light yellow and displayed blue FL under UV light at 366 nm. This sample was analyzed similarly to the other dialyzed samples and compare the analyses.

CF-8a to CF-11b in Table 3 and 8 explored cascade reaction experiments with various residence times to potentially yield more distinct carbon cores. Moreover, researchers have synthesized CDs within short residence times, ranging from 5 to 20 minutes (27-29). Hence, it would be intriguing to investigate the differences between short and long residence times. A second run was conducted using the product from the first cascade reaction (illustrated in Figure 56).

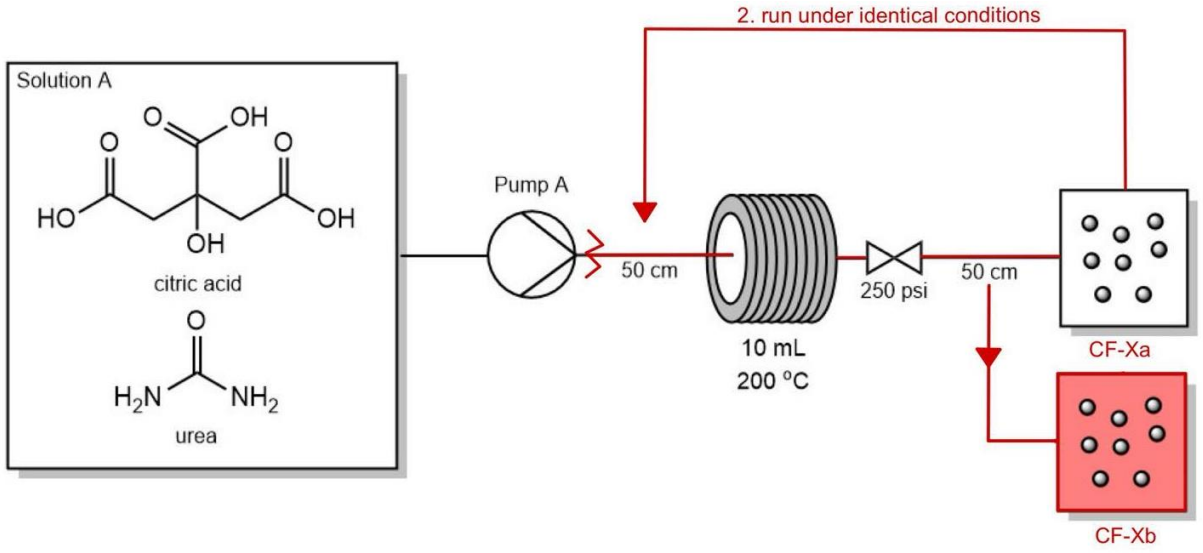

Figure 56: Illustration of the cascade reactions. The flow scheme is akin to Figure 18 in chapter 2.4.2. However, this have included the illustration of the product from ex. CF-8a was subjected to a second run under identical conditions to the first reaction, leading to CF-8b.

Gas evolution during the reaction posed significant challenges overall. The pressure graphs in Figure 43 illustrate the pressure fluctuations observed during the cascade experiments, highlighting differences between the first and second runs. The initial run exhibited significant pressure fluctuations and a higher rate of gas evolution throughout. In contrast, the second run showed a

notable reduction in gas evolution. While some fluctuations persisted, the pressure was generally more stable, typically hovering around 20 bars.

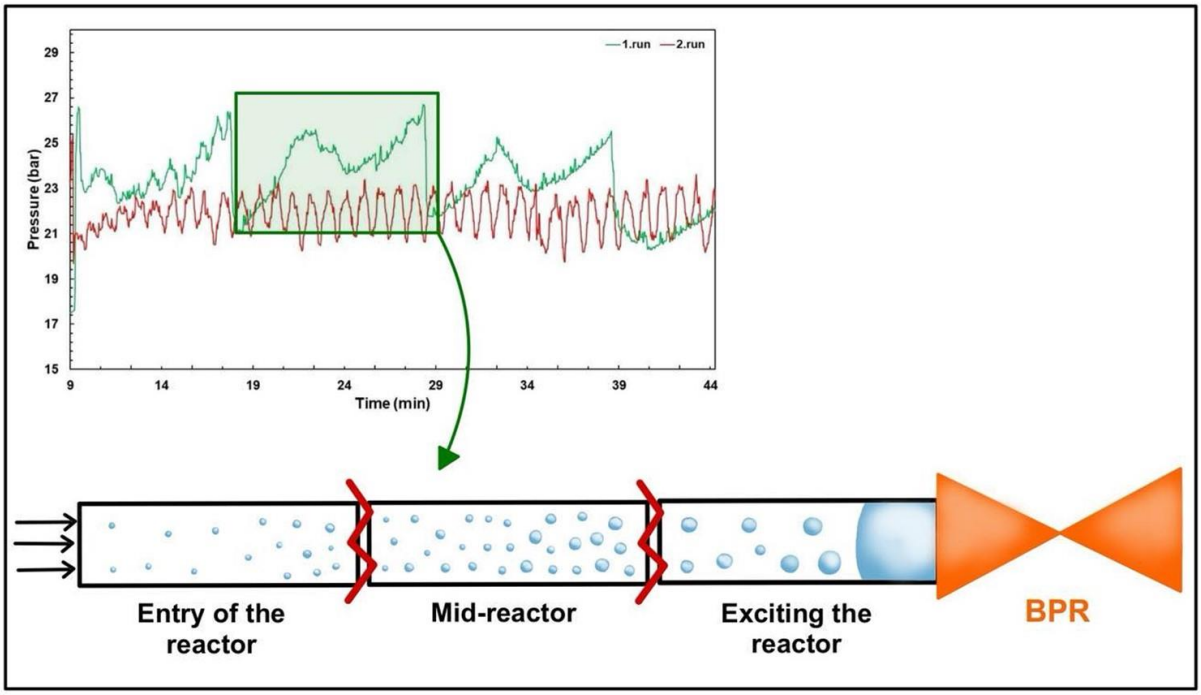

Figure 57: The potential development of gas inside the reactor, divided into three stages. Initially, reactants enter the reactor and begin to produce gas molecules gradually. As these gas molecules accumulate, the gas volume and pressure increase simultaneously. Once the gas volume reaches a critical point, the pressure forces the gas forward in the reactor until it reaches the BPR. Only when the pressure is sufficiently high does the gas escape through the BPR, causing a rapid drop in pressure. This cycle then restarts.

Figure 57 illustrates the potential stages of gas evolution within the reactor. In the initial stage, reactants enter the reactor, and gas molecules begin to form gradually. During the accumulation stage, gas production continues, leading to an increase in gas volume and pressure within the reactor. Finally, in the release stage, the accumulated gas is pushed forward by the rising pressure until it reaches the BPR. Once the pressure is high enough, the gas is released through the BPR, causing a rapid drop in pressure and the cycle restarts.

Consequently, gas generation transformed the single liquid flow stream into a gas-liquid segmented flow. Although this has several benefits, it also affects the flow rate, the residence time, and the mixing, ultimately impacting the CD size and size distribution.

Another consequence of the inconsistent flow rates is the potential for backmixing. Backmixing occurs when the reactants, intended to flow through the reactor continuously and uniformly, mix unintentionally. Pressure fluctuations contribute to hold-ups within the reactor. Each time gas accumulates, pressure nearly halts flow, resulting in longer residence times than anticipated. This situation may lead to incomplete mixing and insufficient flow control within the system, causing

portions of the fluid to mix with previously reacted or unreacted material. Ultimately leading to varying CD product quality and yield.

4.3 FL Spectroscopy: Characterization and Analysis of CD Samples

The PL properties of the CDs is a fascinating feature of the particles due to various applications (72). Typically, CDs exhibit wavelength-dependent emission spectra, with factors such as particle size, shape, and composition playing crucial roles in determining the PL characteristics. When discussing FL intensity, the unit is relative fluorescence units, and thus it will not be specified further.

4.3.1 Excitation-Dependent Emission Characteristics of CDs Synthesized by Different Methods

The emission spectra of varying excitation wavelengths for samples synthesized using microwave, furnace, and continuous flow methods, respectively, are presented in Figure 28a, 33a, and 44d. Bar diagrams (Figure 29, 34 and 45) are also provided to clearly depict the maximum excitation and corresponding maximum emission wavelength for each sample. The diagrams illustrate the excitation-dependent emission characteristics of CDs and to what degree the synthesis method influences this behavior. All emission spectra are provided in Appendix D.

Microwave samples:

For the MW samples, the emission peaks shifted to longer wavelengths and the FL intensity decreased as the excitation wavelengths varied from 280 nm to 380 nm (Figure 28a), exhibiting a red shift. This behavior is typical for CDs, indicating that the emission can be tuned by varying the excitation wavelength. The microwave samples exhibited a maximum FL at an excitation wavelength of 280 nm for every sample (Figure 28b), with the corresponding emission wavelength averaging around 311 nm.

Furnace samples:

The excitation-dependent emission character for the furnace samples is shown in Figure 33a. Generally, these samples exhibit emission peaks shifting to longer wavelengths ranging from 280 nm to 460 nm, with varying FL intensity dependencies. The individual emission wavelengths are given in the bar diagram (Figure 34), along with the maximum FL intensity. The samples show increasing FL intensity towards longer wavelengths. Specifically, F-6 and F-7 have the maximum emission at an excitation wavelength of 360 nm, F-3, F-5, and F-8 at 380 nm, and F-4 at 440 nm.

Continuous Flow samples:

Figure 44d depicts the excitation-dependent emission character for CF-5 samples. These samples also show different FL intensity maxima, with CF-1 to CF-4 having the maximum at 280 nm and CF-5 to CF-7 at 360 nm. The samples collected after 30 minutes, mostly have the maximum at 280 nm, except for CF-6*, which deviates with a maximum at 360 nm. The cascade experiments had a maximum excitation wavelength of 280 nm, with the corresponding emission maximum averaging around 311 nm, like the microwave experiments.

4.3.2 Emission Spectra and Fluorescence Intensity of CD Samples

Microwave samples:

The emission spectra for the MW samples at an excitation wavelength of 280 nm are presented in Figure 28b. On average, the MW samples had a maximum emission (~43 000) at 311 nm, with a range between 306 nm and 314 nm. MW-4 stood out with notably lower FL intensity compared to the other samples (~10 000).

Furnace samples:

Figure 35a-c depicts the emission spectra at the respective maximum excitation wavelengths for all furnace samples. Notably, samples F-4, F-6, and F-7 exhibited higher FL intensity, ranging from 6 000 to 10 000, compared to the rest of the samples, which exhibited weaker FL ranging from 2 000–3 000.

Continuous Flow samples:

CF-1 to CF-4, including CF-3*, had very weak FL intensity, almost negligible and ranging below 300, despite having the same maximum excitation wavelength. CF-5 was the only sample with strong FL, reaching 16 000 at an excitation wavelength of 360 nm. The corresponding sample, CF-5* exhibited much lower intensity and a maximum excitation at a lower wavelength at 280 nm. This discrepancy may be due to an issue during the dialysis procedure, where the tubing of CF-5 punctured after 24 hours. The sample was then diluted in 1 L water and dialyzed again for 48 hours, potentially altering its composition. CF-6 also had low intensity (<1 000), while its corresponding sample CF-6* had a similar graph shape and maximum, but with higher intensity (~3 000). CF-7, which was not dialyzed, had an FL intensity of about 6 000, likely due to the presence of emissive side-products enhancing FL.

Cascade experiments:

In the cascade experiments, the FL intensity was high (~32 000) after the first and second runs of 5 minutes (see Figure 46). As the residence time increased to 15 minutes, the intensity decreased to below 10 000 after the first run, but the second run sample had an intensity of 15 000. Longer residence times of 30 and 60 minutes showed further decreases in intensity, with the second run samples consistently showing higher intensity. The observed decrease in FL with increasing residence time suggests the formation of more defined carbon cores, aligning with the findings of Lu et al. (51). Fluorescent surface groups and nitrogen content typically enhance FL.

General observations:

There are many variations in emission intensities and maximum excitation and emission wavelengths. N-doping on the CD surface can introduce surface states that enhance FL (18). Consequently, CDs with higher urea (nitrogen content) concentrations exhibit stronger emission intensities. Despite the urea content, microwave samples consistently showed strong FL. Furnace samples F-6 and F-7, which had higher urea concentrations, also displayed higher FL intensity, with F-4 being an exception. Continuous flow experiments indicated that samples with higher urea content had higher FL intensity, while increased residence times led to decreased FL intensity.

4.4 UV-Vis Spectroscopy: Characterization and Analysis of CD Samples

In general, extracting chemical information from a UV-vis spectrum is challenging when the structure is unknown. The CD samples contain various particles and sizes, complicating the analysis. However, there are some guidelines that can help in the assessment.

4.4.1 Detailed UV-Vis Spectra Analysis of CD Samples from Different Synthesis Methods

All UV-vis spectra are provided in chapter 3. Figure 30 illustrates the CD samples from the MW experiments, excluding MW-1, which was unavailable for analysis. Among these, only MW-4 displayed a distinct absorption band at 332 nm, while the rest had too low absorption intensity to provide valuable information.

The UV-vis spectra for CD samples from the furnace experiments are divided into two figures (Figure 36a/b) due to the appearance of the spectra. Samples F-3 to F-6 lacked the distinct peak at 332 nm, which was present in F-7 and F-8, likely due to the higher urea concentration. While F-3 to F-6 showed an increase towards 332 nm, the peak was not as pronounced as in F-7 and F-8.

Figure 47 and 48 show the UV-vis spectra for the CF experiments. Figure 47a illustrates spectra for CF-1 to CF-7, excluding CF-5, which had a distinct peak at 332 nm (Figure 47b). CF-1 to CF-4, CF-6, and CF-7 showed similar trends to the furnace experiments, with an increase towards 332 nm but no distinct absorption band. Figure 47c presents spectra for samples denoted CF-X*, which generally matched the shape of the former samples, though CF-5* lacked the distinct peak as observed in CF-5. There are some differences in absorption intensity among the samples, but the preparation for the UV-vis measurements involved diluting the concentrated samples. Each sample was diluted according to its concentration to achieve similar absorption intensity, ensuring more accurate measurements by the instrument.

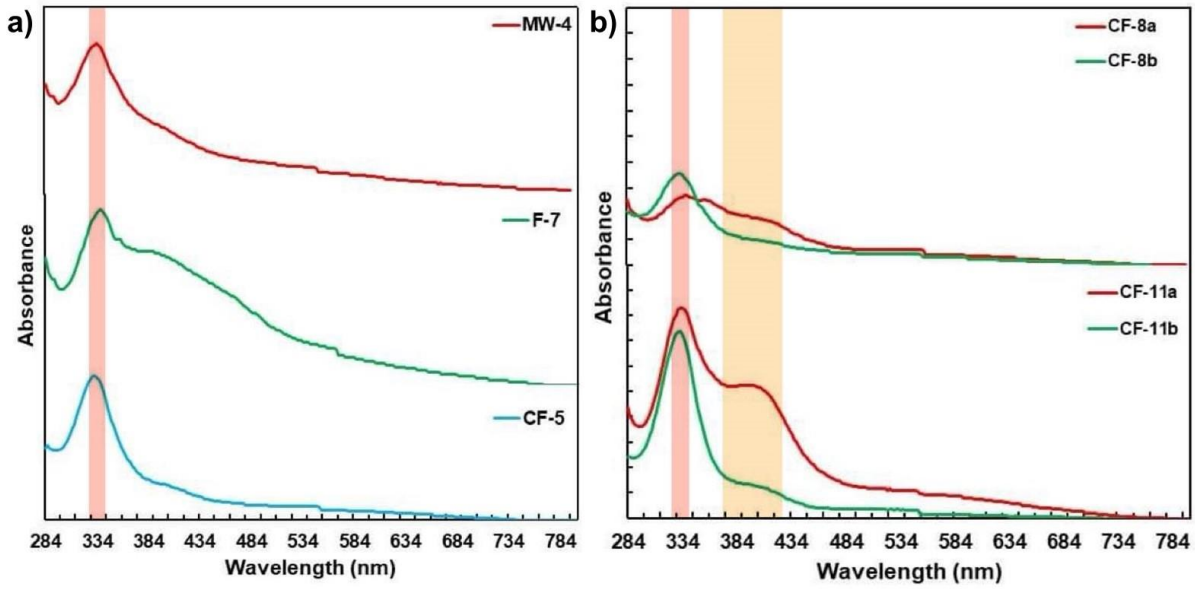

Figure 58: Comparing UV-vis spectra. a) UV-vis spectra from each synthesis method: microwave, furnace and continuous flow. All spectra have the distinct peak at 332 nm. b) UV-Vis spectra from the cascade experiments. The samples analyzed include CF-8a/b and CF-11a/b, denoting the respective residence times of 5 minutes and 60 minutes. All spectra have the same distinct peak at 332 nm and a shoulder at 396 nm.

The cascade experiments are depicted in Figure 48, with results separated into first and second runs. The comparison in Figure 58b shows CF-8a/b and CF-11a/b, representing 5- and 60-minutes residence times. Differences in dilution levels make intensity comparisons less important. However, as residence time increased, the shape became clearer, revealing two peaks. In the first run, there were two medium-intensity bands at 332 nm and a shoulder at 396 nm. In the second run, the band at 332 nm remained strong, while the 396 nm band decreased in intensity.

4.4.2 Guidelines for Interpreting UV-Vis Spectra of CD Samples

According to "Introduction to Spectroscopy" by Pavia et al. (69), a single band in the 250-360 nm region with no significant absorption at shorter wavelengths usually indicates an n→π* transition, involving atoms like O and N, such as in C=O, C=N, N=N, or –COOH groups. Given the

undefined structure of the CDs, identifying specific absorption bands and the causes is challenging. Previous research has documented n→π* transitions corresponding to carbonyl compounds and π→π* transitions related to aromatic sp2 bonds (69, 71, 72, 84, 85).

Different studies assign varying wavelengths to these transitions. For example, Yang et al. (85) attributed a peak at 278 nm to the n→π* transition of C=O and π→π* transition of C=C. In contrast, Yu et al. (84) reported peaks at 220 nm (π→π* transition of C═C) and 281 nm (n→π* transition of C═O) for the undoped CDs. In the UV-vis spectrum of N-doped CDs it was observed weak absorption peaks at 278 and 340 nm.

Generally, the reported absorption maxima of CDs are below 258 nm. Measuring these low wavelengths requires using a quartz cuvette and a UV-transparent solvent. Since the CD measurements were conducted using a plastic cuvette and water, the UV-vis spectra are cut off at 284 nm due to absorption interference. To achieve measurements comparable to previous work, the proper equipment and solvents must be used.

4.5 Interpretation of FT-IR Spectra: Broad Peaks and Molecular Environment

In all IR spectra there are broad peaks with significant overlap, indicative of a complex molecular environment. The wide peaks suggest a range of molecular vibrations occurring across various functional groups, resulting in overlapping signals. This complexity makes precise peak identification challenging, requiring careful analysis and interpretation of the spectral data. The broad peaks observed in the IR spectra may arise from a variety of factors, including multiple functional groups present within the CD samples, hydrogen bonding interactions, or the presence of impurities.

4.5.1 Comparative Analysis of CD IR Spectra from Each Synthesis Method

While it remains challenging to precisely identify all peaks observed in the IR spectra, some notable observations can be made. Figure 59 provides a suggested breakdown of potential bond vibrations present in the CD samples. Specifically focusing on CF-11a, where the CA to urea ratio was 1:1 and the residence time in the flow reactor was 60 minutes, several distinct features emerge.

The presence of the carbonyl group (C=O) at 1702 cm^{-1} is a prevalent observation across most samples, with exceptions noted in CF-1 to CF-4. Notably, the carbonyl peak becomes more pronounced as the CA to urea ratio reaches 1:1, distinctly appearing in samples CF-6 to CF-11 (see Figure 49 and 50). Conversely, this observation is not mirrored in the microwave and furnace samples.

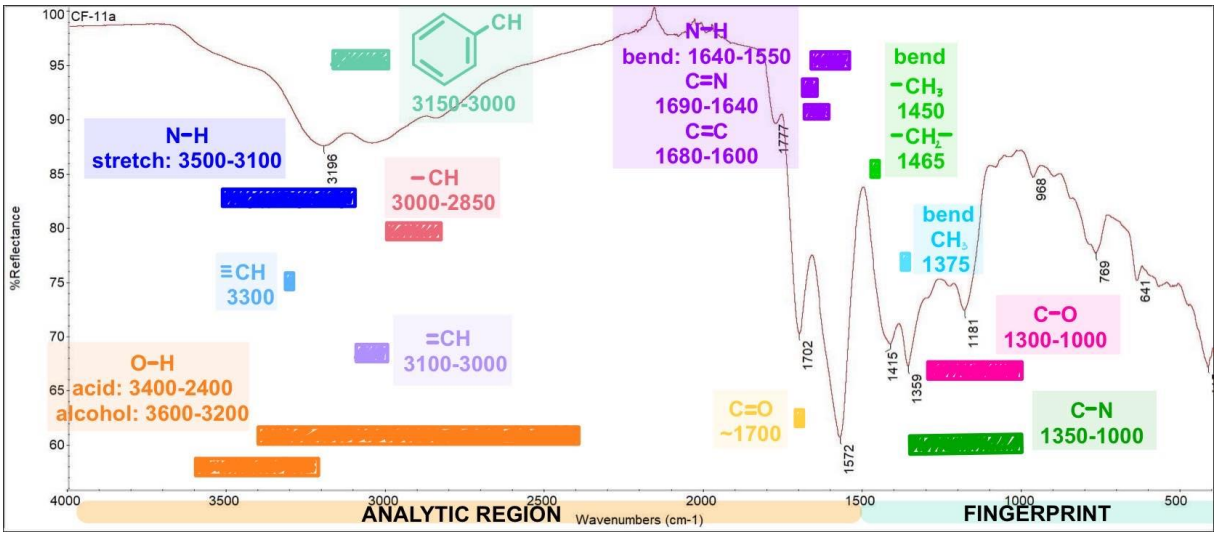

Figure 59: Utilizing the correlation chart in Pavia et al. (69), the wavenumbers are employed to elucidate potential bond vibrations present in the samples. Specifically, the analysis is focused on sample CF-11a.

Similarly, the peak around 1550-1570 cm^{-1} is consistently present in CF samples except CF-6. In furnace samples, the intensity increases with rising CA to urea ratio towards 1:1, while in microwave samples, the peak is not detected. The identification of the peak is challenging, but it may correspond to a N–H bending vibration, potentially explaining its emergence with increasing urea concentration. The region between 1700-1500 cm^{-1} may also be influenced by overlapping vibration modes such as C=N and C=C.

In the analytical region, a broad peak is observed, likely representing various vibrations such as stretching vibrations of N–H, O–H, ≡CH, =CH, –CH, and aromatics. In the fingerprint region, numerous peaks are present, making determination of the specific vibration modes difficult. Potential vibration modes include bending vibrations from $–CH_3$, $–CH_2–$, or C–O and C–N vibrations.

An important consideration is the potential impact of sample preparation on the spectra. Many experiments resulted in low yields, making direct measurement with FT-IR challenging, so that the product had to be dissolved in a solvent. Despite efforts to increase concentrations through solvent evaporation, the results did not improve. The low intensity of the IR spectra may make some signals sensitive to noise interference, leading to potential misinterpretations.

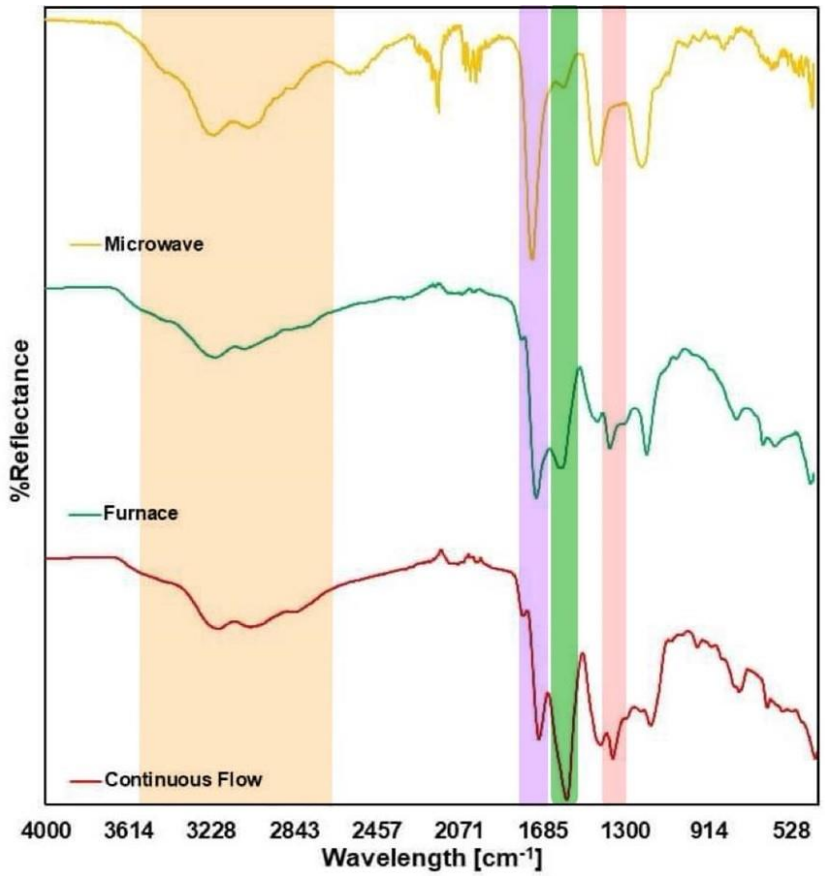

Figure 60: Comparing FT-IR spectra from each synthesis method. FT-IR spectra representing F-8 (furnace), MW-4 (microwave) and CF-11a (continuous flow). The highlighted areas represent differences and similarities across the spectra.

In summary, while the IR spectra exhibit overall similarity, a notable distinction lies in the peak around ~1350 cm^{-1} (highlighted in pink in Figure 60). Pinpointing its precise origin remains undetermined due to its location in the fingerprint region. Moreover, other characteristic peaks are consistent across all spectra: a prominent stretch near 3000 cm^{-1} (orange region), a carbonyl stretch at ~1700 cm^{-1} (purple region), and a peak around ~1570-1580 cm^{-1} (green region).

4.5.2 Comparative Analysis of CD IR Spectrum and Second Derivative

The IR spectra from the CDs unveiled numerous peaks that overlapped, suggesting diverse chemical environments, and consequently leading to a lack of clear resolution in the peaks. To elucidate the spectral features more distinctly, second derivative spectroscopy was employed as a technique to enhance the resolution of overlapping peaks, a challenge not adequately addressed in the original spectrum (86).

In Figure 61, the initially broad peaks, suspected of comprising multiple underlying peaks, such as the C=O peak at 1706 cm^{-1}, or those exhibiting shoulders (e.g., 1385 cm^{-1}), are now distinctly

resolved. Specifically, the peak at 1706 cm^{-1} reveals two peaks at 1722 cm^{-1} and 1662 cm^{-1}. Similarly, the peak at 1385 cm^{-1} exhibits distinct individual peaks at 1436 cm^{-1} and 1384 cm^{-1}.

This observation underscores the existence of diverse chemical environments coupled to each vibrational frequency, contributing to broad peaks and altering of the original peaks.

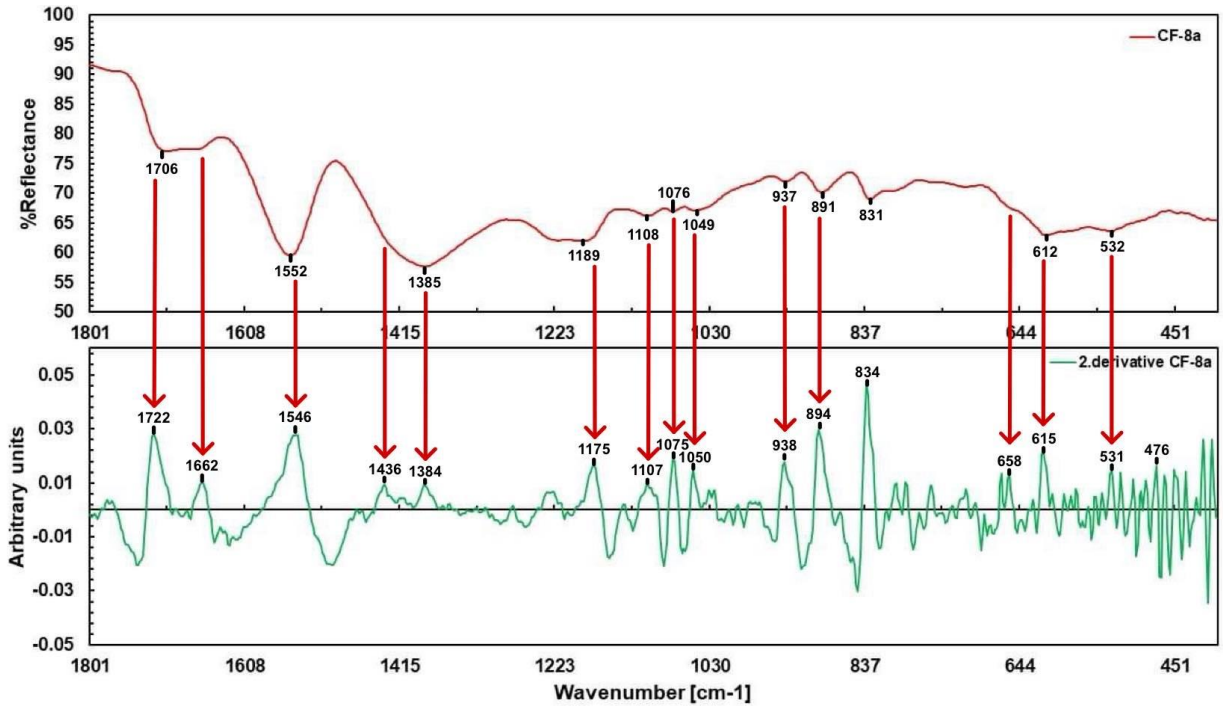

Figure 61: IR spectrum alongside its second derivative spectrum of CF-8a. The inclusion of the second derivative spectrum enhances the clarity of individual peaks, aiding in more detailed analysis of spectral features.

4.6 Challenges and Limitations of Raman Spectroscopy

Raman spectroscopy has been widely employed as a characterization technique for CD samples, as documented in previous studies (25, 72, 73), with particular interest centered around the observation of the D-band and G-band at 1350 cm^{-1} and 1585 cm^{-1}, respectively. However, the Raman analyses revealed significant hurdles in obtaining consistent and meaningful results.

Initially, there were promising resemblances to the characteristic bands of interest in some sample measurements. However, upon subsequent analysis, these signals were no longer present, leading to uncertainty regarding the reproducibility and reliability of the results. Consequently, it was deemed impractical to continue with further analyses, given the unpredictability of outcomes.

The primary challenge encountered was the dominance of solvent (2-propanol) and sample fluorescence in the recorded spectra. Initially, there was suspicion of analytical signals arising from the samples dissolved in 2-propanol solution. However, it became evident that the observed signals were attributed solely to the solvent itself. The overwhelming FL signal from the samples likely

masked the characteristic peaks associated with molecular vibrations, making it challenging to extract of meaningful information.

This observation parallels difficulties encountered in the DLS measurements, further complicating the attempts to obtain reliable data. Figure 53 displays spectra obtained from samples synthesized using microwave, furnace, and continuous flow methods, revealing consistent spectral characteristics resembling those of 2-propanol across all synthesis methods. Particularly, the yellow graph (F-7) also highlights FL interference.

Despite the employment of an alternative probe (ball probe), similar outcomes were observed, with only FL visible or no signals detected. Consequently, Raman spectroscopy was deemed unsuitable for further analysis due to the overwhelming FL background and limited analytical peaks.

4.7 Particle Size Analysis through DLS

The correlation coefficient graphs are an important tool to calculate the particle size values. The graph for polystyrene is considered as a "good" representation of a correlation graph, yielding reliable results (refer to Figure 55). Here, the Z-average value calculated was 63 nm, with corresponding PDI of 0.048 (see Table 9). A low PDI denotes a monodisperse sample. Conversely, the correlation graphs for CF-8b and CF-11a are categorized as "medium good" and "bad correlation", respectively.

In the case of polystyrene, the correlation coefficient graph exhibits a high degree of correlation, signifying the accuracy and reliability of the measurements. Conversely, CF-11a displays a low correlation, indicating poor agreement in data quality. CF-8b falls somewhere in between, implying moderate correlation. Consequently, this results in large Z-average values and a PDI > 0.5, indicative of polydisperse samples and diminished accuracy when employing DLS. The correlation graphs gradually decent to baseline at extended timescales, indicative of the presence of large particles.

Each graph illustrates the correlation coefficient values obtained from the analysis, with additional correlation graphs presented in Appendix G. Furthermore, an exemplar report from the "Expert Advice" section of the DLS software offers potential explanations for suboptimal results (see Appendix F). Sample FL and coloration are potential causes for the low count intensities and inferior data quality. The presence of such FL CDs presents a challenge as the emitted light may be registered as scattered light by the detector.

This led to the conclusion that the DLS measurements was inconclusive due to the CD samples being unsuitable for analysis.

4.8 TEM Analysis and Characterization of CDs

To delve deeper into the nanostructures of the CDs, TEM was employed to directly observe the morphology and particle size distributions. However, initial attempts were not as successful as anticipated.

Initially, some samples were evaluated for their suitability for TEM imaging. These samples were initially dissolved in water, which was considered as an unsuitable solvent for measurements based on recommendations from the Electron Microscopic Laboratory. The reasons stemmed from the risk of evaporation under vacuum conditions, which could lead to interference from water vapor and electron beam interactions with the sample, potentially resulting in contamination and instability.

The samples were evaporated and resuspended in a more suitable solvent. The first choice, ethanol, did not dissolve the samples completely. The ethanol was thus evaporated, and the samples were resuspended in 2-propanol. The multiple changes of solvents may have had adverse effect on the imaging conditions, making it more challenging. TEM images of two samples attempted for imaging, without success, are provided in Appendix J. The samples appeared unclear with little contrast, making it difficult for the microscope to focus.

In subsequent attempts, CD samples from cascade experiments were directly dissolved in 2-propanol after freeze-drying, aiming for improved results. TEM images of these samples are presented in Figure 51 and 52 in chapter 3.3.6. Despite challenges encountered in imaging, including low contrast and shadows or silhouettes of particles, some samples gave rise for successful imaging. Analysis of these TEM images revealed variations in contrast and morphology across the CD samples, indicating heterogeneous chemical environments. Notably, individual CD particles were directly observed, showcasing a diverse range of sizes and shapes within the sample. Additionally, a significant distance between each discovered particle indicated dispersion, while the presence of aggregates or clusters of CDs of different sizes further confirmed the heterogeneity of the sample.

These findings align with theoretical models suggesting the CD formation through complex pathways involving nucleation, growth, and surface passivation, resulting in diverse sizes and structures. The observations of heterogeneous chemical environments and diverse particle sizes in TEM images are consistent with previous characterization techniques, such as DLS measurements, FT-IR and FL spectroscopy analyses. The images reveal numerous clusters and aggregations, with fewer individual particles, suggesting that this material structure may contribute to the high FL

intensity observed in various samples. Backmixing within the reactor could potentially explain the characteristics of the CD product. The presence of an uneven flow profile and inconsistencies within the reactor might have altered the mixing dynamics. This could have resulted in incomplete mixing, where the fluids may not have fully reacted or have mixed with previously reacted fluids rather than with fresh reactants.

While CDs are typically reported to have sizes around 10 nm (72), the TEM images showed the smallest sizes ranging from 50-80 nm in diameter, often within clusters and aggregates. Contrary to these findings, Yang et.al. reported CDs at a size of 2 nm and no aggregation (85), while Yu et.al. obtained nearly spherical and well dispersed CD particles measuring 3 nm (84).

Overall, the TEM images indicate the presence of polymer-like side products and surface groups, which likely contribute to the formation of large aggregates and clusters observed in the samples.

4.9 Overall Insights: Challenges and Observations in CD Synthesis and Characterization

The analyses shed light on several key observations and challenges encountered in the synthesis and characterization of CDs.

The findings suggest that the carbonization process may not have been fully completed during the syntheses. Possible factors contributing to this include inadequate reaction conditions, such as insufficient heating or incomplete reaction times, leading to partially carbonized particles.

Addressing reactions generating significant gas presents challenges, particularly in achieving uniform mixing and controlling NP size distribution due to the formation of gas-liquid segmented flow. Consequently, the flow dynamics was disrupted, leading to non-uniform RTD and potentially impacting product quality. However, despite these challenges, a gas-liquid segmented flow can offer opportunities for improving mixing efficiency. By managing factors such as flow rates, channel design, and external control mechanisms, one can leverage the flow to overcome these challenges and achieve more consistent NP synthesis.

The particles remained incompletely carbonized and larger than expected. Possible reasons include incomplete conversion during synthesis, precursor impurities, inefficient dialysis, aggregation, incomplete surface passivation, and variations in the reaction conditions. While dialysis is intended to remove impurities and unreacted precursors, it can be affected by potential parameters that may hinder its efficiency and completeness. These factors include the choice of MWCO, the duration of dialysis, and the replacement of dialysis water. However, as stated by Ullal et al. (20), no universal method for purification and separation exists. Alternative techniques such as various

chromatography techniques, centrifugation, or solvent extraction may be explored to enhance product quality. Ensuring effective removal of impurities and unreacted precursors is crucial for obtaining high-quality CD products.

Moreover, aggregation of CD particles during synthesis or post-synthesis processing could also contribute to larger particle sizes. Aggregation may occur due to factors such as improper solvent choice or high particle concentration. Challenges were also encountered in the dissolution of CDs after freeze-drying, with both ethanol and 2-propanol presenting difficulties. Water turned out to be the optimal solvent for dissolution but was not ideal for certain characterization techniques.

These findings underscore the complexity of CD synthesis and purification, highlighting the importance of optimizing reaction conditions, purification methods, and solvent selection to achieve desired particle characteristics and enable accurate characterization. Furthermore, parallels can be drawn between purification and characterization techniques due to the absence of standard guidelines. Besides those employed in this study, other methods are available to gain information on CD structure, behavior and features. For instance, nuclear magnetic resonance spectroscopy, mentioned by Ullal et al. as "the most definitive and effective characterization technique," (20) and X-ray photoelectron spectroscopy offer valuable insights. These techniques complement the ones utilized in this research, contributing to a comprehensive understanding of CD properties.

5 Conclusion

5.1 Conclusive Analysis of CD Synthesis Methods: Microwave, Furnace, and Continuous Flow Techniques

In conclusion, this study reveals that each synthesis method presents its unique advantages and challenges. A notable finding was the occurrence of the pressure-related problems, which have been only scarcely documented in existing literature. This underscores the critical importance of carefully considering experimental conditions, particularly in continuous flow setups where pressure fluctuations can significantly impact the outcome of the synthesis process.

Purification and work-up techniques remain a challenge in CD synthesis. The CDs exhibited varying FL emission spectra, with differences in intensity and excitation wavelengths attributed to synthesis methods and experimental conditions. Furthermore, the FL intensity decreased with longer residence times in cascade experiments, suggesting the formation of more defined carbon cores. Generally, the samples exhibited distinct absorption peaks visible in most UV-vis spectra.

The FT-IR analyses revealed broad peaks indicative of a complex molecular environment, posing challenges for peak identification. Similar challenges were observed in DLS measurements, where inaccuracies in particle size determination were attributed to sample FL and the presence of large particles. Fluorescence issues also affected Raman measurements, with characteristic peaks originating from the solvent (2-propanol) rather than the samples.

TEM imaging confirmed the heterogeneous nature of CD samples, with diverse particle sizes and clusters indicating complex formation pathways. Notably, observed particle sizes were larger than previously reported, suggesting variations in synthesis methods or sample preparation.

Microwave synthesis offered speed and cleanliness but faced pressure limitations, resulting in suboptimal product yields. A closed system like the Biotage Initiator+ Synthesizer faced shutdowns before reactions could initiate. Furnace synthesis, on the other hand, bypassed pressure issues but required longer reaction times and higher energy consumption. Continuous flow synthesis showed promise for automation and scalability but faced challenges with gas evolution and pressure control, requiring extensive optimization for consistent results. Notably, no evident differences were observed in the products synthesized using the various methods.

The time frame of the project did not allow for running replicates of the experiments. Despite these challenges, each synthesis method offers potential for further development and application, highlighting the need for continued research and optimization in CD synthesis techniques.

6 Further Work

To guide future investigations in NP synthesis, the following sections outline key areas for further exploration and optimization.

6.1 Investigation of Advanced Reactor Designs and Control Strategies

Investigating advanced reactor designs and control strategies could optimize gas-liquid segmented flow for NP synthesis. This includes exploring the incorporation of a gas separation stage in the reactor design to manage excessive gas buildup and prevent the aggregation of gas bubbles. However, this integration poses challenges, particularly in high-pressure, high-temperature setups, where stability and leakage prevention are critical. Addressing these challenges is essential for successful implementation. Additionally, optimizing flow rates, reactant concentrations, and temperatures can help maintain desired reaction conditions and enhance gas-liquid segmentation.

6.2 Enhancement of Surface Passivation of CDs

Exploring alternative methods to improve surface passivation of CDs is crucial to prevent particle aggregation and control size. Surface passivation stabilizes particle surfaces, playing a critical role in synthesis. Investigating the use of citrate ions, known for stabilizing other NPs, could be promising. These ions can form a protective layer on the NP surface, inhibiting aggregation and enhancing stability. Researching the effectiveness of citrate ions in stabilizing CD particles could provide valuable insights for optimization and diverse applications.

6.3 Evaluation of Alternative Purification Techniques of CDs

While dialysis remains a common method for purifying CD solutions, exploring alternative purification techniques is necessary, especially considering the larger-than-expected particle sizes observed in this study. Techniques like thin-layer chromatography (87, 88) and high-performance liquid chromatography (33, 89) present viable options for effective purification and particle size control. Further assessment of these methods can optimize the CD solution purity and particle sizes.

7 References

1. Sharma A, Das J. Small molecules derived carbon dots: synthesis and applications in sensing, catalysis, imaging, and biomedicine. Journal of Nanobiotechnology. 2019;17(1):92.
2. Sousa HBA, Martins CSM, Prior JAV. You Don't Learn That in School: An Updated Practical Guide to Carbon Quantum Dots. Nanomaterials. 2021;11(3):611.
3. Wang Y, Hu A. Carbon quantum dots: synthesis, properties and applications. Journal of Materials Chemistry C. 2014;2(34):6921-39.
4. Zeng Q, Shao D, He X*, et al.* Carbon dots as a trackable drug delivery carrier for localized cancer therapy in vivo. Journal of Materials Chemistry B. 2016;4(30):5119-26.
5. Boakye-Yiadom KO, Kesse S, Opoku-Damoah Y*, et al.* Carbon dots: Applications in bioimaging and theranostics. International Journal of Pharmaceutics. 2019;564:308-17.
6. Xu X, Ray R, Gu Y*, et al.* Electrophoretic Analysis and Purification of Fluorescent Single-Walled Carbon Nanotube Fragments. Journal of the American Chemical Society. 2004;126(40):12736-7.
7. Sun Y-P, Zhou B, Lin Y*, et al.* Quantum-Sized Carbon Dots for Bright and Colorful Photoluminescence. Journal of the American Chemical Society. 2006;128(24):7756-7.
8. Sun Y-P. Carbon Dots: Exploring Carbon at Zero-Dimension. Cham, Switzerland: Springer International Publishing; 2020. Available from: https://doi.org/10.1007/978-3-030-41184-8_1.
9. Cayuela A, Soriano ML, Carrillo-Carrión C*, et al.* Semiconductor and carbon-based fluorescent nanodots: the need for consistency. Chemical Communications. 2016;52(7):1311-26.
10. Park H, Shin DJ, Yu J. Categorization of Quantum Dots, Clusters, Nanoclusters, and Nanodots. Journal of Chemical Education. 2021;98(3):703-9.
11. Vert M, Doi Y, Hellwich K-H*, et al.* Terminology for biorelated polymers and applications (IUPAC Recommendations 2012). Pure and Applied Chemistry. 2012;84(2):377-410.
12. Zhao X-X, Tao S-Y, Yang B. The Classification of Carbon Dots and the Relationship between Synthesis Methods and Properties. Chinese Journal of Chemistry. 2023;41(17):2206-16.
13. Zhu S, Song Y, Zhao X*, et al.* The photoluminescence mechanism in carbon dots (graphene quantum dots, carbon nanodots, and polymer dots): current state and future perspective. Nano Research. 2015;8(2):355-81.
14. International Union of Pure and Applied Chemistry (IUPAC). luminescence: IUPAC; 2019. Available from: https://doi.org/10.1351/goldbook.L03641.
15. LibreTexts Chemistry. Fluorescence and Phosphorescence: LibreTexts Chemistry; 2024 [cited 2024 26th May]. Available from:

https://chem.libretexts.org/Bookshelves/Physical_and_Theoretical_Chemistry_Textbook_Maps/Supplemental_Modules_(Physical_and_Theoretical_Chemistry)/Spectroscopy/Electronic_Spectroscopy/Fluorescence_and_Phosphorescence.

16. Atkins P, de Paula J. Elements of Physical Chemistry. 7 ed. New York, US: Oxford University Press; 2017. p. 449-86.
17. Jiang K, Sun S, Zhang L*, et al.* Red, Green, and Blue Luminescence by Carbon Dots: Full-Color Emission Tuning and Multicolor Cellular Imaging. Angewandte Chemie International Edition. 2015;54(18):5360-3.
18. Xu Q, Kuang T, Liu Y*, et al.* Heteroatom-doped carbon dots: synthesis, characterization, properties, photoluminescence mechanism and biological applications. Journal of Materials Chemistry B. 2016;4(45):7204-19.
19. Liu ML, Chen BB, Li CM*, et al.* Carbon dots: synthesis, formation mechanism, fluorescence origin and sensing applications. Green Chemistry. 2019;21(3):449-71.
20. Ullal N, Mehta R, Sunil D. Separation and purification of fluorescent carbon dots – an unmet challenge. Analyst. 2024;149(6):1680-700.
21. Ding H, Yu S-B, Wei J-S*, et al.* Full-Color Light-Emitting Carbon Dots with a Surface-State-Controlled Luminescence Mechanism. ACS Nano. 2016;10(1):484-91.
22. Wang L, Zhu S-J, Wang H-Y*, et al.* Common Origin of Green Luminescence in Carbon Nanodots and Graphene Quantum Dots. ACS Nano. 2014;8(3):2541-7.
23. Zhang Y, Yuan R, He M*, et al.* Multicolour nitrogen-doped carbon dots: tunable photoluminescence and sandwich fluorescent glass-based light-emitting diodes. Nanoscale. 2017;9(45):17849-58.
24. Wang F-T, Wang L-N, Xu J*, et al.* Synthesis and modification of carbon dots for advanced biosensing application. Analyst. 2021;146(14):4418-35.
25. Baker SN, Baker GA. Luminescent Carbon Nanodots: Emergent Nanolights. Angewandte Chemie International Edition. 2010;49(38):6726-44.
26. Wikipedia contributors. Laser Ablation: Wikipedia, The Free Encyclopedia.; 2024 [updated 29th February 2024; cited 2024 26 May]. Available from: https://en.wikipedia.org/w/index.php?title=Laser_ablation&oldid=1211078305.
27. Cheng Y, Chen Z, Wang Y*, et al.* Continuous synthesis of N, S co-coped carbon dots for selective detection of CD(II) ions. Journal of Photochemistry and Photobiology A: Chemistry. 2022;429:113910.

28. Shao M, Yu Q, Jing N*, et al.* Continuous synthesis of carbon dots with full spectrum fluorescence and the mechanism of their multiple color emission. Lab on a Chip. 2019;19(23):3974-8.
29. Rao L, Tang Y, Li Z*, et al.* Efficient synthesis of highly fluorescent carbon dots by microreactor method and their application in Fe^{3+} ion detection. Materials Science and Engineering: C. 2017;81:213-23.
30. Campalani C, Rigo D. Continuous flow synthesis and applications of carbon dots: a mini-review. Next Sustainability. 2023;1:100001.
31. He G, Shu M, Yang Z*, et al.* Microwave formation and photoluminescence mechanisms of multi-states nitrogen doped carbon dots. Applied Surface Science. 2017;422:257-65.
32. Alkian I, Prasetio A, Anggara L*, et al.* A Facile Microwave-Assisted Synthesis of Carbon Dots and Their Application as Sensitizers in Nanocrystalline TiO_2 Solar Cells. Journal of Physics: Conference Series. 2019;1204(1):012093.
33. Chen C-Y, Tsai Y-H, Chang C-W. Evaluation of the dialysis time required for carbon dots by HPLC and the properties of carbon dots after HPLC fractionation. New Journal of Chemistry. 2019;43(16):6153-9.
34. Devi JSA, Aparna RS, Aswathy B*, et al.* Understanding the Citric Acid–Urea Co–Directed Microwave Assisted Synthesis and Ferric Ion Modulation of Fluorescent Nitrogen Doped Carbon Dots: A Turn On Assay for Ascorbic Acid. ChemistrySelect. 2019;4(3):816-24.
35. Herrero MA, Kremsner JM, Kappe CO. Nonthermal Microwave Effects Revisited: On the Importance of Internal Temperature Monitoring and Agitation in Microwave Chemistry. The Journal of Organic Chemistry. 2008;73(1):36-47.
36. Tsuji M, Hashimoto M, Nishizawa Y*, et al.* Microwave-Assisted Synthesis of Metallic Nanostructures in Solution. Chemistry – A European Journal. 2005;11(2):440-52.
37. Polshettiwar V, Varma RS. Aqueous microwave chemistry: a clean and green synthetic tool for rapid drug discovery. Chemical Society Reviews. 2008;37(8):1546-57.
38. Mohamad Aziz NA, Yunus R, Kania D*, et al.* Prospects and Challenges of Microwave-Combined Technology for Biodiesel and Biolubricant Production through a Transesterification: A Review. Molecules. 2021;26(4):788.
39. Rabiller-Baudry M, Paquin L, Lepéroux C*, et al.* How microwaves can help to study membrane ageing. Environmental Technology. 2020;41(18):2314-36.
40. Chen S, Liu X, Li S*, et al.* Eco-friendly and efficient synthesis of nitrogen-doped carbon quantum dots for pH sensing applications. Applied Physics A. 2024;130(2):121.

41. Britannica T. Editors of Encyclopaedia. Sintering: Encyclopedia Britannica; 2024 [cited 2024 21th May]. Available from: https://www.britannica.com/technology/sintering.
42. Yan F, Sun Z, Zhang H*, et al.* The fluorescence mechanism of carbon dots, and methods for tuning their emission color: a review. Microchimica Acta. 2019;186(8):583.
43. Ma Z, Ming H, Huang H*, et al.* One-step ultrasonic synthesis of fluorescent N-doped carbon dots from glucose and their visible-light sensitive photocatalytic ability. New Journal of Chemistry. 2012;36(4):861-4.
44. Liu J, Li R, Yang B. Carbon Dots: A New Type of Carbon-Based Nanomaterial with Wide Applications. ACS Central Science. 2020;6(12):2179-95.
45. Zhang H-Y, Wang Y, Xiao S*, et al.* Rapid detection of Cr(VI) ions based on cobalt(II)-doped carbon dots. Biosensors and Bioelectronics. 2017;87:46-52.
46. Yin H, Manoharan MM, Truskewycz A*, et al.* A Portable RGB-Type Quantum Dot-Based Water Sensing Device for Heavy Metal Ion Detection. Journal of Nanosciences Research & Reports. 2024;6(2):1-4.
47. Li L, Yu B, You T. Nitrogen and sulfur co-doped carbon dots for highly selective and sensitive detection of Hg(II) ions. Biosensors and Bioelectronics. 2015;74:263-9.
48. Zhu C, Zhai J, Dong S. Bifunctional fluorescent carbon nanodots: green synthesis via soy milk and application as metal-free electrocatalysts for oxygen reduction. Chemical Communications. 2012;48(75):9367-9.
49. Gao G, Jiang Y-W, Yang J*, et al.* Mitochondria-targetable carbon quantum dots for differentiating cancerous cells from normal cells. Nanoscale. 2017;9(46):18368-78.
50. Zhao X, Tang Q, Zhu S*, et al.* Controllable acidophilic dual-emission fluorescent carbonized polymer dots for selective imaging of bacteria. Nanoscale. 2019;11(19):9526-32.
51. Lu Y, Zhang L, Lin H. The Use of a Microreactor for Rapid Screening of the Reaction Conditions and Investigation of the Photoluminescence Mechanism of Carbon Dots. Chemistry – A European Journal. 2014;20(15):4246-50.
52. Baumann M, Moody TS, Smyth M*, et al.* A Perspective on Continuous Flow Chemistry in the Pharmaceutical Industry. Organic Process Research & Development. 2020;24(10):1802-13.
53. Hessel V, Kralisch D, Kockmann N*, et al.* Novel Process Windows for Enabling, Accelerating, and Uplifting Flow Chemistry. ChemSusChem. 2013;6(5):746-89.
54. Illg T, Löb P, Hessel V. Flow chemistry using milli- and microstructured reactors—From conventional to novel process windows. Bioorganic & Medicinal Chemistry. 2010;18(11):3707-19.

55. Razzaq T, Kappe CO. Continuous Flow Organic Synthesis under High-Temperature/Pressure Conditions. Chemistry – An Asian Journal. 2010;5(6):1274-89.
56. Schwolow S, Neumüller A, Abahmane L*, et al.* Design and application of a millistructured heat exchanger reactor for an energy-efficient process. Chemical Engineering and Processing: Process Intensification. 2016;108:109-16.
57. Plutschack M, Pieber B, Gilmore K*, et al.* The Hitchhiker's Guide to Flow Chemistry. Chemical Reviews. 2017;117(18):11796-893.
58. Hessel V. Novel Process Windows – Gate to Maximizing Process Intensification via Flow Chemistry. Chemical Engineering & Technology. 2009;32(11):1655-81.
59. Newman SG, Jensen KF. The role of flow in green chemistry and engineering. Green Chemistry. 2013;15(6):1456-72.
60. Plouffe P, Macchi A, Roberge DM. From Batch to Continuous Chemical Synthesis—A Toolbox Approach. Organic Process Research & Development. 2014;18(11):1286-94.
61. Nambiar AG, Singh M, Mali AR*, et al.* Continuous Manufacturing and Molecular Modeling of Pharmaceutical Amorphous Solid Dispersions. AAPS PharmSciTech. 2022;23(7):249.
62. Zhao C-X, He L, Qiao SZ*, et al.* Nanoparticle synthesis in microreactors. Chemical Engineering Science. 2011;66(7):1463-79.
63. Marre S, Jensen KF. Synthesis of micro and nanostructures in microfluidic systems. Chemical Society Reviews. 2010;39(3):1183-202.
64. Rogers L, Jensen KF. Continuous manufacturing – the Green Chemistry promise? Green Chemistry. 2019;21(13):3481-98.
65. Wardencki W, Curylo J, Namiesnik J. Green Chemistry - Current and Future Issues. Polish Journal of Environmental Studies. 2005;14(4):389-95.
66. Vapourtec. RS-400 – Reactions and reagents automated: Vapourtec; 2024 [cited 2024 29th May]. Available from: https://www.vapourtec.com/products/r-series-flow-chemistry-system/reactions-and-reagents-automated-rs-400-features/.
67. Xiao W, Xu Z, Liu W*, et al.* Cascade Reaction: Science Direct; 2019 [cited 2024 25th May]. Available from: https://www.sciencedirect.com/topics/chemistry/cascade-reaction.
68. Leng Y. Materials Characterization. Introduction to Microscopic and Spectroscopic Methods. 2. ed. Weinheim, Germany: Wiley-VCH; 2013. p. 83-126.
69. Pavia D, Lampman GM, Kriz G*, et al.* Introduction to Spectroscopy. 5 ed. Boston, USA: Cengage Learning, Inc.; 2015. p. 14-30,577-82.
70. Tecan. Application Guide for Multimode Readers [Manual]: Tecan; 2024 [cited 2024 26th May]. Available from: https://lifesciences.tecan.com/multimode-plate-reader?p=tab--5.

71. Hu Q, Paau MC, Zhang Y*, et al.* Green synthesis of fluorescent nitrogen/sulfur-doped carbon dots and investigation of their properties by HPLC coupled with mass spectrometry. RSC Advances. 2014;4(35):18065-73.
72. John BK, Abraham T, Mathew B. A Review on Characterization Techniques for Carbon Quantum Dots and Their Applications in Agrochemical Residue Detection. Journal of Fluorescence. 2022;32(2):449-71.
73. Rooj B, Mandal U. A review on characterization of carbon quantum dots. Vietnam Journal of Chemistry. 2023;61(6):693-718.
74. Edinburgh Instruments. Raman Microscopy of Graphene: Edinburgh Instruments; 2024 [cited 2024 12th May]. Available from: https://www.edinst.com/application-note-raman-microscopy-of-graphene/.
75. Kjemisk Institutt UiB. IR-Dempet totalrefleksjon: Universitetet i Bergen; 2020 [cited 2024 13th May]. Available from: https://www.uib.no/kj/57213/ir-dempet-totalrefleksjon#gode-gratis-r-d-om-dtr-spektroskopi.
76. Nanoscience Instruments. Transmission Electron Microscopy: Nanoscience Instruments; 2024 [cited 2024 9th May]. Available from: https://www.nanoscience.com/techniques/transmission-electron-microscopy/.
77. Reimer L, Kohl H. Transmission Electron Microscopy. Physics of Image Formation. 5. ed. New York, US: Springer Science+Business Media, LLC; 2008. p. 1, 141-94.
78. Malvern Instruments. Zetasizer Nano Series User Manual [Manual]2004 [cited 2024 21st May].
79. Schaber PM, Colson J, Higgins S*, et al.* Thermal decomposition (pyrolysis) of urea in an open reaction vessel. Thermochimica Acta. 2004;424(1):131-42.
80. Wikipedia contributors. Citric Acid: Wikipedia, The Free Encyclopedia.; 2024 [updated 18th April 2024; cited 2024 27th May]. Available from: https://en.wikipedia.org/w/index.php?title=Citric_acid&oldid=1219620482.
81. Hu W, Dong Z, Ma Z*, et al.* W–Y_2O_3 composite nanopowders prepared by hydrothermal synthesis method: Co-deposition mechanism and low temperature sintering characteristics. Journal of Alloys and Compounds. 2020;821:153461.
82. Roy NK, Foong CS, Cullinan MA. Effect of size, morphology, and synthesis method on the thermal and sintering properties of copper nanoparticles for use in microscale additive manufacturing processes. Additive Manufacturing. 2018;21:17-29.
83. Ma X, Dong Y, Sun H*, et al.* Highly fluorescent carbon dots from peanut shells as potential probes for copper ion: The optimization and analysis of the synthetic process. Materials Today Chemistry. 2017;5:1-10.

84. Yu D, Wang L, Zhou H*, et al.* Fluorimetric Detection of Candida albicans Using Cornstalk N-Carbon Quantum Dots Modified with Amphotericin B. Bioconjugate Chemistry. 2019;30(3):966-73.
85. Yang X, Zhuo Y, Zhu S*, et al.* Novel and green synthesis of high-fluorescent carbon dots originated from honey for sensing and imaging. Biosensors and Bioelectronics. 2014;60:292-8.
86. Rieppo L, Saarakkala S, Närhi T*, et al.* Application of second derivative spectroscopy for increasing molecular specificity of fourier transform infrared spectroscopic imaging of articular cartilage. Osteoarthritis and Cartilage. 2012;20(5):451-9.
87. Zhou Y, Mintz KJ, Sharma SK*, et al.* Carbon Dots: Diverse Preparation, Application, and Perspective in Surface Chemistry. Langmuir. 2019;35(28):9115-32.
88. Fawaz W, Hasian J, Alghoraibi I. Synthesis and physicochemical characterization of carbon quantum dots produced from folic acid. Scientific Reports. 2023;13(1):18641.
89. Vinci JC, Ferrer IM, Seedhouse SJ*, et al.* Hidden Properties of Carbon Dots Revealed After HPLC Fractionation. The Journal of Physical Chemistry Letters. 2013;4(2):239-43.

8 Appendices

A 12 Principles of Green Chemistry

Table 10: The 12 principles of Green Chemistry presented by Wardencki et al. (65).

1	**Prevention**	Prevent waste rather than treating or cleaning up waste after it is formed.
2	**Atom Economy**	Design synthetic methods to maximize the incorporation of all materials used in the process into the final product.
3	**Less hazardous chemical syntheses**	Design synthetic methods to use and generate substances that minimize toxicity to human health and the environment.
4	**Designing safer chemicals**	Design chemical products that are fully effective yet have little or no toxicity.
5	**Safer solvents**	Use safer solvents and reaction conditions to minimize risks.
6	**Design for energy efficiency**	Minimize energy requirements and conduct processes at ambient temperature and pressure when possible.
7	**Use of renewable feedstocks**	A raw material or feedstock should be renewable rather than depleting whenever technically and economically practicable.
8	**Reduce derivative**	Minimize the use of blocking or protecting groups and temporary modifications.
9	**Catalysis**	Use catalytic reagents (as selective as possible) instead of stoichiometric reagents.
10	**Design for degradation**	Design chemical products so they break down into other products that do not persist in the environment.
11	**Real-time analysis for pollution prevention**	Develop analytical methodologies to allow for real-time monitoring and control of hazardous substances.
12	**Inherently safer chemistry for accident prevention**	Choose substances and the form of a substance used in a chemical process to minimize the potential for chemical accidents, including explosions, fires, and releases to the environment.

B Biotage Initator: Report

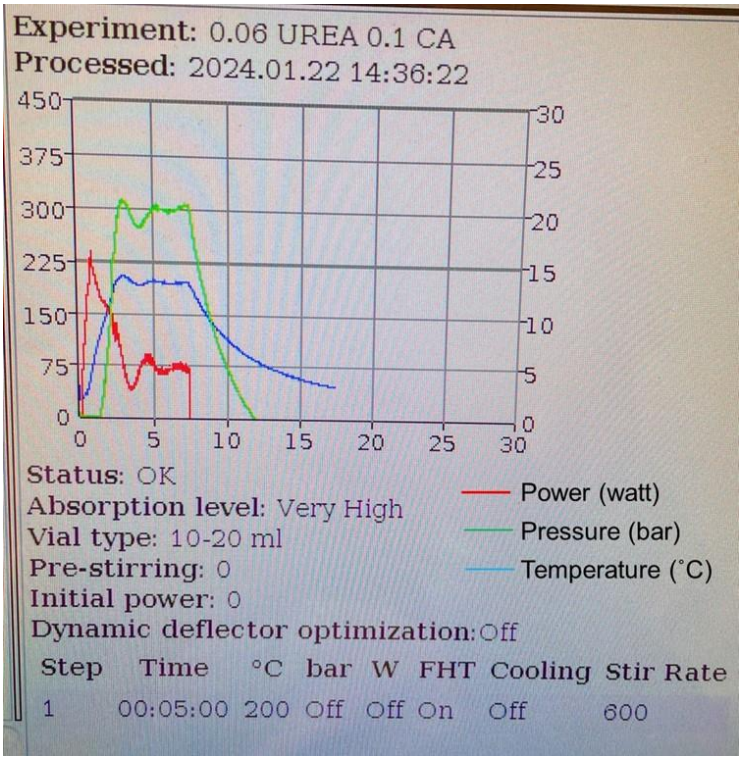

Figure A1: Example of an experiment reported from the Biotage Initator+ Synthesizer.

C FL Instrument Settings

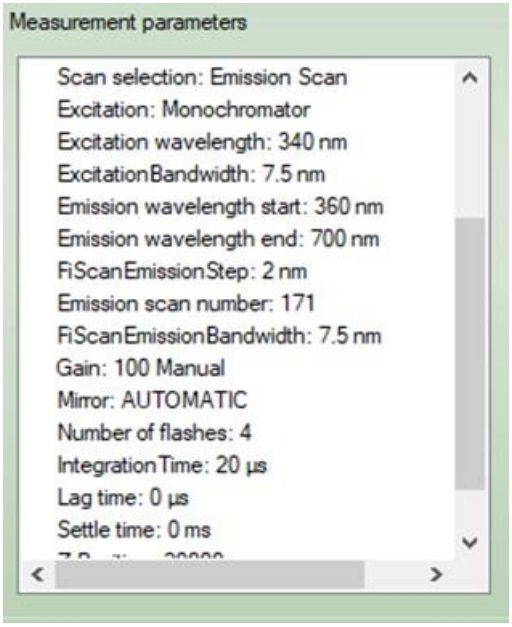

Figure A2: Detailed instrument settings from the FL instrument, Tecan (SPARK) 96-well plate reader.

D FL Emission Spectra for All CD Samples

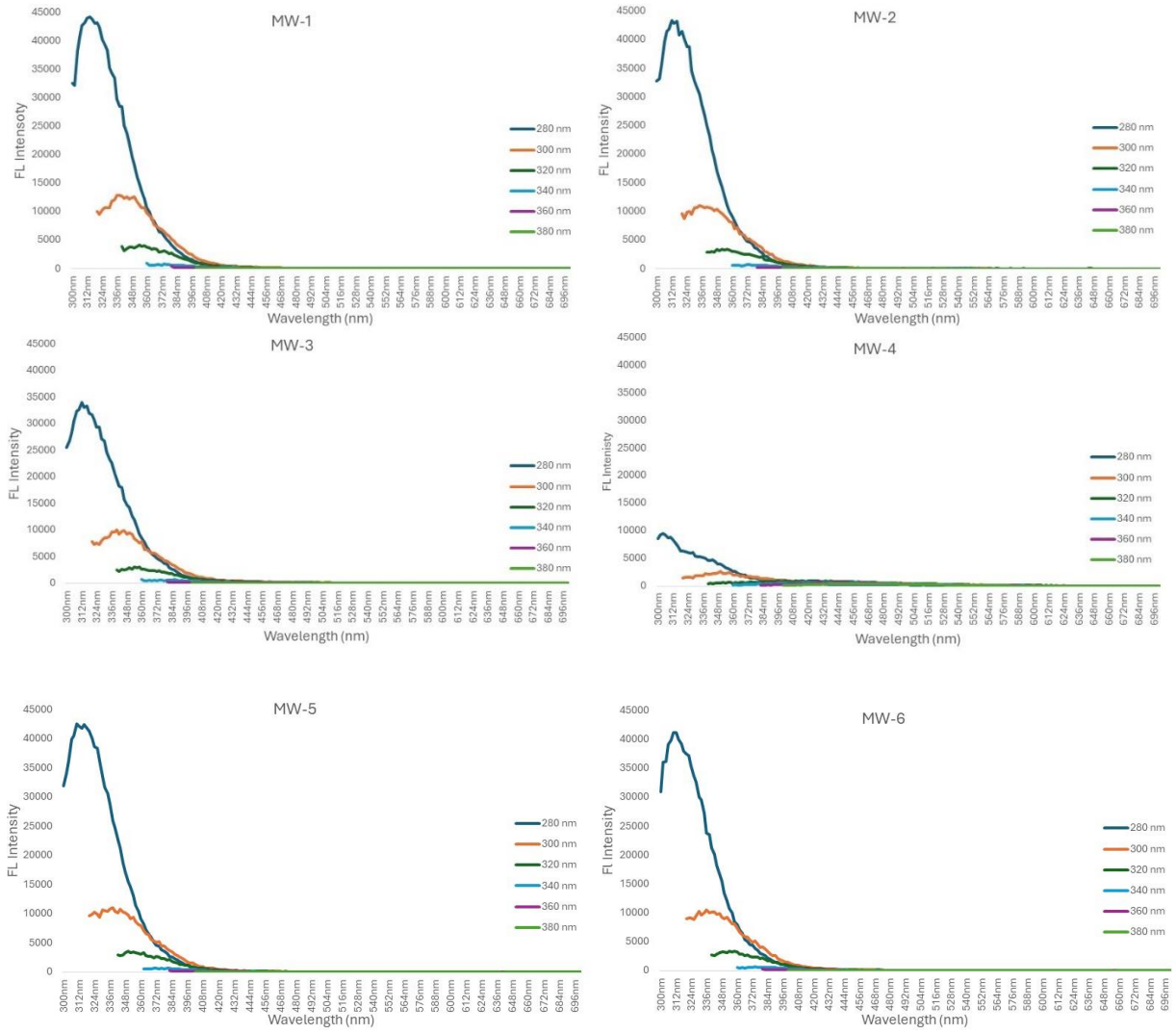

Figure A3: FL emission spectra for CD samples synthesized with a microwave synthesizer.

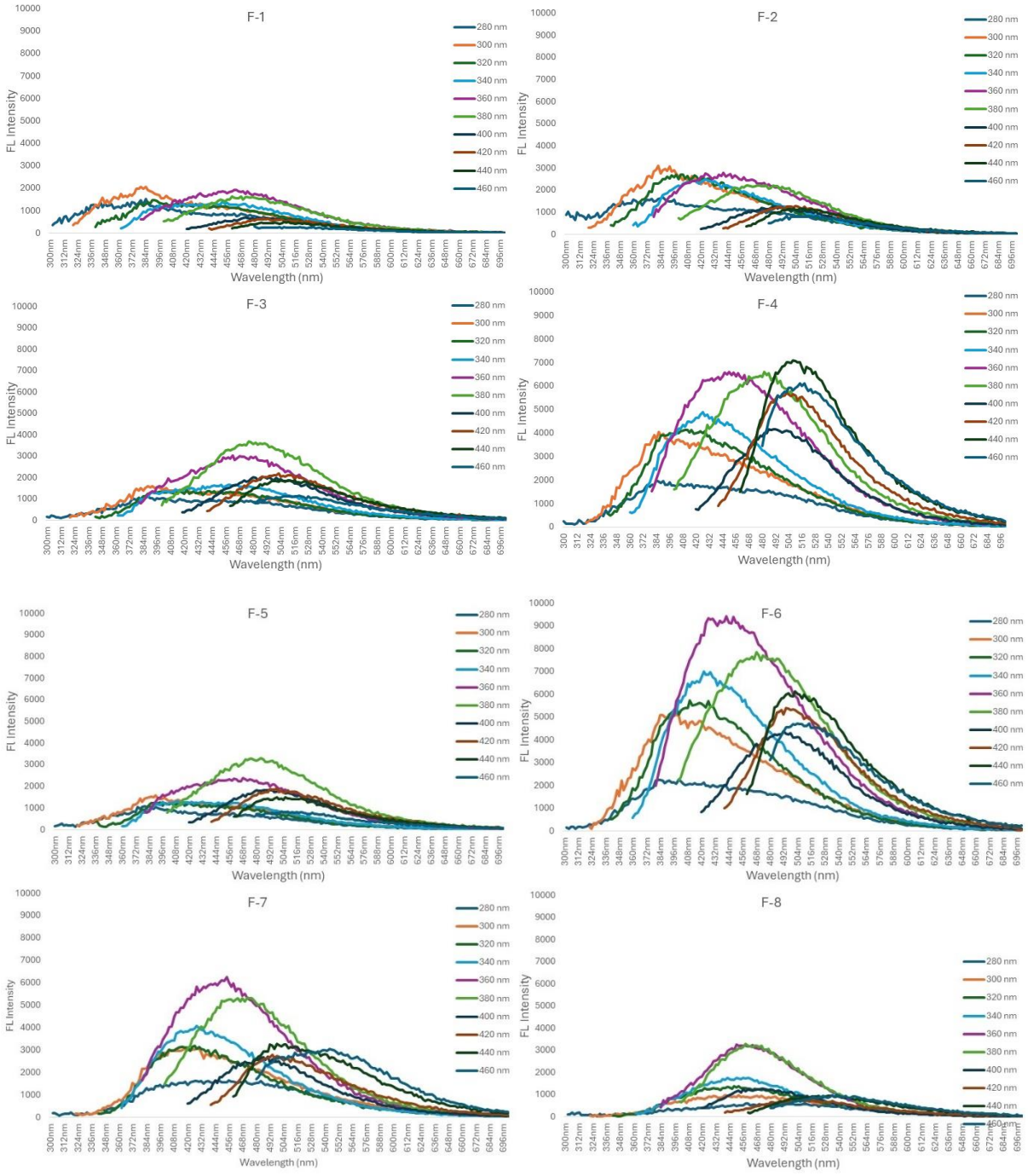

Figure A4: FL emission spectra for CD samples synthesized in a furnace.

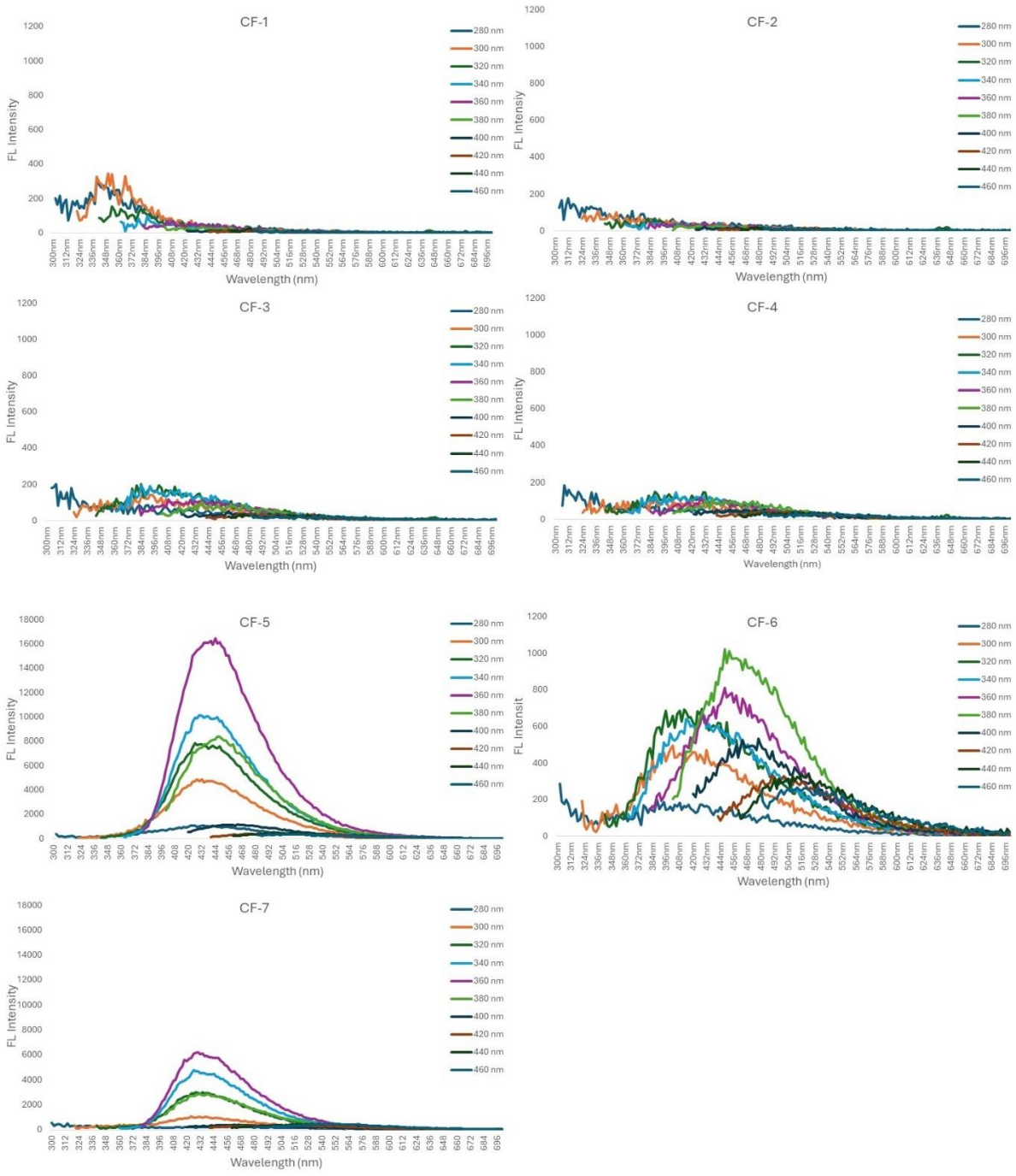

Figure A5: FL emission spectra for CD samples synthesized using a continuous flow setup.

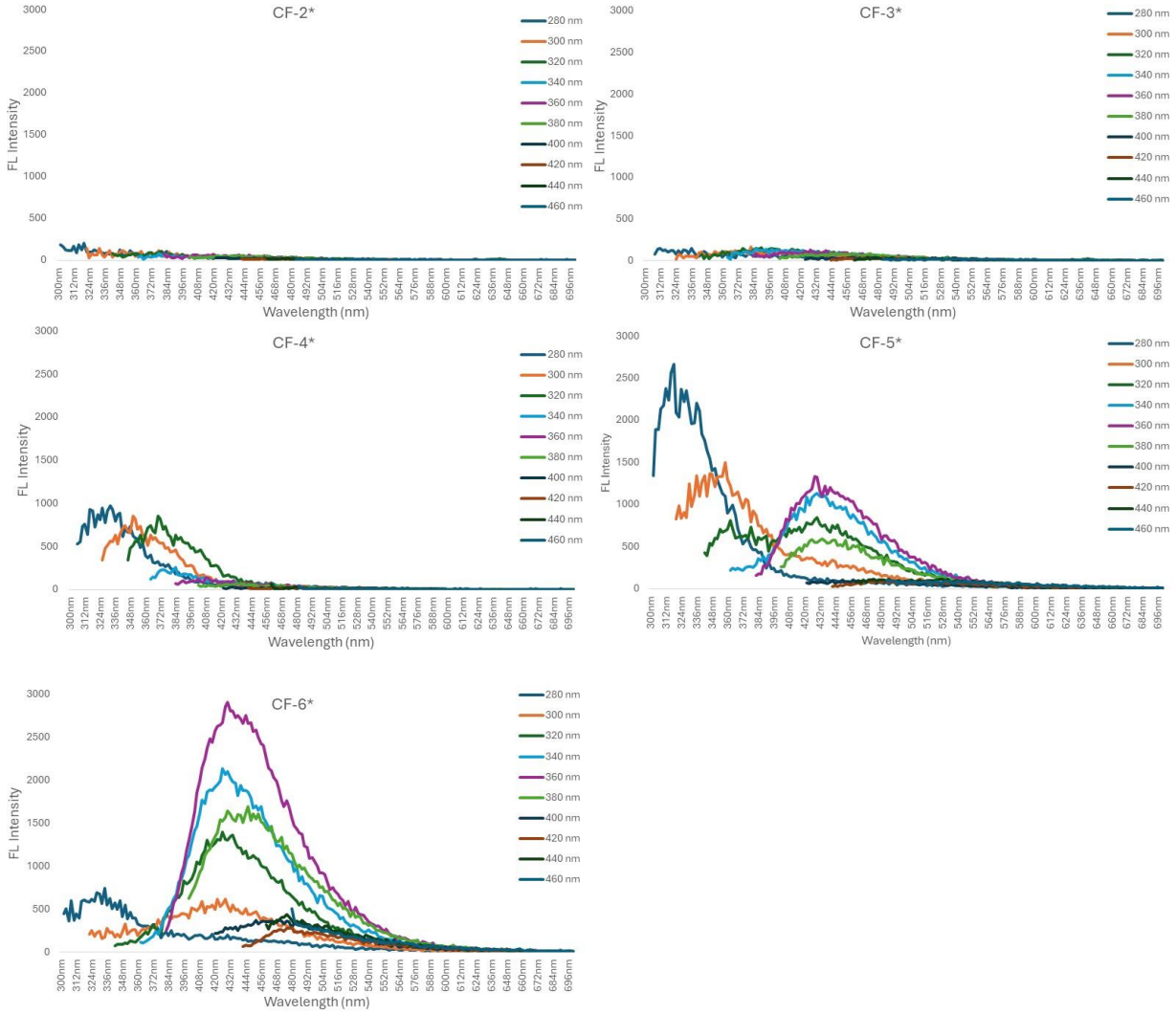

Figure A6: FL emission spectra for samples synthesized using a continuous flow setup, collected during the final 30 minutes of the process.

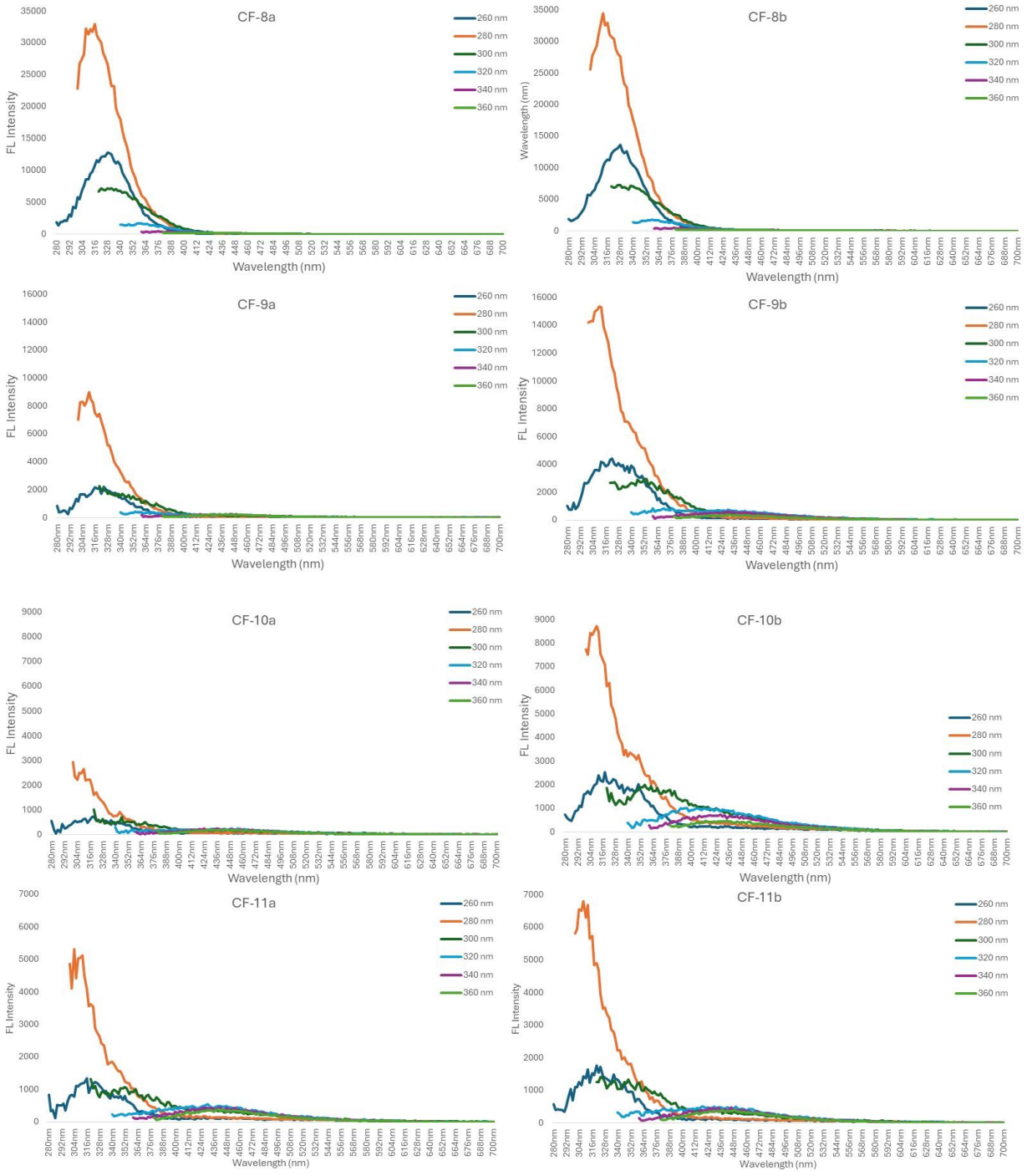

Figure A7: FL emission spectra for CD samples from the cascade experiments.

E Vapourtec System: Pressure Fluctuations

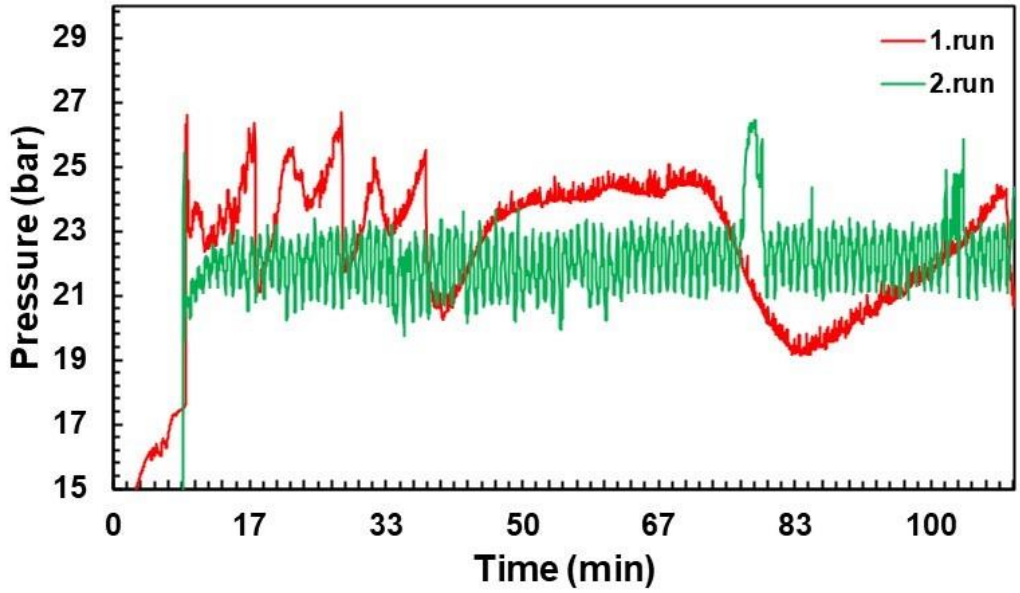

Figure A8: Complete pressure graphs illustrating the pressure fluctuations reported from the R-series software during the cascade reactions.

F DLS Expert Advice

Expert Advice

Size measurements

Polydispersity index is very high (1.000).
- Sample is very polydisperse and may not be suitable for DLS measurements.
- Sample contains large particles/aggregates/dust.
- Wrong measurement position selected.

In range figure is low (55%).
- Presence of large or sedimenting particles.
- Sample fluorescence.
- Sample absorbance (coloured samples).

Cumulant fit error high.
- Data quality too poor for cumulant analysis.
- Sample too polydisperse for cumulant analysis.

Multimodal fit error high.
- Data quality too poor for distribution analysis.
- Sample too polydisperse for distribution analysis.

Figure A9: Example of an "Expert Advice" report generated from the ZetaSizer software after a DLS measurement.

G DLS: Correlation Graphs

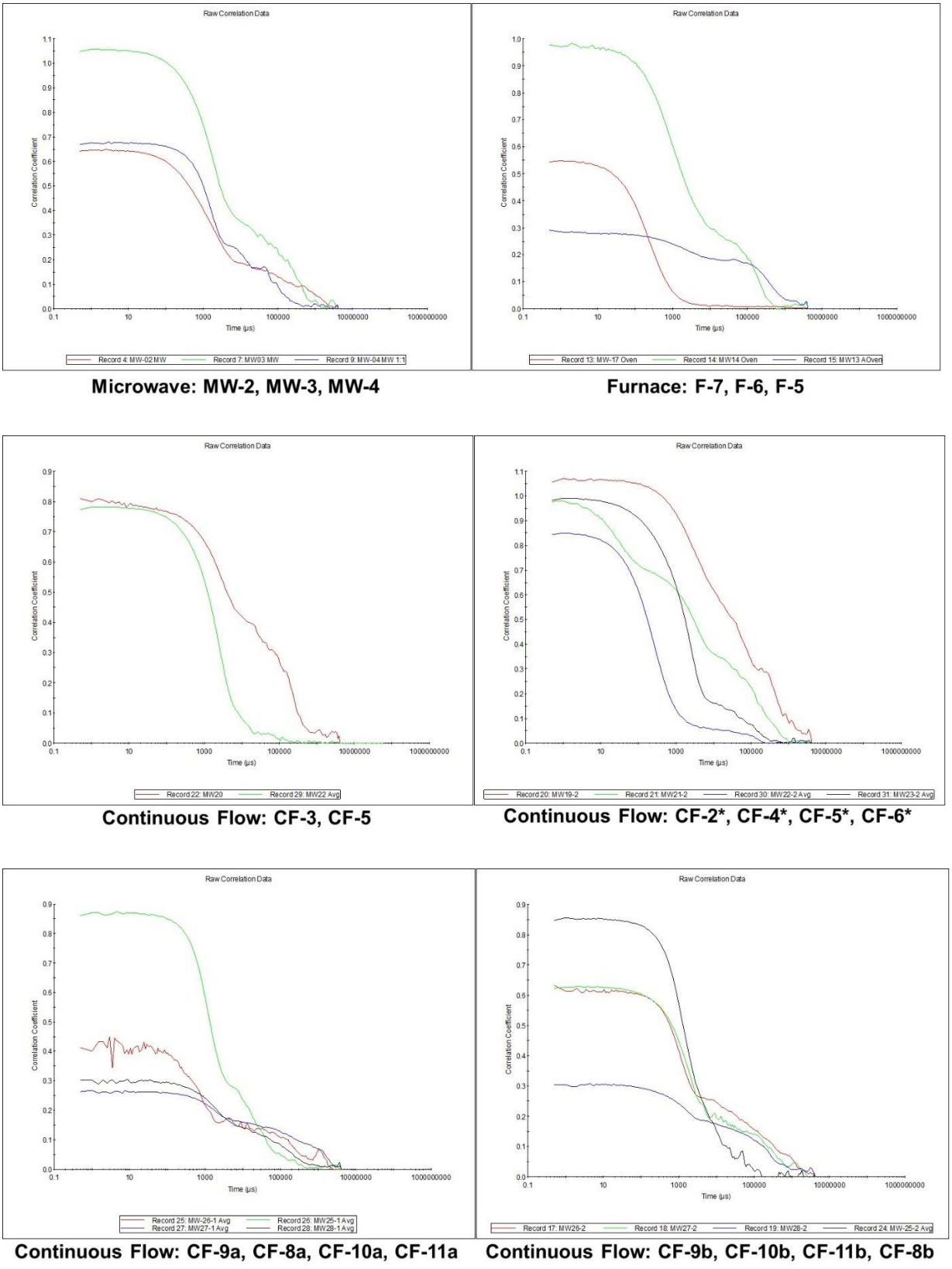

Figure A10: The correlation coefficient graphs for experiments conducted using microwave, furnace, and continuous flow. Samples are labeled in the order of their presentation at the bottom of the figure, providing clarity regarding the coloring.

H DLS: Size Measurement Graphs

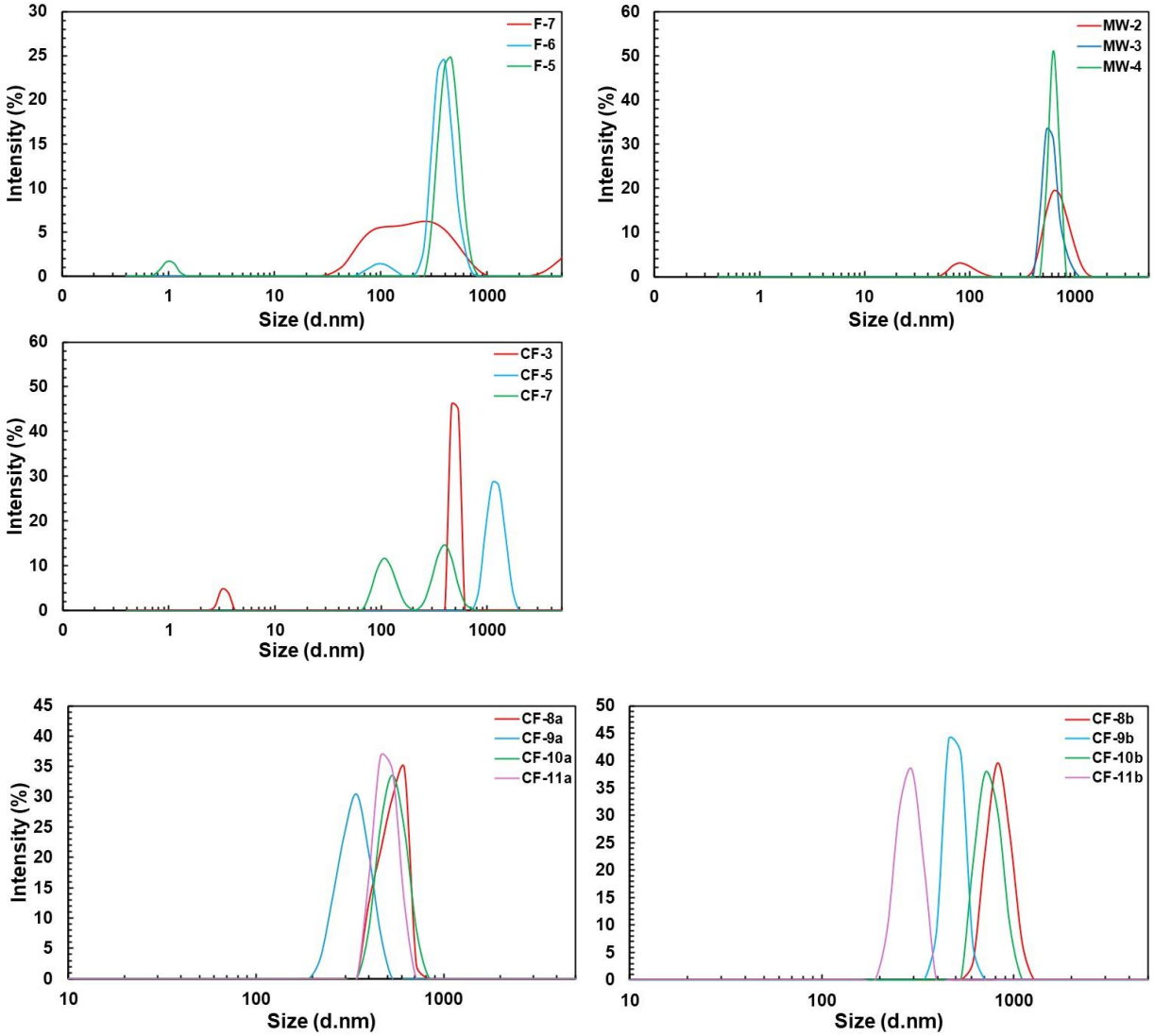

Figure A11: Size measurement graphs for the CD samples that were analyzed with DLS. All samples are presented according to their respective intensity (%).

I FT-IR Spectra

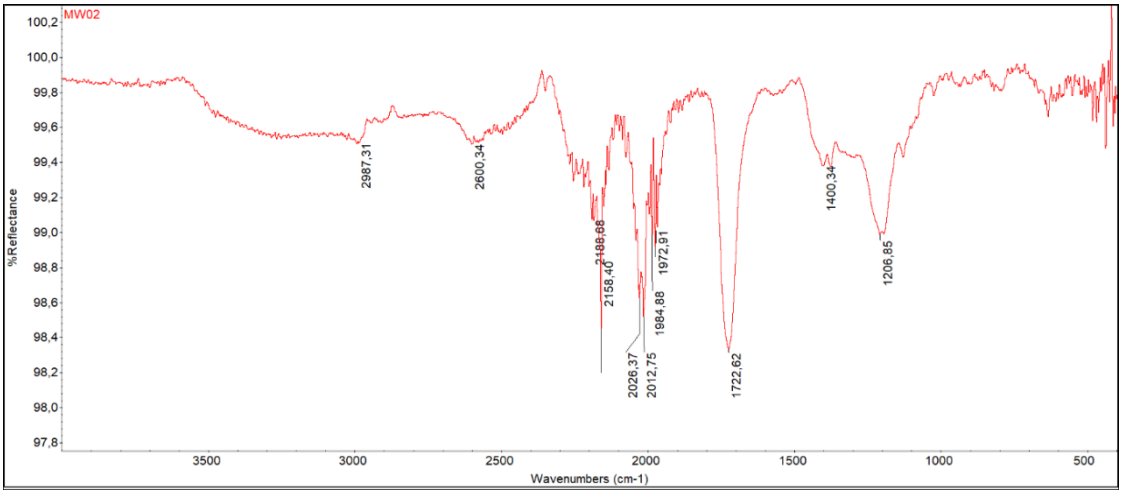

Figure A12: FT-IR Spectrum for MW-2.

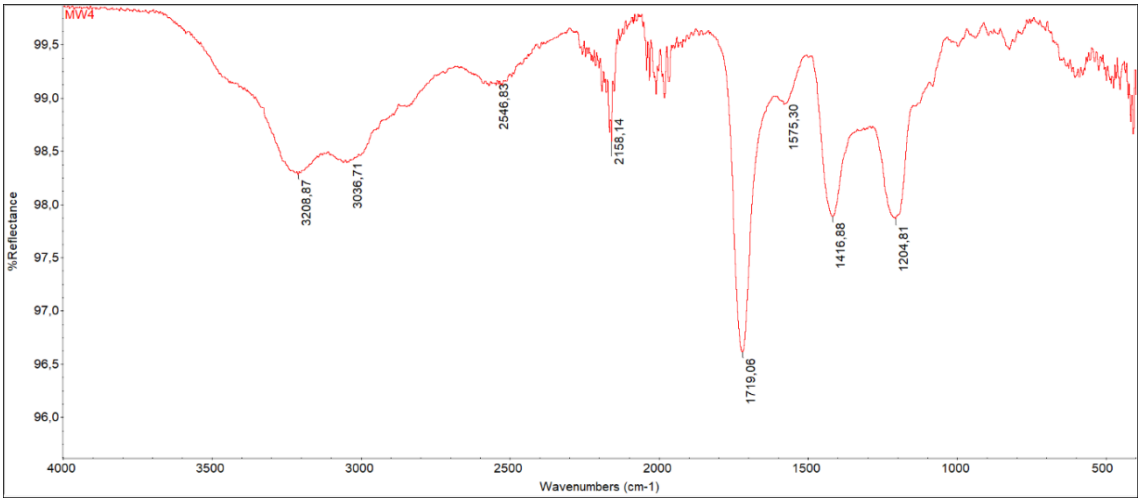

Figure A13: FT-IR Spectrum for MW-4.

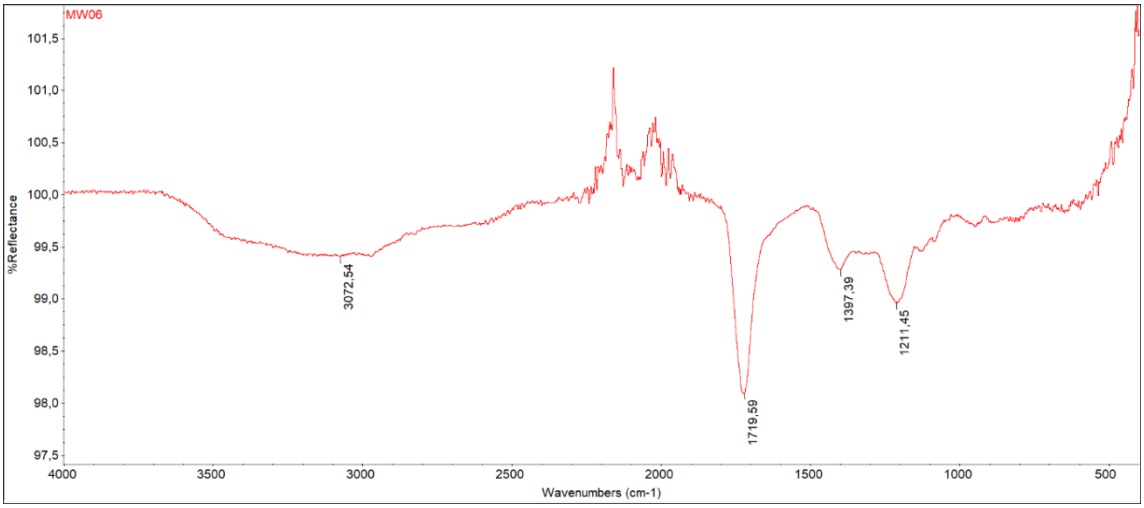

Figure A14: FT-IR Spectrum for MW-5.

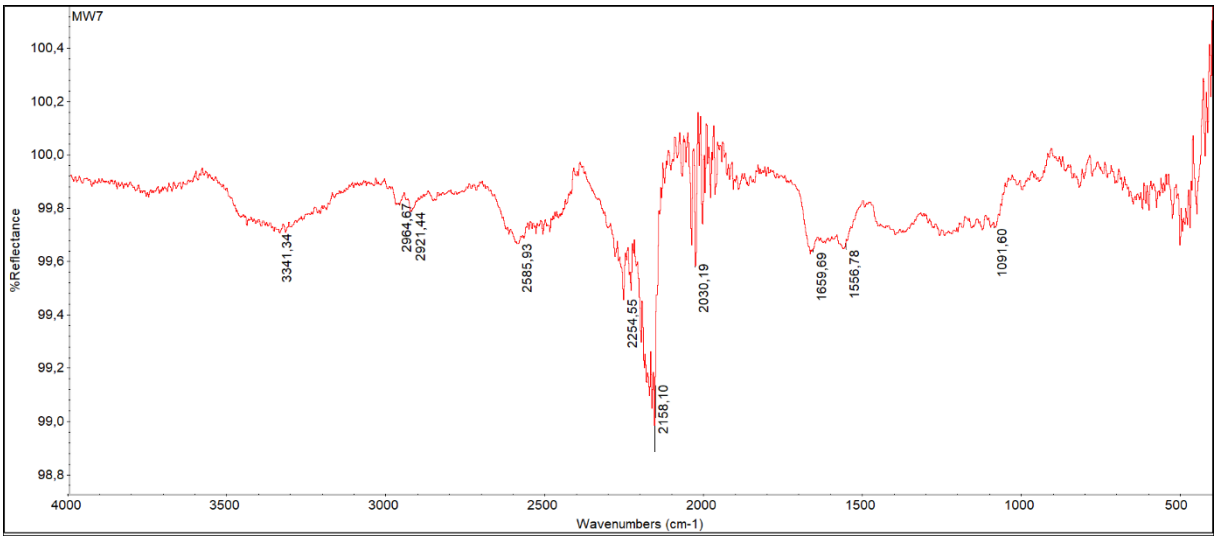

Figure A15: FT-IR Spectrum for MW-6.

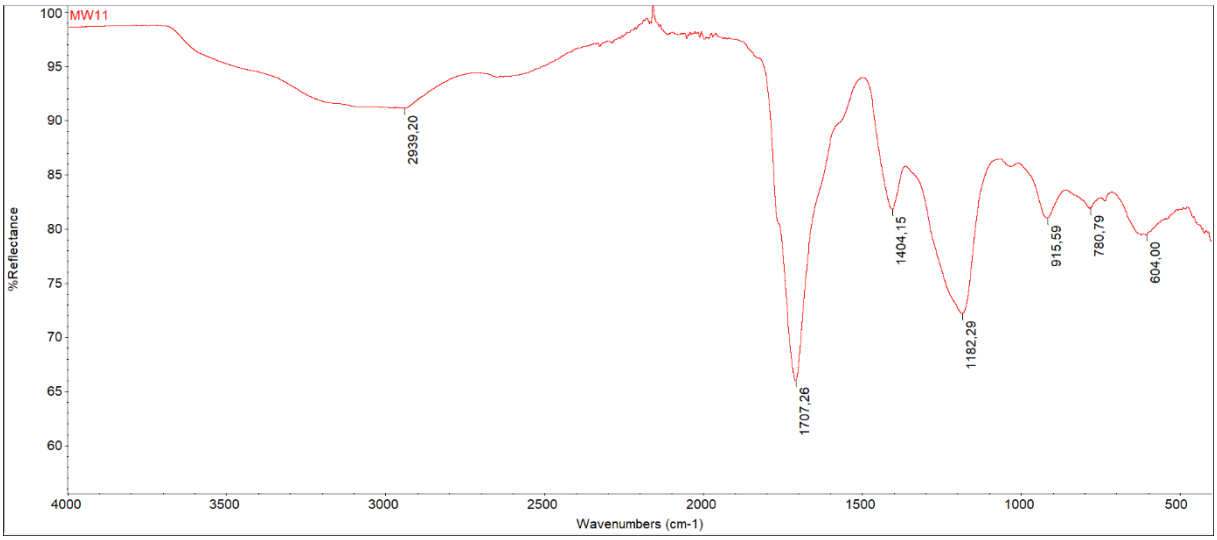

Figure A16: FT-IR Spectrum for F-3.

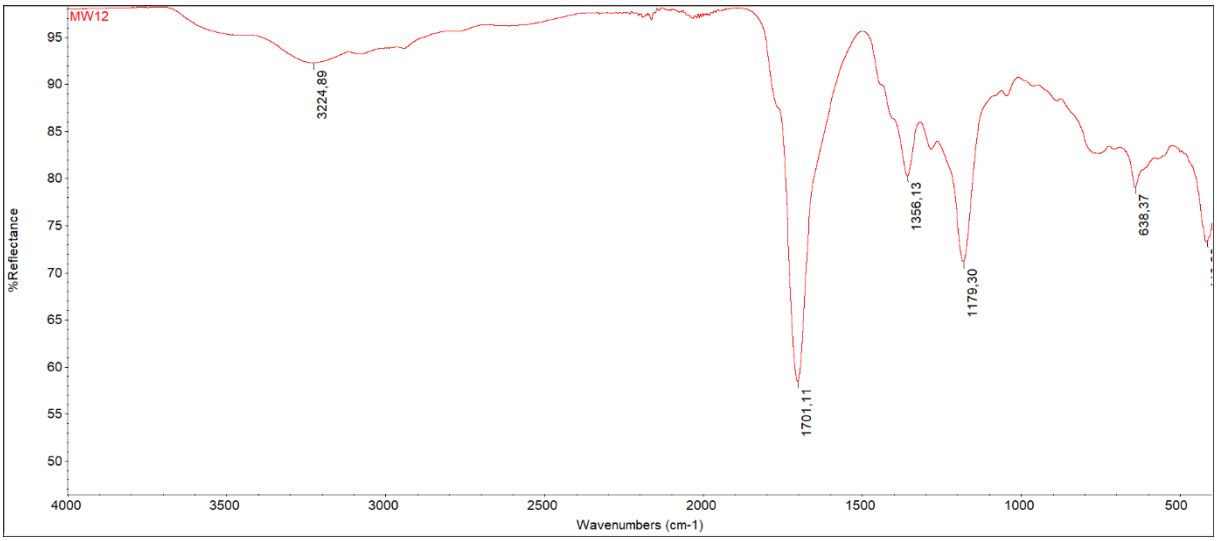

Figure A17: FT-IR Spectrum for F-4.

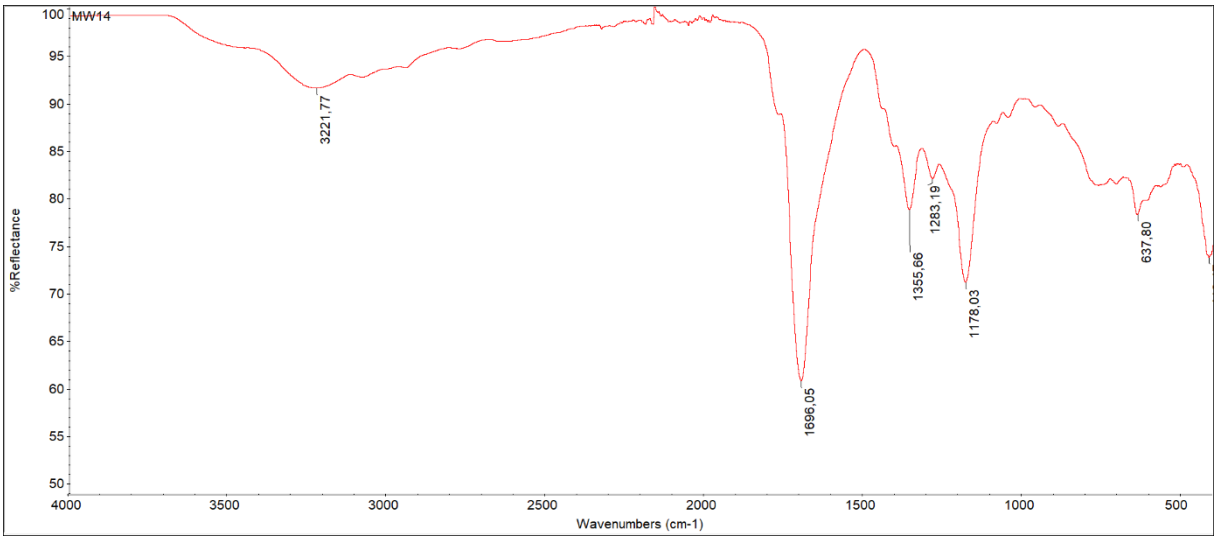

Figure A18: FT-IR Spectrum for F-6.

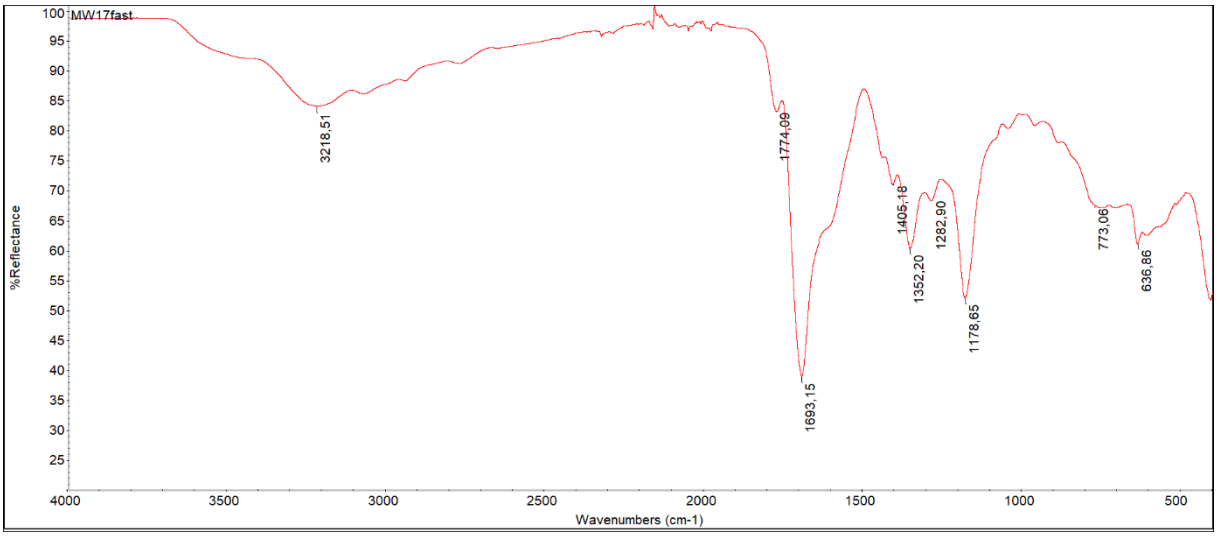

Figure A19: FT-IR Spectrum for F-7.

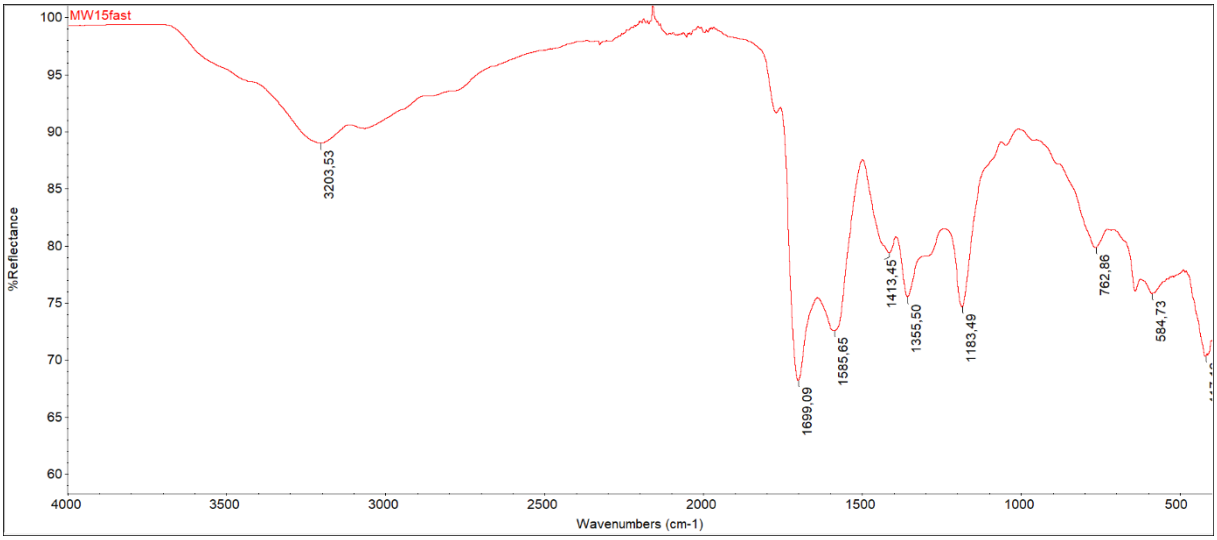

Figure A20: FT-IR Spectrum for F-8.

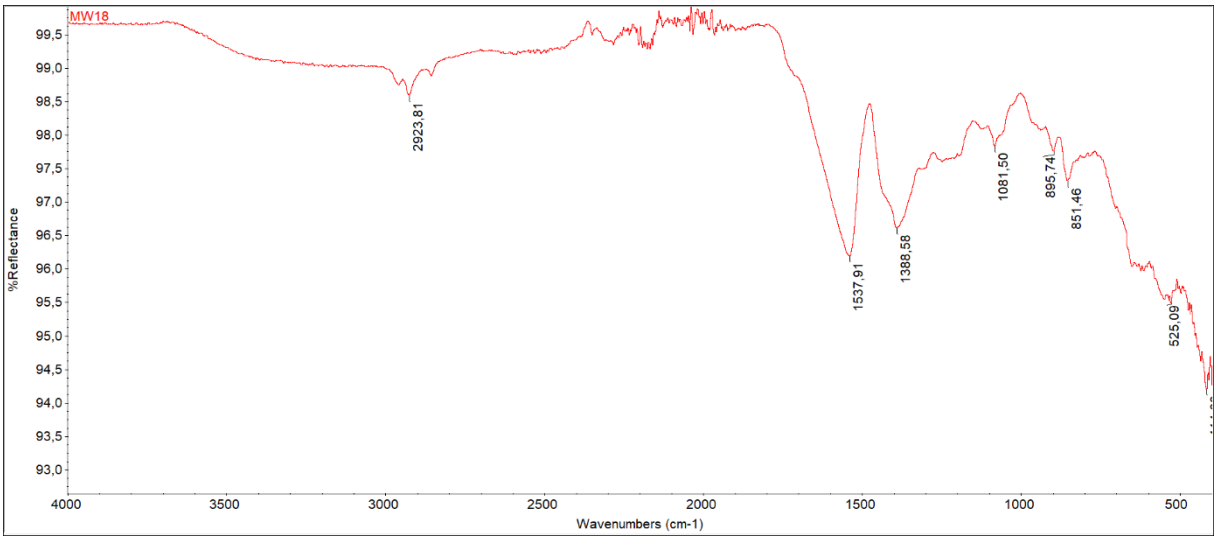

Figure A21: FT-IR Spectrum for CF-1.

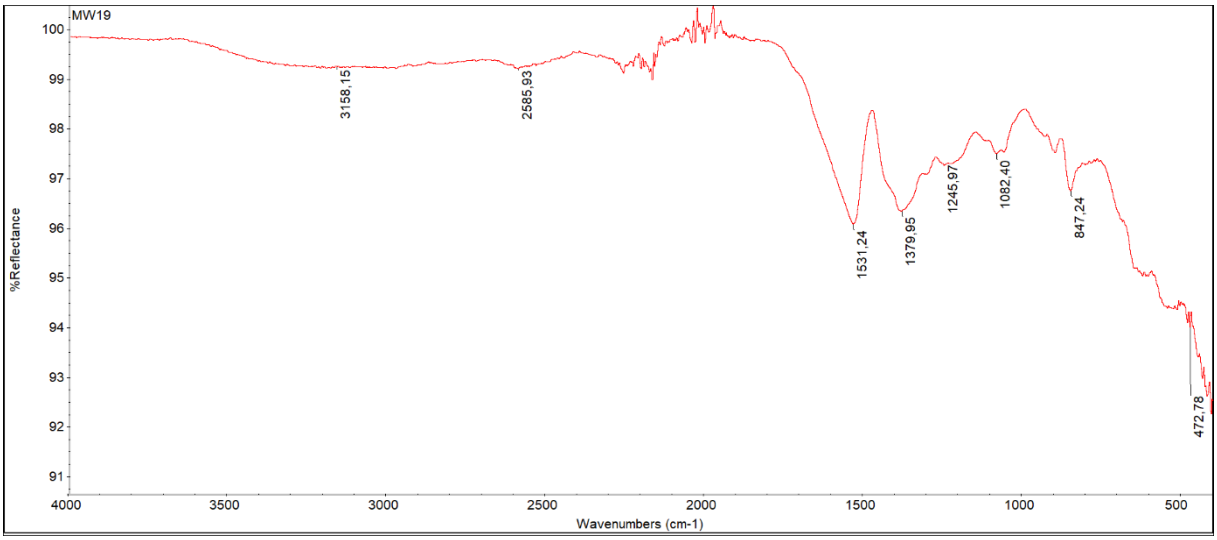

Figure A22: FT-IR Spectrum for CF-2.

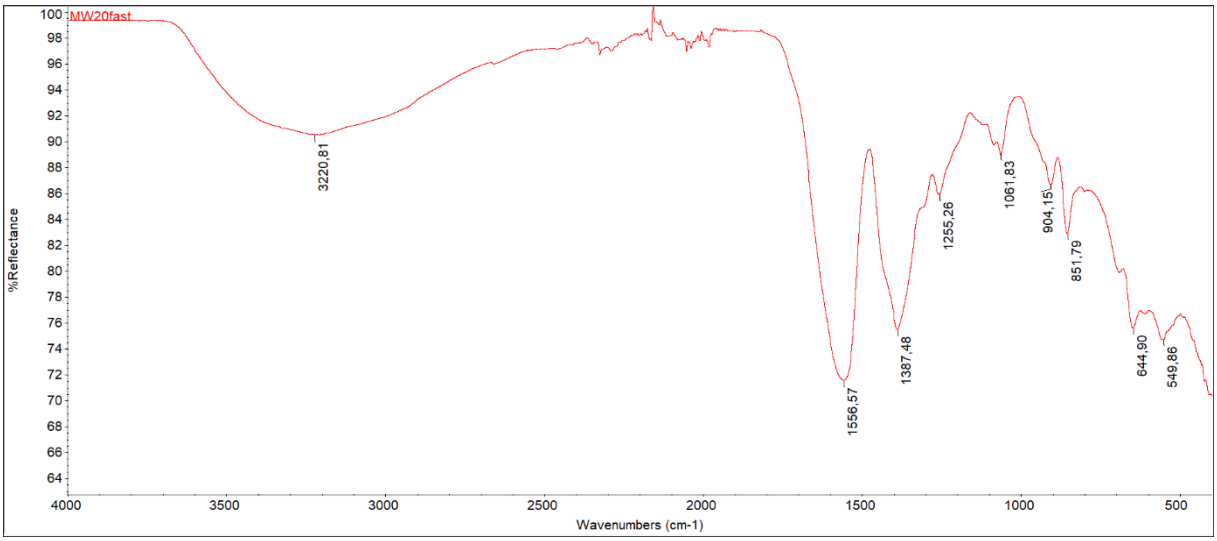

Figure A23: FT-IR Spectrum for CF-3.

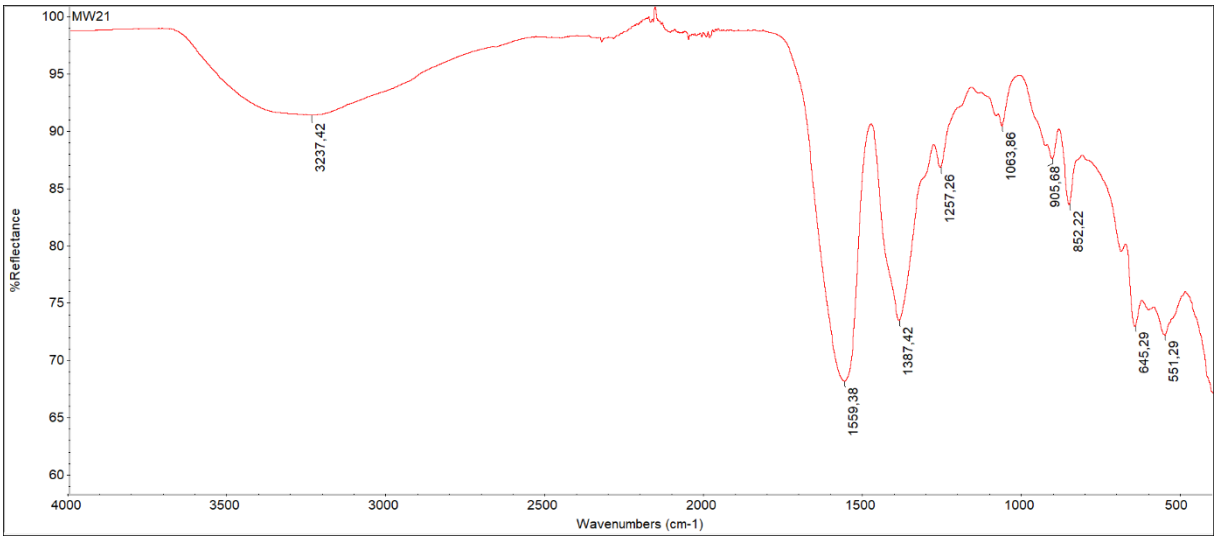

Figure A24: FT-IR Spectrum for CF-4.

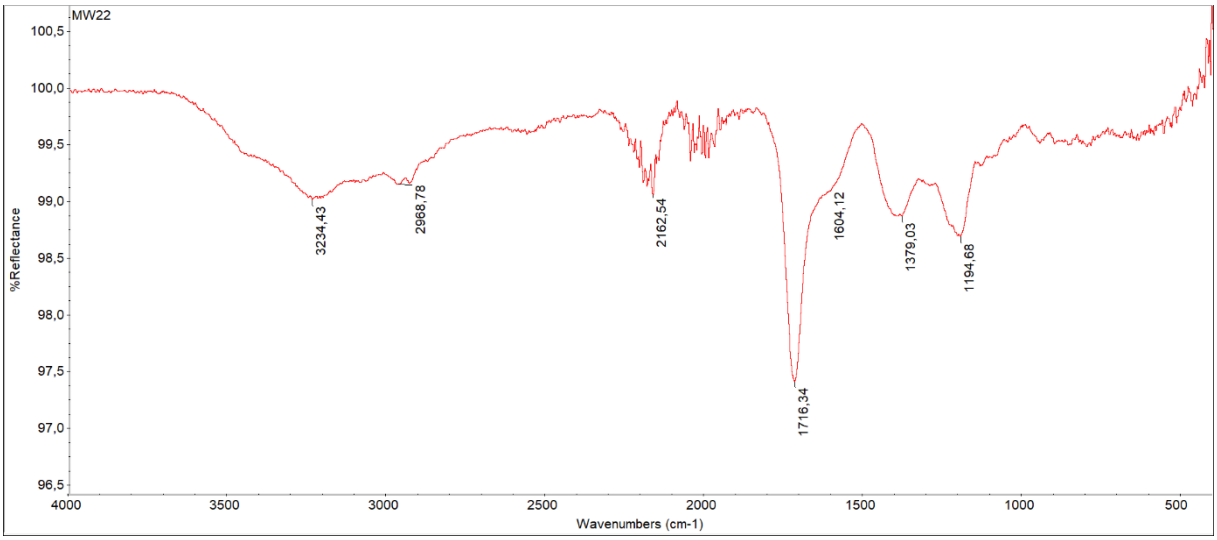

Figure A25: FT-IR Spectrum for CF-5.

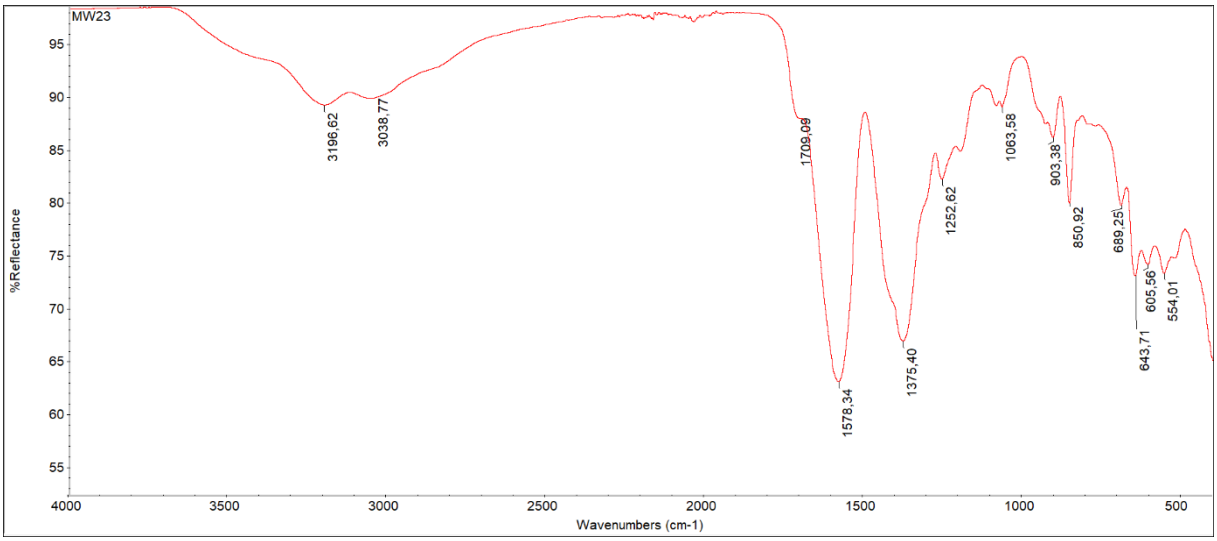

Figure A26: FT-IR Spectrum for CF-6.

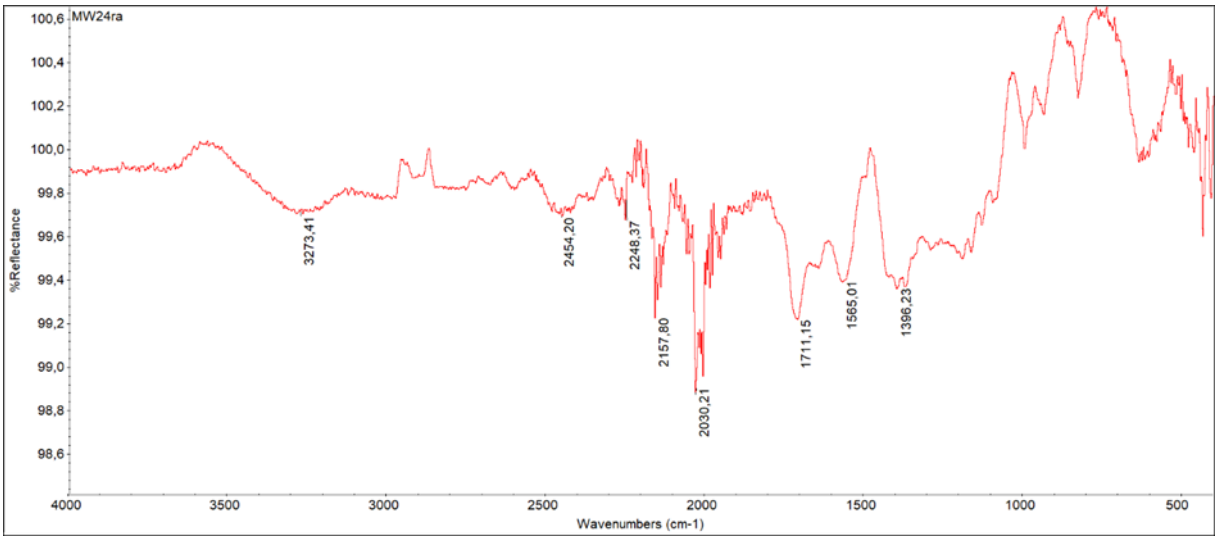

Figure A27: FT-IR Spectrum for CF-7.

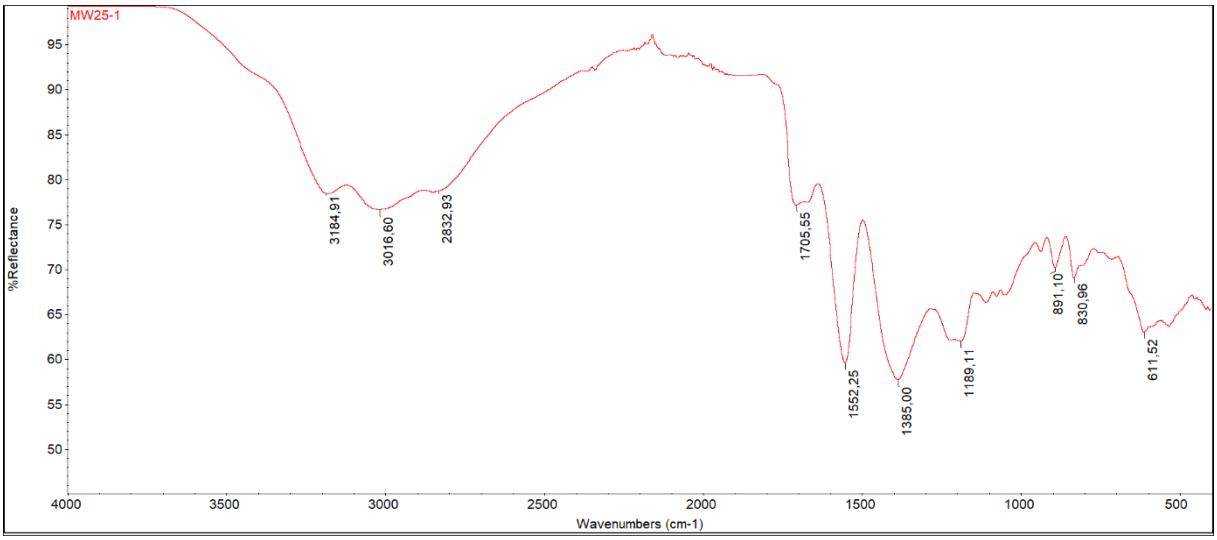

Figure A28: FT-IR Spectrum for CF-8a.

Figure A29: FT-IR Spectrum for CF-8b.

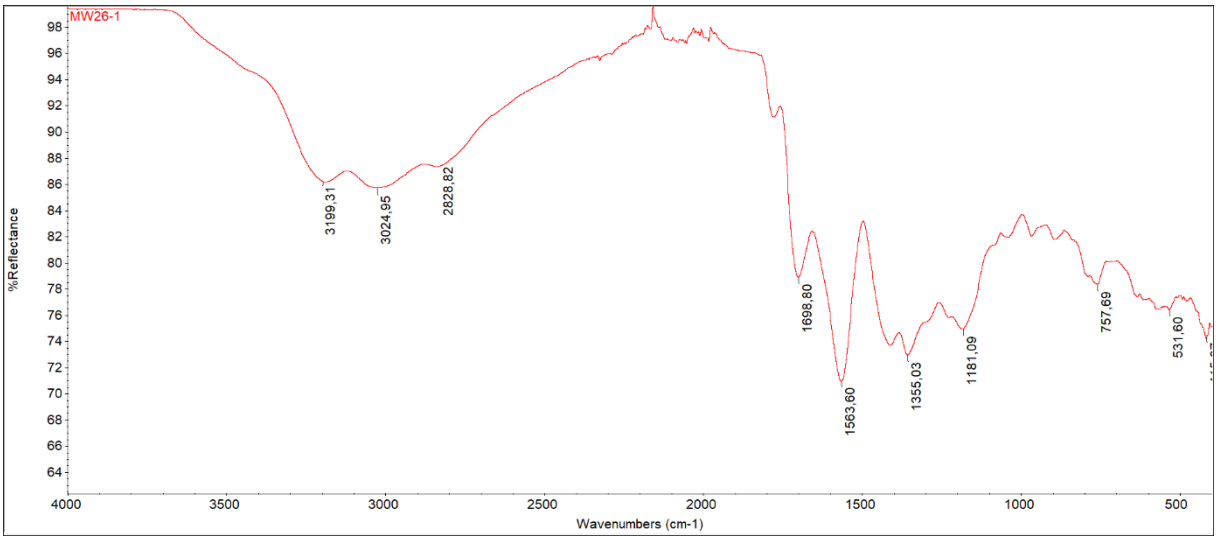

Figure A30: FT-IR Spectrum for CF-9a.

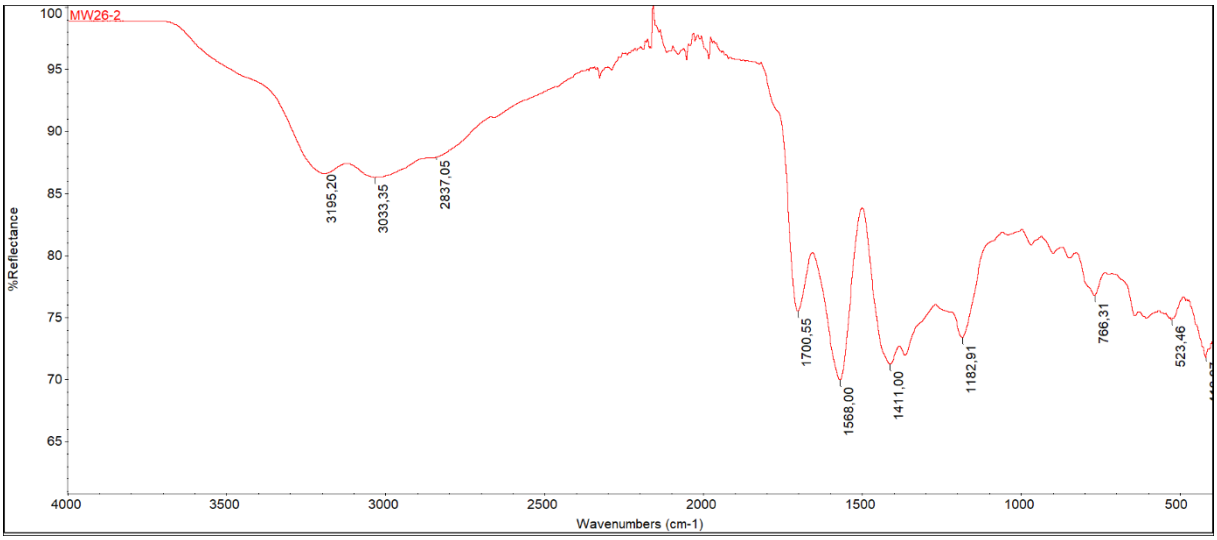

Figure A31: FT-IR Spectrum for CF-9b.

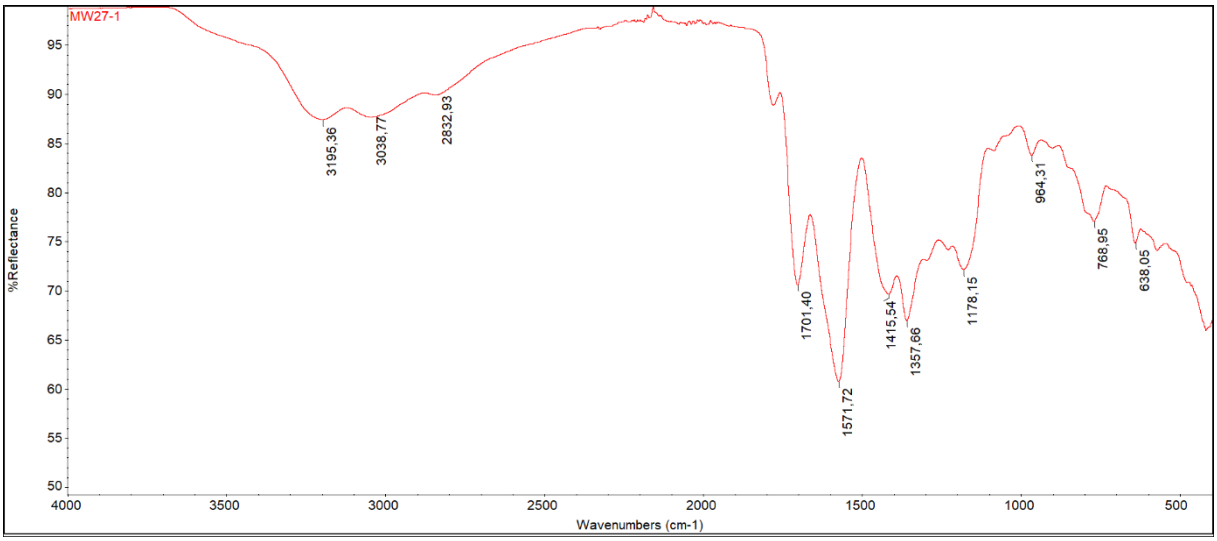

Figure A32: FT-IR Spectrum for CF-10a.

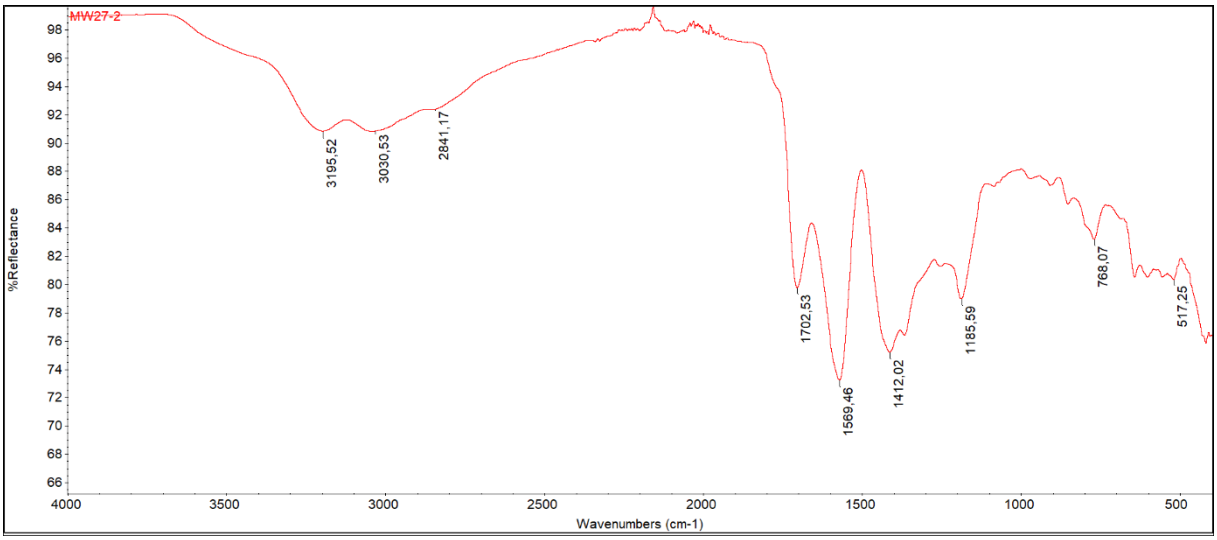

Figure A33: FT-IR Spectrum for CF-10b.

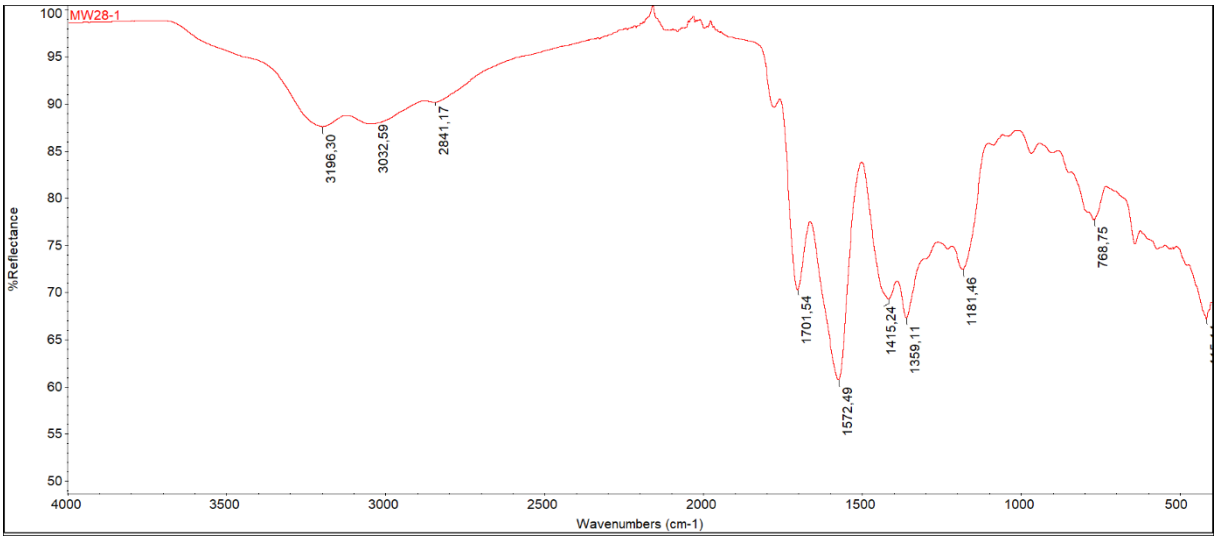

Figure A34: FT-IR Spectrum for CF-11a.

Figure A35: FT-IR Spectrum for CF-11b.

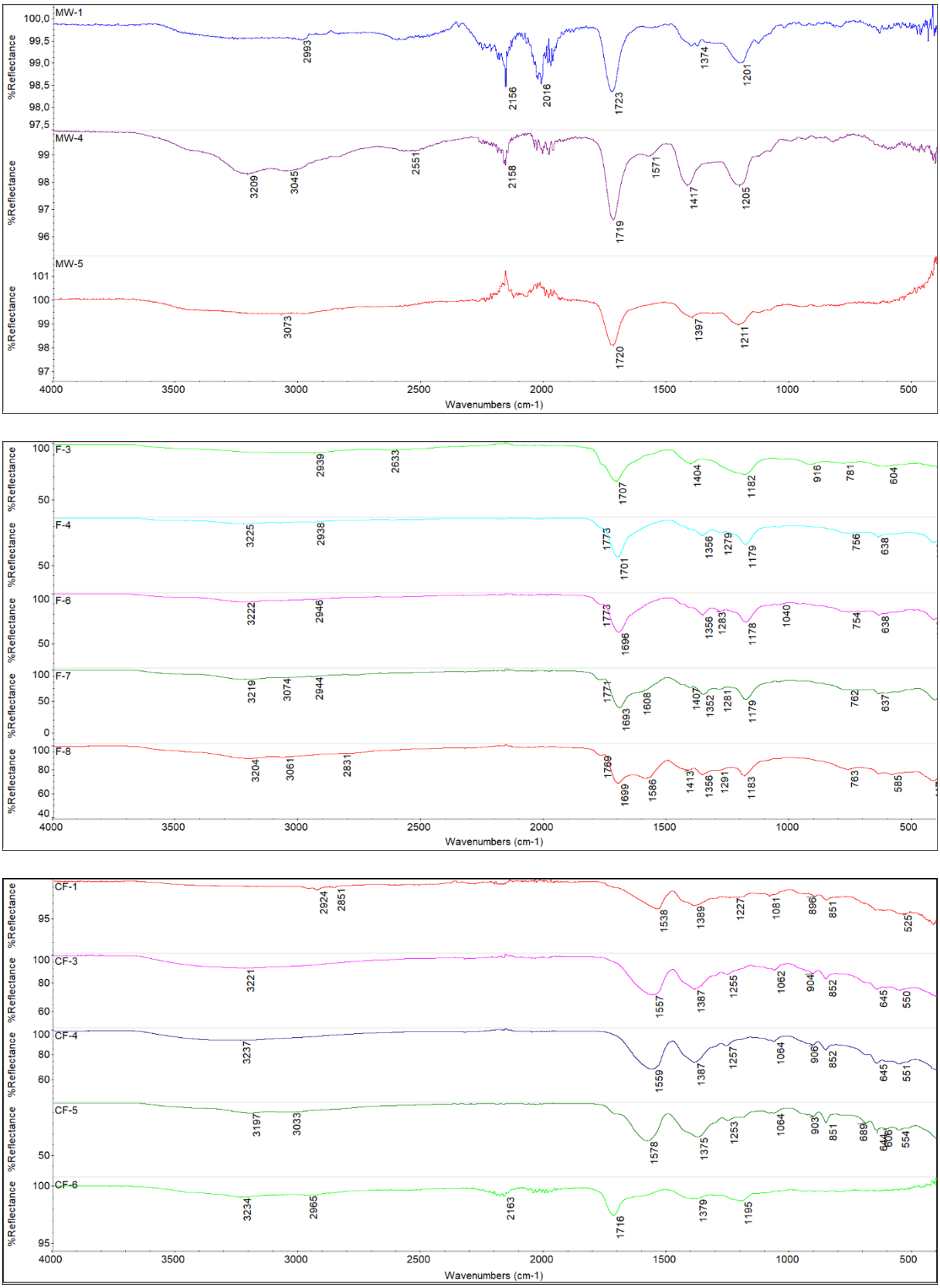

Figure A36: FT-IR spectra for samples synthesized with varying molar ratios of CA and urea, using different methods. Each spectrum is displayed in terms of %reflectance to highlight the differences.

J TEM Images

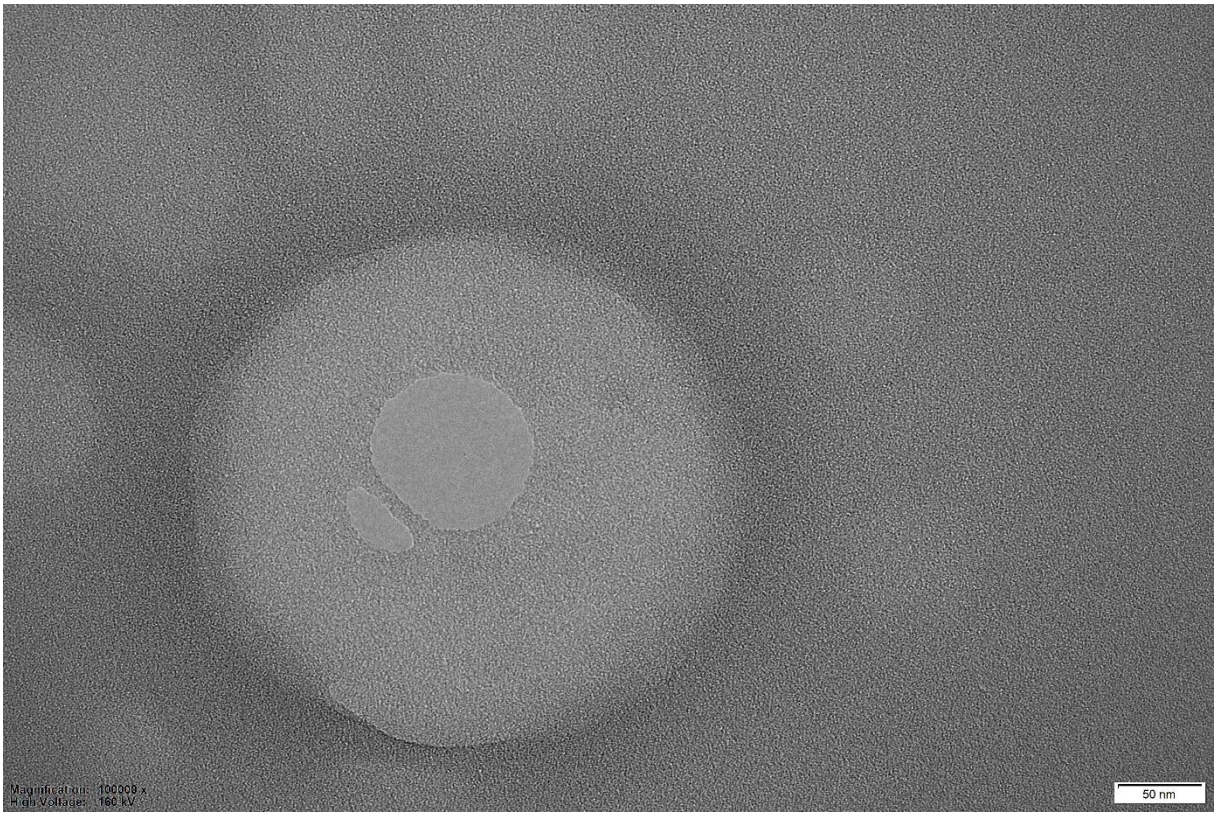

Figure A37: TEM image of sample F-6.

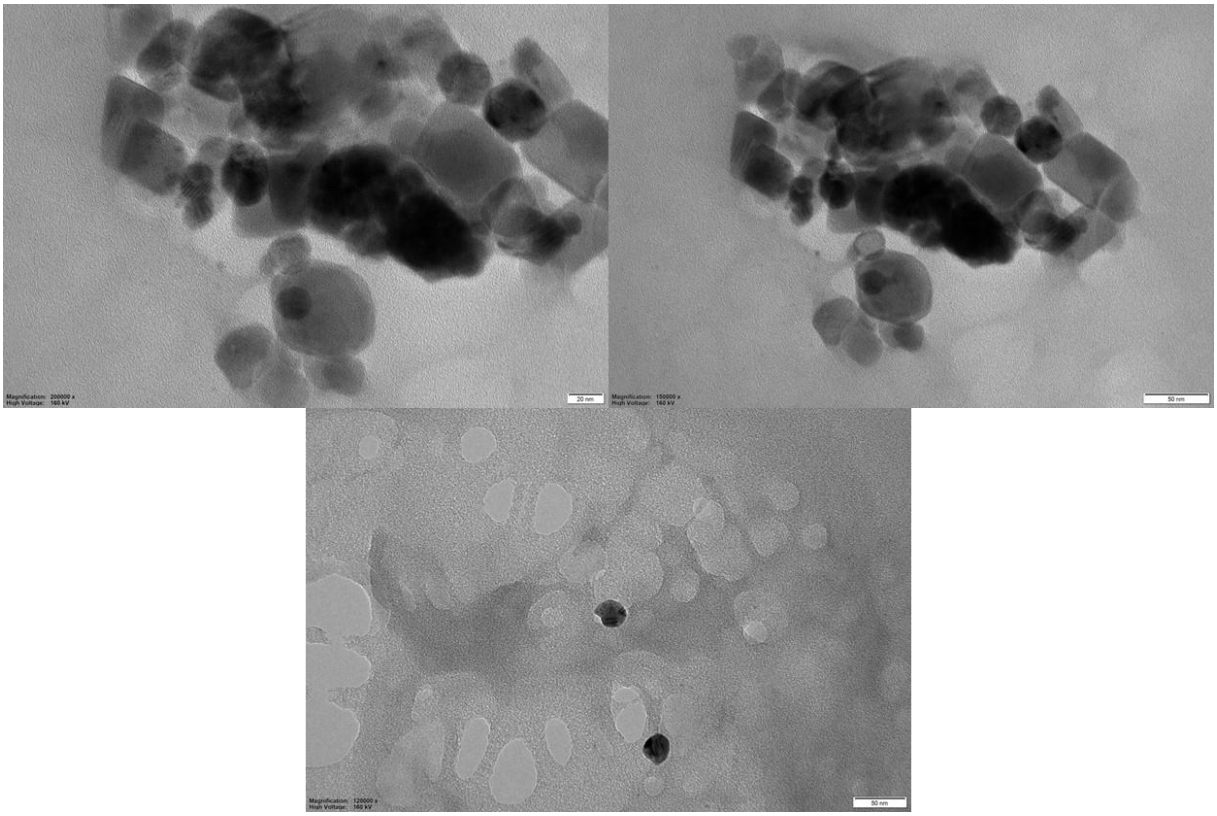

Figure A 38: TEM images of sample CF-5.

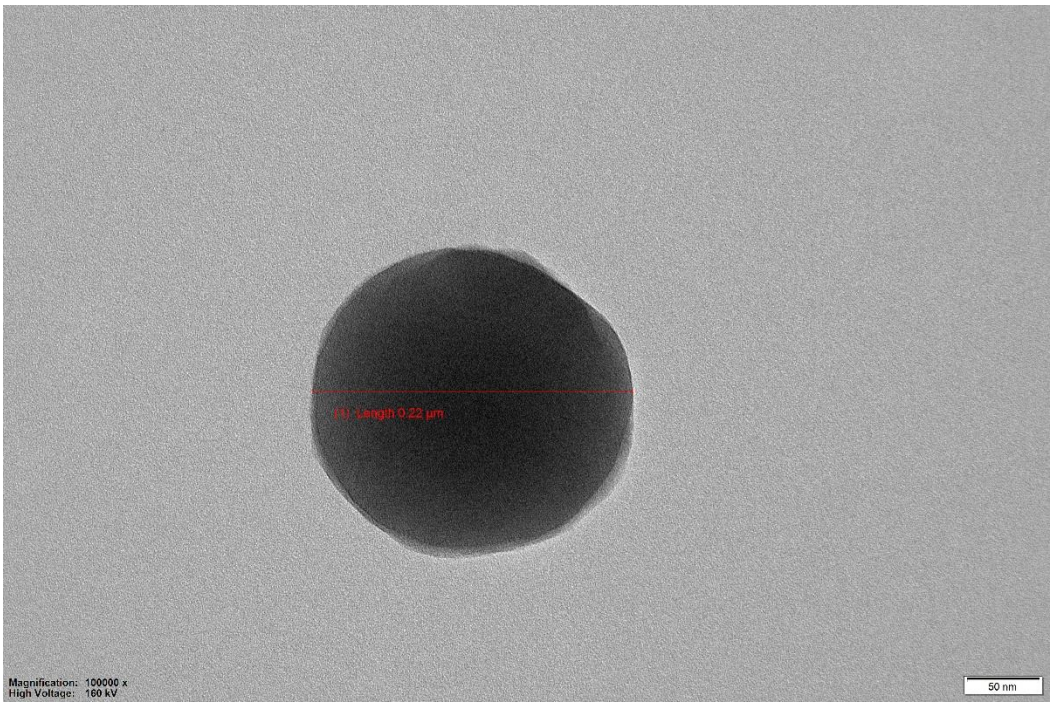

Figure A39: TEM image of sample CF-8a.

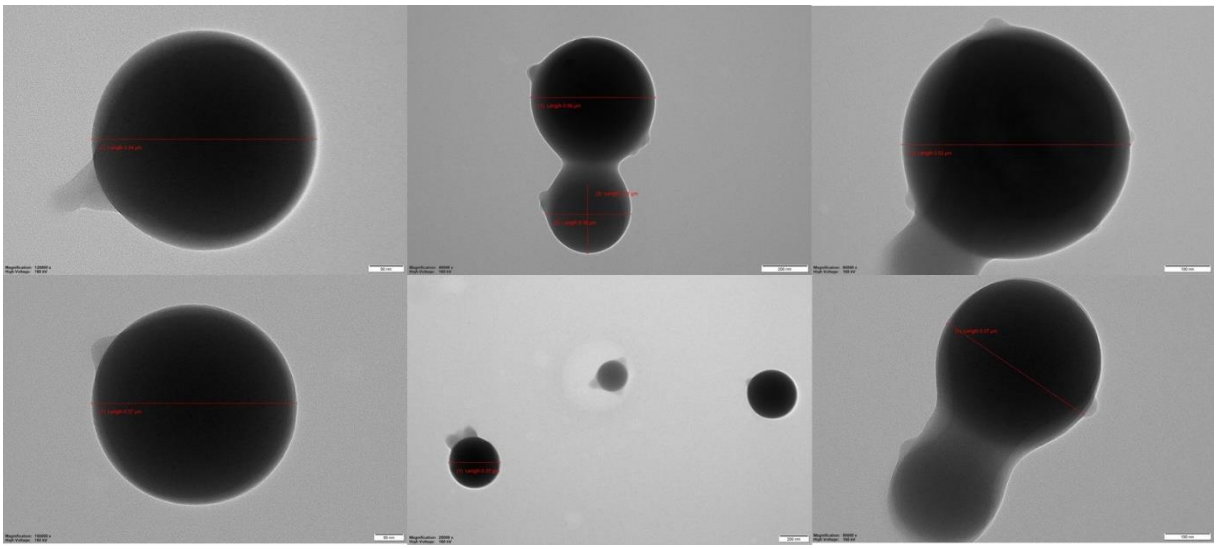

Figure A40: TEM images of sample CF-8b.

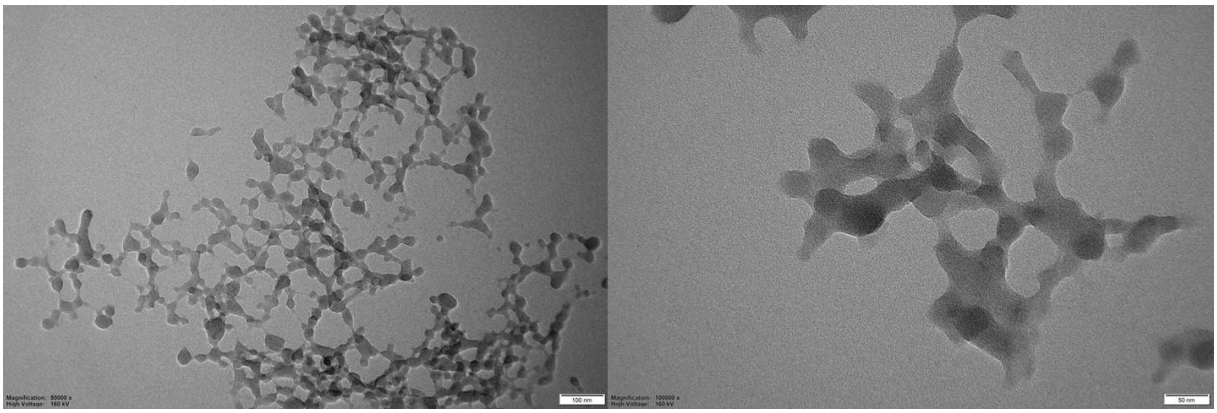

Figure A41: TEM images of sample CF-9a.

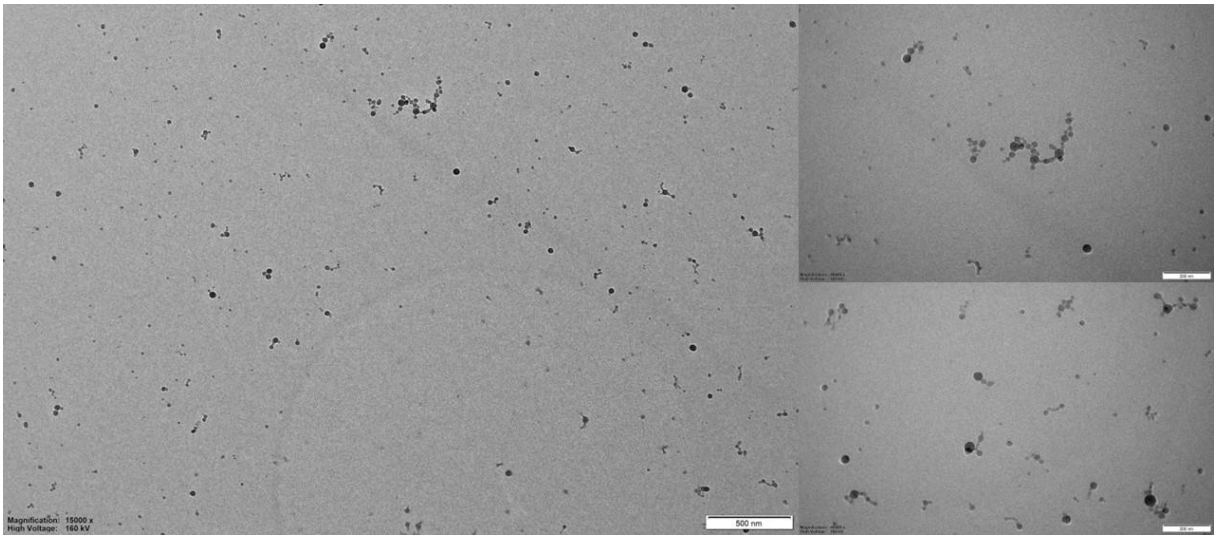

Figure A42: TEM images of sample CF-10a.

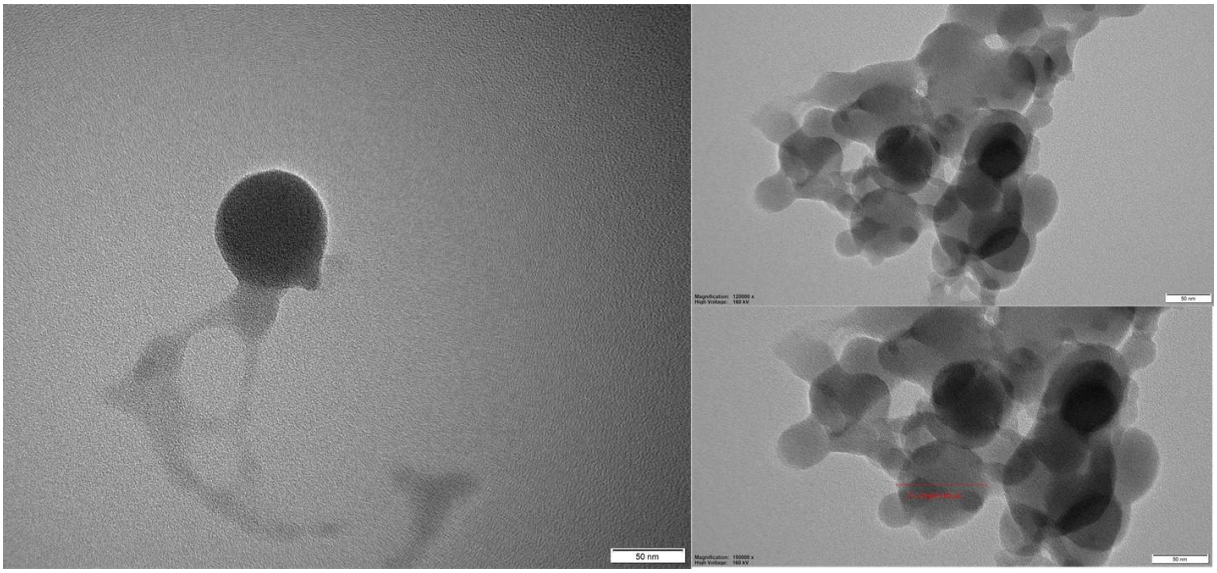

Figure A43: TEM images of sample CF-10b.

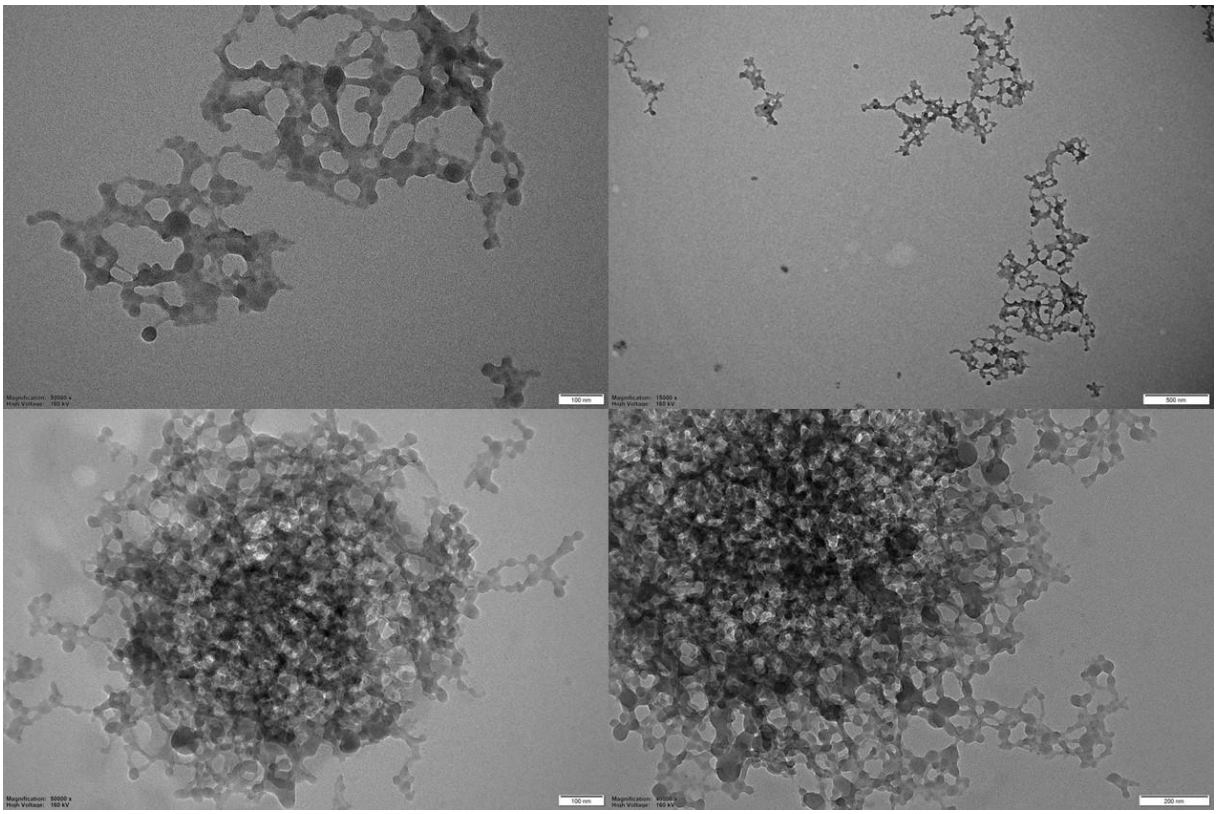

Figure A44: TEM images of sample CF-11a.

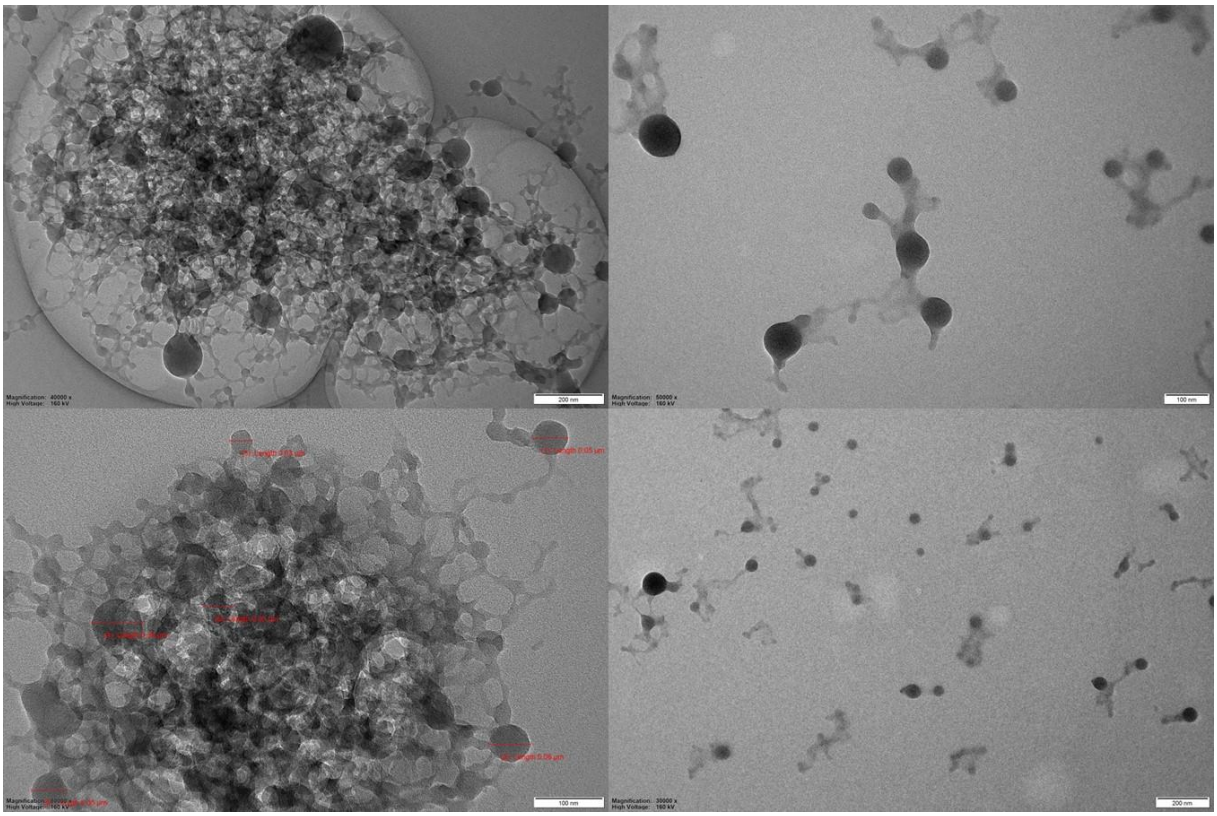

Figure A45: TEM images of sample CF-11b.